Variational assimilation of stratospheric remote sounding data by an adjoint chemistry-transport-model

Inaugural-Dissertation
zur
Erlangung des Doktorgrades
der Mathematisch-Naturwissenschaftlichen Fakultät
der Universität zu Köln

vorgelegt von

Dagmar Klasen

aus Aachen

Köln 2003

Berichterstatter:
Prof. Dr. A. Ebel
Prof. Dr. M. Kerschgens

Tag der mündlichen Prüfung: 4.7.2003

M I T T E I L U N G E N
aus dem Institut für Geophysik und Meteorologie
der Universität zu Köln
Herausgeber: M. Kerschgens, F. M. Neubauer, M. Pätzold, P. Speth, B. Tezkan

Heft 155

D a g m a r K l a s e n

Variational assimilation of stratospheric remote sounding data by an adjoint chemistry-transport-model

Köln 2003

Anmerkung: Eine Farbversion dieser Arbeit findet sich auf der beigefügten CD-ROM. Formate sind ps und pdf.

ISSN 0069-5882

Abstract

In recent years high resolution data have become available due to the deployment of satellite born instruments observing the state of a large number of stratospheric constituents with unprecedentedly high horizontal and vertical resolution. These measurements are valuable for accessing the state of the atmosphere and for helping to develop guidelines for its preservation as a protection layer for terrestrial life. Nevertheless, the measurements alone offer limited direct information. They require interpretation and combination with other information sources to accurately describe the state of the atmosphere. By combining measurements with atmospheric models, the measurements' scatter in time and space can be mitigated and their interpretation improved. A **c**hemistry-**t**ransport **m**odel (CTM) version of the **Co**logne **M**odel of the **M**iddle **A**tmosphere (COMMA) has been developed to model transport and chemical transformation of atmospheric trace gases. In this thesis, the method of four-dimensional variational data assimilation is used to realize the above-mentioned combination in a mathematically rigorous way. The goal is to identify the most probable chemical state of the atmosphere using all available information. As chemistry-transport modelling is an initial value problem, those initial conditions are sought which result in best compliance of the model state with available information during the time period considered. As a measure of compliance, a cost function is specified, whose gradient is needed for minimising the cost function, and which can be obtained by means of an adjoint model. To this end, the adjoint code to the CTM was developed. As a last building block of the data assimilation system, the L-BFGS algorithm for the minimization of the cost function was added. The **A**djoint **M**odel of the **M**iddle atmosphere **o**f **C**ologne CTM (AMMOC-CTM) data-assimilation system thereby developed was tested by applying it to data measured by the **Cr**yogenic **I**nfrared **S**pectrometer and **T**elescopes for the **A**tmosphere (CRISTA) during the first campaign conducted in November 1994. In this thesis, the first 4D var chemical data assimilation system is presented that takes into consideration horizontal correlations by means of a new penalty term in the cost function. The usefulness of the AMMOC-CTM for the analysis of chemically active constituents from satellite measurements was demonstrated by the synoptic maps which it produced. The model results were tested for consistency with the underlying assumptions by means of statistical investigations that for the first time included evaluation of the background term. After parallelization, the developed model system can be used to routinely create synoptic maps assimilating for example Envisat (Environmental Satellite) data. CTMs such as the AMMOC-CTM are not only useful for scientific investigations, but can provide essential information for environmental policy making and supervision as well, for example concerning the interdiction to produce certain CFCs.

Kurzzusammenfassung

Durch den Einsatz von satellitengestützten Instrumenten, die die Konzentration einer großen Anzahl von stratosphärischen Konstituenten mit bislang unerreichter hoher horizontaler und vertikaler Auflösung beobachten, sind in den letzten Jahren hochpräzise Daten verfügbar geworden. Diese Messungen sind wichtig, um den Zustand der Atmosphäre einzuschätzen und um Richtlinien zu ihrer Bewahrung aufzustellen. Dennoch bieten Messungen alleine nur eine begrenzte Menge an Informationen. Sie müssen interpretiert und mit anderen Informationsquellen kombiniert werden, um die Atmosphäre genau zu beschreiben. Durch Kombination der Messungen mit Atmosphärenmodellen wird die Streuung der Messungen in Raum und Zeit gemindert und ihre Interpretation verbessert. In der vorliegenden Dissertation wurde eine **C**hemie-**T**ransport-**M**odellversion des Kölner Modells der Mittleren Atmosphäre (COMMA) entwickelt und die Methode der vierdimensionalen variationalen Datenassimilation dazu verwendet, um den wahrscheinlichsten chemischen Zustand der Atmosphäre unter Verwendung aller zur Verfügung stehenden Informationen zu bestimmen, und zwar mit einem mathematisch fundierten Zugang. Die Chemie-Transport-Modellierung stellt ein Anfangswertproblem dar, daher werden diejenigen Anfangswerte gesucht, die während des betrachteten Zeitintervalls zur besten Übereinstimmung des Modellzustandes mit den verfügbaren Informationen führen. Als Maß der Übereinstimmung wird eine Kostenfunktion definiert, die unter Verwendung ihres Gradienten minimiert wird. Dieser wird mithilfe eines adjungierten Modells bestimmt. Zu diesem Zweck wurde der zum CTM adjungierte Code entwickelt. Als letzter Baustein des Datenassimilationssystems wurde der L-BFGS Algorithmus zur Minimierung der Kostenfunktion hinzugefügt. Das dadurch entwickelte Datenassimilationssystem AMMOC-CTM wurde durch Anwendung auf Realdaten getestet, die das **Cr**yogenic **I**nfrared **S**pectrometer and **T**elescopes for the **A**tmosphere (CRISTA) während der ersten Kampagne im November 1994 gemessen hat. Im Rahmen dieser Arbeit wurde das erste 4D var chemische Datenassimilationssystem entwickelt, das die horizontalen Feldkorrelationen durch Verwendung eines entsprechenden Terms in der Kostenfunktion berücksichtigt. Die Zweckmäßigkeit des AMMOC-CTMs zur Analyse von chemisch aktiven Konstituenten aus Satellitenmessungen wurde durch die Erstellung synoptischer Karten demonstriert. Die Modellergebnisse wurden auf Konsistenz mit den zugrundeliegenden Annahmen statistisch untersucht, dazu gehörte erstmalig die Bewertung des Hintergrundterms. Nach Parallelisierung kann das entwickelte Modellsystem dazu genutzt werden, routinemässig synoptische Karten beispielsweise durch Assimilation von Envisat (Environmental Satellite) Daten zu erstellen. CTMs wie das AMMOC-CTM werden nicht nur für wissenschaftliche Untersuchungen genutzt, sondern können auch essentielle Informationen für die Umweltpolitik und zur Umweltüberwachung liefern, beispielsweise hinsichtlich des Produktionsverbots bestimmter CFCs.

Contents

List of Figures

List of Abbreviations

ATLAS	**At**mospheric **L**aboratory for **A**pplications and **S**cience
AMMOC	**A**djoint **M**odel of the **M**iddle Atmosphere **o**f **C**ologne
ATMOS	**A**tmospheric **T**race **Mo**lecule **S**pectroscopy
BLUE	**b**est **l**inear **u**nbiased **e**stimate
CFC	**c**hloro**f**luoro**c**arbon
COMMA	**Co**logne **M**odel of the **M**iddle **A**tmosphere
CRISTA	**Cr**yogenic **I**nfrared **S**pectrometer and **T**elescopes for the **A**tmosphere
CTM	**c**hemistry-**t**ransport **m**odel
Envisat	**Envi**ronmental **Sat**ellite
GCM	**g**eneral **c**irculation **m**odel
HALOE	**Hal**ogen **O**ccultation **E**xperiment
KPP	**K**inetic **P**re**P**rocessor
L-BFGS	**l**imited memory **B**royden **F**letcher **G**oldfarb **S**hanno algorithm
MAS	**M**illimeter-wave **A**tmospheric **S**ounder
MLS	**M**icrowave **L**imb **S**ounder
NDSC	**N**etwork for the **D**etection of **S**tratospheric **C**hange
POAM	**P**olar **O**zone and **A**erosol **M**easurement
PSC	**p**olar **s**tratospheric **c**loud
QBO	**q**uasi **bi**annual **o**scillation
SAGE	**S**tratospheric **A**erosol and **G**as **E**xperiment
SAO	**s**emi-**a**nnual **o**scillation
SPAS	**S**huttle **Pa**llet **S**atellite
UARS	**U**pper **A**tmosphere **R**esearch **S**atellite
UKMO	**U**nited **K**ingdom **M**eteorological **O**ffice
WMO	**W**orld **M**eteorological **O**rganization
4D-PSAS	**four d**imensional **P**hysical-space **S**tatistical **A**nalysis
4D var	**four d**imensional **var**iational

CHAPTER 1

Introduction

Shortly after the discovery of the ozone layer, the ability of the middle atmosphere (between 10 and 100 km altitude) to filter harmful ultraviolet (UV) radiation was recognised. An important consequence of the UV absorption by the ozone layer is its heating, which results in an increase of stratospheric temperature up to the stratopause at about 50 km altitude. Above the ozone layer, in the mesosphere, a characteristic decrease of temperature is found as a result of combined radiative and dynamic effects. Stratospheric temperature increase due to the ozone layer suppresses vertical movements. This shows that the ozone layer is an important component influencing atmospheric dynamics. Thus, its development has to be considered for climate change studies. In 1985, Farman et al. published the observation of a drastic reduction of the ozone concentration at the south pole in early spring which is now known by the term "ozone hole". Increased chlorine loading of the atmosphere was theorised to contribute to the ozone depletion. This drastic reduction or even complete destruction of ozone was reported for altitudes where usually the ozone concentration is at its maximum. This discovery has initiated an intensive investigation of the chemical state of the stratosphere. As a part of this effort, routine measurements were complemented by measurement campaigns, special laboratory experiments were conducted, and chemistry-transport-models (CTMs) and instruments were improved. So far the following picture has emerged: man-made chlorofluorocarbons and halons have been confirmed to be responsible for the increased ozone destruction. These gases, which are inert in the troposphere, are transported into the middle atmosphere where their dissociation due to UV radiation leads to chlorine release. In the presence of polar stratospheric clouds (PSCs) and sunlight, chlorine catalytically destroys large amounts of

ozone. In mid-latitudes, ozone loss is increased following volcanic eruptions due to heterogeneous reactions on sulfate aerosols. An additional process that reduces the total ozone amount (amount of ozone between the ground and the top of the atmosphere) at mid-latitudes is the mixing of ozone-depleted air from polar to mid-latitudes. Recently, the decline in total ozone observed in mid-latitudes has slowed down (World Meteorological Organization, 1999). Chlorine can be removed from the middle atmosphere through formation of water soluble HCl which is precipitated by water droplets or crystals. Due to international efforts following the Montreal protocol and its amendments, the production of chlorofluorocarbons has been reduced, leading to a reduction of the atmospheric concentration of these species. Several studies estimated the recovery time after which the level of chlorine loading can be expected to return to pre-ozone hole values. Engel et al. (2002) expect the total chlorine loading at 20 km altitude inside the polar vortex to reach values similar to those of 1980 (pre-ozone hole) approximately in the year 2060. Other authors concluded this might occur as early as 2040 (Solomon, 1999). However, according to Waibel et al. (1999), even in 2070 enough chlorine might be present in the atmosphere to deplete ozone. The reduced chlorine content of the atmosphere will eventually lead to a slow return of the ozone concentration to pre-ozone hole values. Weatherhead et al. (2000) employed a two-dimensional chemical model to estimate the time when the ozone recovery should become detectable at different locations. For most regions they determined a noticeable recovery in 15–45 years. Reinsel (2002) has detected a positive trend in Umkehr data at the three stations Arosa, Boulder and Tateno for the five-year period 1996–2001. Further details of dynamical processes which are of special interest for the middle atmosphere are described in Chapter 4.

Nowadays satellites observe the chemical state of the atmosphere continuously. An analysis of this enormous amount of data allows the derivation of a global and more detailed description of the atmospheric state. The existent data sources differ widely with respect to data density, measurement frequency and representativity. For example, the Network for the Detection of Stratospheric Change (NDSC) is a set of remote-sounding research stations for observing and understanding the physical and chemical state of the stratosphere. Figure 1.1 shows the geographically irregular distribution of NDSC sites, where frequent remote sensing and in-situ measurements are performed by means of balloon soundings and ground-based remote sensing techniques. These measurements focus on ozone and ozone-related chemical compounds and parameters. The geographical coverage by satellite instruments is also characterised by irregularities. The measurement frequency at a given location depends on the satellite orbit. For example, CRISTA, which will be described in Chapter 3, covered middle latitudes about twice as often as equatorial latitudes, but did not measure poleward of 67° at all during its first mission in 1994. On the other hand, satellites can sample even

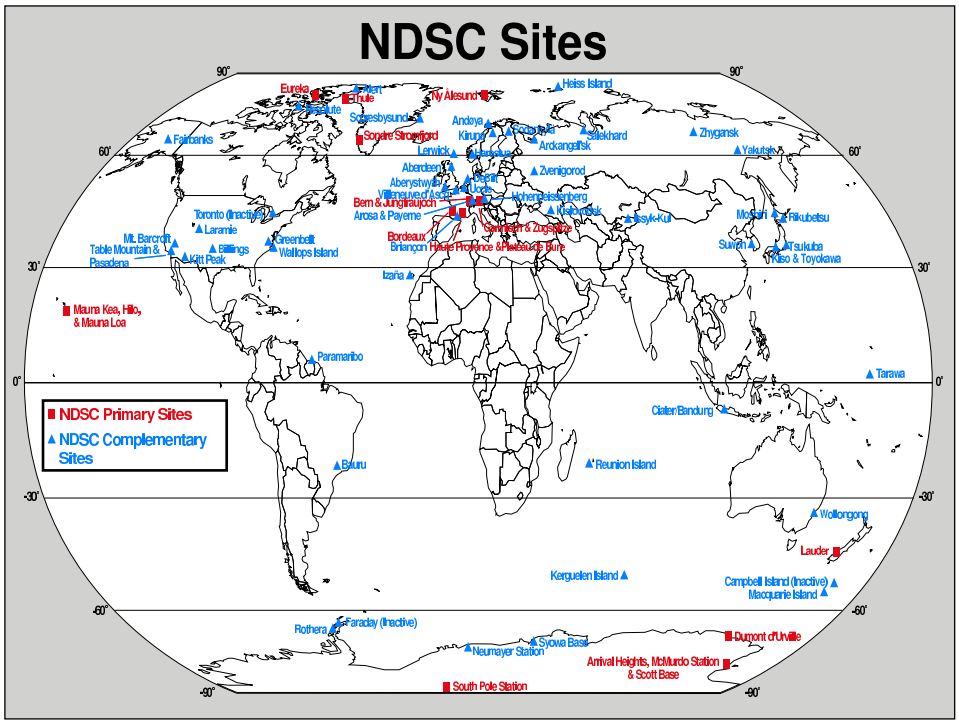

Figure 1.1: *Geographical distribution of the Network for the Detection of Stratospheric Change measurement sites. The disadvantage of the irregular distribution of the measurement sites can partially be compensated by the use of progressive data assimilation techniques.*

remote locations, for example above oceans or mountains. Furthermore, some instruments, like those mounted on Envisat (Environmental Satellite, launched by the European Space Agency ESA on March 01, 2002), are capable of long-term observations.

Because of the observational heterogeneity, sophisticated methods are needed for the joint interpretation of the measurements. The application of a CTM allows one to combine measurements with a priori knowledge of chemical and physical atmospheric processes. CTMs examine the influence of transport and chemical reactions on the chemical composition of the atmosphere. They use meteorological analyses, e.g. from general circulation models (GCMs), as input. In this thesis, analyses from the United Kingdom Meteorological Office (UKMO) for the Upper Atmosphere Research Satellite (UARS) project are used in a CTM that was adopted from the Cologne Model of the Middle Atmosphere (COMMA) within the scope of this thesis. The model is described in detail in Chapter 5. The method of choice for combining experimental data and numerical models is the four-dimensional variational (4D var) data assimilation, which is described in detail in Chapter 2.1. It allows the incorporation of measurements in the modelling process

by paying attention to the information's significance without disturbing the chemical equilibrium of the model. By using this approach, the irregular distribution of the measurements is compensated. Synoptic maps created in this way are value-added products in the sense that their information content is superior to that of the raw data. The modifications of the COMMA-CTM that were necessary to allow the development of an efficient and stable 4D var data assimilation system are described in Chapter 5.1.

The 4D var method is based on the fact that chemistry-transport modelling is an initial value problem so that the choice of the initial values determines the degree of compliance of the model with measurements at later times as well. The agreement between the model state on the one side and measurements as well as further information such as climatologies or former model runs on the other side during the so-called assimilation period is measured by a scalar valued cost function. The definition of the cost function requires careful considerations as it weighs the relative influence of every information source through the employed error covariance matrices. Because of the use of the cost function that weighs the influence of model and observations the resulting analysis can be claimed to be objective. Besides observations and previous model runs, the use of curvature of the trace gas field as information is examined in this work. The curvature penalty term in the cost function controls the curvature of the trace gas fields at the beginning of the assimilation interval. It compares neighbouring grid boxes and can spread information from observed to unobserved neighbouring locations. This additional term for the cost function and its gradient are described in Chapter 7 followed by a comparison with an alternative method for spreading information, the use of off-diagonal entries in the background error covariance matrix. It is shown that the assumption about the field and error correlations of the employed background field are the basis for the decision which of the two methods is advisable.

The model domain comprises (96*71+2)*10 grid points and at each grid point, the initial values of 41 species are required. For this reason, the L-BFGS minimization algorithm which needs only moderate amounts of storage space was chosen to find new initial values which result in a smaller cost function. The algorithm is described in Chapter 8.1 along with a description of the performed modifications. To facilitate rapid minimization, the trace gas mixing ratios are preconditioned before the minimization is called.

For the minimization, the gradient of the cost function is required. It is efficient to determine the gradient by the adjoint model to the tangent-linear CTM. In Chapter 6, the development of the adjoint code is explained. The CTM, the adjoint model, and the minimization algorithm compose the 4D var data assimilation system named Adjoint Model of the Middle Atmosphere of Cologne (AMMOC-CTM) as described in Chapter 9. An overview of the implementation is given in Chapter 9 along with additional information concerning the storage and recalculation strategy which is

needed because the adjoint model needs large amounts of information from the forward model trajectory.

The assimilation system allows the determination of the initial state of the CTM, which results in closest agreement with all available information in the sense of a least square estimate. Thus, it provides the best linear unbiased estimate (BLUE). The price for this superior performance are high computational demands. The AMMOC-CTM was tested in identical twin experiments which are described in Chapter 10. Besides demonstrating the correct set-up of the model system, these tests allowed to investigate how the choice of measured trace gases provided to the assimilation system influences the quality of the analysis. In particular, these experiments were focused on the conditions prevalent in November and the species measured by CRISTA in preparation of the real case experiment. The results indicated that the available measurements lead to an improved description of the observed and also of many unobserved species. The quality of the analysis however depends on the chemical regime of the grid box.

The assimilation of CRISTA measurements is subject of Chapter 11. The properties of the assimilation system using the curvature penalty term are examined through synoptic maps and statistical investigations.

The analysis depends strongly on the errors attributed to the different information sources through the error specification in the cost function. A verification proposed by Talagrand (1998) has been extended to examine the consistency of the analysis with the error covariance matrices. It is derived in Chapter 12 and applied to the performed real case experiments. Finally, the last chapter gives a summary of the present work and discusses the obtained results.

CHAPTER 2

Data assimilation methods

The most important goal of a data assimilation system is the combination of a model and measurements. With this approach it is attempted to obtain a more complete picture of the atmospheric state and its evolution, compared to using both information sources separately. A conceptually simple approach in this direction is nudging. This method was used by Austin (1992) who first assimilated chemical data into a CTM by using a nudging scheme which corrected concentrations at nearby grid points towards the observations at the time of measurement. One difficulty in this approach is the proper selection of the nudging coefficients. Additional difficulties may arise from a poorly known relaxation process and a possible induction of a bias.

One disadvantage of simple data assimilation methods lies in the fact that the exactness of the different pieces of information is usually not accounted for. This may lead to rejection of observations like in the approach used by Smyshlyaev and Geller (2001), where data that did not pass an a priori quality control were not inserted into the model.

To make best use of the available information, more sophisticated data assimilation methods employ all available sources of information together with their errors. In this way, the goal of objectivity can be pursued, and the analysis can be checked for consistency with the utilised pieces of information. This implies that a state-of-the-art data assimilation system can show its full capacities only if enough information about the errors is available.

Another requirement for sophisticated data assimilation methods is to handle observations distributed in time. The way in which this is accomplished can be used to distinguish between different data assimilation meth-

ods. In intermittent data assimilation, at every model time step an optimization problem is solved considering all sources of information attributed to this time step. This method was widely used in the 1980's (Daley, 1991) and early 90's. On the other hand, the 4D var method makes use of all the information for a chosen time period to estimate the state of the atmosphere at all points in time during this period which is called assimilation period. For this reason, 4D var is a smoother and delivers a coherent picture during the assimilation period. In contrast, a filter such as the Kalman filter propagates the information forward in time only. This is a sequential procedure. Further comparison between these two approaches can be found in Section 2.2.

The possibility to include many independent measurements and model knowledge in sophisticated data assimilation systems is a major improvement as compared to other methods, which often limited past investigations to ozone measurements only. In state-of-the-art atmospheric chemical data assimilation systems, the use of a chemistry module ensures that the coupling between different species is provided for. Since transport modules are also incorporated, measurements with different observation geometries, observation locations and times can be combined, and even spatially and temporally sparse observations can be taken into account. These model systems can then deliver information about unmeasured but chemically coupled species and about data-void regions. In addition, one can consider indirect observations, i.e. observations of species or quantities that do not belong to the model, but are related to a model quantity. As a result, synoptic maps can be created, and one can pursue what Ghil and Malanotte-Rizzoli (1991) describe as "the ambitious and elusive goal of data assimilation": "to provide a dynamically consistent 'motion picture' of the atmosphere $\cdots$ in three space dimensions, with known error bars."

The 4D var data assimilation method was developed in the realm of meteorology, e.g. Lewis and Derber (1985), LeDimet and Talagrand (1986), Talagrand and Courtier (1987). It was motivated by the search for a better initialization of weather forecast models and by the desire to consider a diverse spectrum of observations. In particular, an increasing number of asynoptic observations (taken at other times than the synoptic times 06, 12 18 and 24 UTC) from satellites became available. 4D var data assimilation was introduced into the ECMWF analysis cycle in 1997 (Rabier et al., 2000; Mahfouf and Rabier, 2000; Klinker et al., 2000).

A first application of the 4D var method to chemistry-transport modelling was performed by Fisher and Lary (1995). These authors employed a stratospheric chemistry algorithm reduced to eight constituents. A complex chemically-dynamically coupled data assimilation system for the troposphere was developed and applied to case studies (Elbern et al., 1997; Elbern and Schmidt, 1999; Elbern et al., 1999a,b, 2000). Errera and Fonteyn (2001) developed a 4D var CTM and applied it to the first CRISTA cam-

paign in November 1994. However, as far as the development of the adjoint code is concerned, there are considerable differences between the model they employed and the model presented in this thesis. Errera and Fonteyn (2001) discretised the adjoint of the continuous model equation, while in the present approach the adjoint of the discretised model equation is used. This difference is elaborated on in Chapter 6. Furthermore, in the present study, the treatment of measurement errors is improved by considering systematic errors in addition to statistical errors. While Errera and Fonteyn (2001) use a semi-lagrangian transport algorithm, the Eulerian Bott transport is used in this thesis. Finally, it should be added that in the present work the question of horizontal field correlations and of representativity is addressed and a method is developed and applied that consistently makes use of these correlations.

As explained in more detail in Section 2.1, the 4D var method takes into account so called background knowledge, e.g. from previous model integrations, in addition to observations taken during the assimilation period. A sophisticated approach for the inclusion of background knowledge was described in Hoelzemann et al. (2001). These authors proposed a method allowing for the use of horizontally inhomogeneous error covariances for the troposphere.

The focus of the 4D var data assimilation method is the optimization of initial values, as will be explained in Chapter 2.1. This approach is justified especially in the stratosphere as there are only few emission sources, which could in principal influence the time evolution of the model system in addition to the initial values. Further on, adjoint models can also be used to explicitly determine gradients for sensitivity analysis (Talagrand, 1991) or for parameter estimation (Zou et al., 1997).

2.1 The four-dimensional variational data assimilation system

In the area of atmospheric chemistry, the goal of four-dimensional variational data assimilation is the determination of the most probable chemical evolution of the atmosphere, taking into account the available information:

- observations from both satellite-born and ground-based instruments
- chemical and physical laws as represented by a chemistry-transport model
- a priori knowledge from previous model runs, climatologies, or spatial and chemical correlations.

The desired optimality is achieved by using the following scalar-valued cost function J:

$$\begin{aligned} J \quad &= \tfrac{1}{2} \sum_{\mathbf{r}} \left(\mathbf{c}\left(t_0, \mathbf{r}\right) - \mathbf{c}^b(t_0, \mathbf{r}) \right)^T \mathbf{B}_o^{-1} \left(\mathbf{c}\left(t_0, \mathbf{r}\right) - \mathbf{c}^b(t_0, \mathbf{r}) \right) \\ &+ \tfrac{1}{2} \sum_{i=0}^{n} \sum_{\mathbf{s}} \left(\mathbf{H}\mathbf{c}(t_i, \mathbf{r}) - \mathbf{y}^o(t_i, \mathbf{s}) \right)^T \mathbf{R}^{-1} \left(\mathbf{H}\mathbf{c}(t_i, \mathbf{r}) - \mathbf{y}^o(t_i, \mathbf{s}) \right) \ , \end{aligned} \tag{2.1}$$

which measures the deviation of the model state from the available information and thus the quality of the description of the atmospheric state. Here, $\mathbf{c}\left(t_0, \mathbf{r}\right)$ denotes the model state at the beginning of the integration at time t_0, $\mathbf{c}^b(\mathbf{r})$ denotes background knowledge, $\mathbf{H}$ interpolates from model grid space (with points $\mathbf{r}$) to observation space (with points $\mathbf{s}$) and here is assumed to be linear, and $\mathbf{c}(t_i, \mathbf{r})$ describes the model state at subsequent time steps t_i. The time period of comparison is called the assimilation interval. The background and observation error covariance matrices, $\mathbf{B}_o$ and $\mathbf{R}$, take into account the confidence in the different sources of information, and $\mathbf{y}^o(t_i, \mathbf{s})$ describes measurements at time t_i. The model state $\mathbf{c}$ is a function of space and time coordinates on a finite-dimensional grid, and the summations in Equation 2.1 are performed over all model or observation grid points. The notation mostly follows the proposition of Ide et al. (1997), with the exception that $\mathbf{c}$ is used to describe the model state (chemical concentrations) to hint at its functional character and to avoid confusion with a spatial vector commonly referred to as $\mathbf{x}$. The probabilistic aspect inherent in the definition of data assimilation in the beginning of this chapter is dealt with by using error covariance matrices and by defining the confidence in the validity of the data as inversely proportional to its error covariance. In this way, the optimal description corresponds to a minimum in the cost function. In the following, the space variables $\mathbf{r}$ and $\mathbf{s}$ will be dropped to obtain a more concise notation.

The chemistry-transport model constitutes an initial value problem and can be understood as the application of a nonlinear model operator $\mathcal{M}$: $\mathbf{c}(t_i) = \mathcal{M}\mathbf{c}(t_0)$. For small variations $\delta\mathbf{c}$ of $\mathbf{c}$, which are of interest here, the nonlinear operator $\mathcal{M}$ can be replaced by the successive application of a linear operator $\mathbf{M}$ which is obtained from $\mathcal{M}$ as described by

$$\mathcal{M}(\mathbf{c_0} + \delta\mathbf{c}) = \mathcal{M}(\mathbf{c_0}) + \left.\frac{\partial\mathcal{M}}{\partial\mathbf{c}}\right|_{\mathbf{c}=\mathbf{c_0}} \delta\mathbf{c} + \mathbf{O}(\delta\mathbf{c^2}) \ .$$

Thus, with $\left.\frac{\partial\mathcal{M}}{\partial\mathbf{c}}\right|_{\mathbf{c}=\mathbf{c}_0} =: \mathbf{M}$ and considering the temporal aspect,

$$\delta\mathbf{c}\,(t_i) = \mathbf{M}\,(t_i, t_{i-1})\,\mathbf{M}\,(t_{i-1}, t_{i-2}) \cdots \mathbf{M}\,(t_1, t_0)\,\delta\mathbf{c}\,(t_0) \ . \tag{2.2}$$

We define a scalar product$< \cdot, \cdot >$ by $< \mathbf{a}, \mathbf{b} >= \sum_{\mathbf{r}} \mathbf{a}^T(\mathbf{r})\mathbf{b}(\mathbf{r})$ and rewrite the cost function (Equation 2.1) as

$$\begin{aligned} J = \ & \tfrac{1}{2} < \mathbf{c}(t_0) - \mathbf{c}^b(t_0), \mathbf{B}_o^{-1} \left[\mathbf{c}(t_0) - \mathbf{c}^b(t_0)\right] > \\ & + \tfrac{1}{2} \textstyle\sum_{i=0}^{n} < \mathbf{Hc}(t_i) - \mathbf{y}^o(t_i), \mathbf{R}^{-1} \left[\mathbf{Hc}(t_i) - \mathbf{y}^o(t_i)\right] > \ . \end{aligned} \tag{2.3}$$

The scalar product ensures that the following expression holds for small variation of J:

$$\delta J =< \nabla_{\mathbf{c}} J, \delta\mathbf{c} > \ ,$$

or, as in Equation 2.3,

$$\delta J =< \nabla_{\mathbf{c}(t_0)} J, \delta\mathbf{c}(t_0) > + \sum_{i=0}^{n} < \nabla_{\mathbf{c}(t_i)} J, \delta\mathbf{c}(t_i) > \ .$$

Using Equation 2.2, one obtains

$$\begin{aligned} \delta J \ & =< \nabla_{\mathbf{c}(t_0)} J, \delta\mathbf{c}(t_0) > \\ & + \textstyle\sum_{i=0}^{n} < \nabla_{\mathbf{c}(t_i)} J, \mathbf{M}\,(t_i, t_{i-1})\,\mathbf{M}\,(t_{i-1}, t_{i-2}) \cdots \mathbf{M}\,(t_1, t_0)\,\delta\mathbf{c}(t_0) > \ . \end{aligned} \tag{2.4}$$

Thus, the variation of J can be ascribed to variations of the initial concentrations. Using the adjoint operator $\mathbf{M}^*$ of $\mathbf{M}$ (which is the transpose $\mathbf{M}^T$), δJ can be expressed by

$$\begin{aligned} \delta J \ & =< \nabla_{\mathbf{c}(t_0)} J, \delta\mathbf{c}(t_0) > \\ & + \textstyle\sum_{i=0}^{n} < \mathbf{M}^T\,(t_1, t_0) \cdots \mathbf{M}^T\,(t_i, t_{i-1})\,\nabla_{\mathbf{c}(t_i)} J, \delta\mathbf{c}(t_0) > \ . \end{aligned} \tag{2.5}$$

Making use of the linearity of the scalar product, Equation 2.5 becomes

$$\delta J = < \mathbf{B}_o^{-1}[\mathbf{c}(t_0) - \mathbf{c}^b(t_0)], \delta\mathbf{c}(t_0) >$$

$$+ \sum_{i=0}^{n} < \mathbf{M}^T(t_1, t_0) \cdots \mathbf{M}^T(t_i, t_{i-1}) \, \mathbf{H}^T\mathbf{R}^{-1}[\mathbf{H}\mathbf{c}(t_i) - \mathbf{y}^o(t_i)], \delta\mathbf{c}(t_0) > \quad . \tag{2.6}$$

The gradient with respect to the initial concentrations is thus given by

$$\nabla_{\mathbf{c}(t_0)} J = \mathbf{B}_o^{-1}[\mathbf{c}(t_0) - \mathbf{c}^b(t_0)]$$
$$+ \tfrac{1}{2} \sum_{i=0}^{n} \mathbf{M}^T(t_1, t_0) \cdots \mathbf{M}^T(t_i, t_{i-1}) \, \mathbf{H}^T\mathbf{R}^{-1}[\mathbf{H}\mathbf{c}(t_i) - \mathbf{y}^o(t_i)] \; . \tag{2.7}$$

Together with $\mathbf{c}(t_0)$ and $J(\mathbf{c}(t_0))$, the gradient can be used in a minimization procedure to determine $\mathbf{c}(t_0)$ with the smallest $J(\mathbf{c}(t_0))$, taken as the most probable state of the atmosphere.

The corresponding phase space where the zero search is to be performed is of the dimension grid points times number of chemical species, which is (96∗71+2)∗10∗41 = 2795380 for the present COMMA-version.

This method is illustrated in Figure 2.1 for a scalar valued function: having performed an integration of the direct model, the distance of the model state to the available information can be determined as $(\mathbf{H}\mathbf{c}(t_i)) - \mathbf{y}^o(t_i))$. The adjoint model is then integrated backward in time starting at T_{end}. Whenever there is a discrepancy between direct model and measurement, the weighted difference given by $\mathbf{H}^T\mathbf{R}^{-1}[\mathbf{H}\mathbf{c}(t_i) - \mathbf{y}^o(t_i)]$ is added to the adjoint of $\mathbf{c}(t_i)$. This contribution is referred to as the observational **forcing term**. The adjoint field can thus be understood as the gradient of the cost function at this point in phase space. The information contained in the measurements is used for other components of $\mathbf{c}(t_i)$ as well if their correlation is expressed in the weighting matrices. The gradient of the cost function at t_0 indicates in which direction the initial values have to be changed to give closer correspondence of model and observations. The flowchart in Figure 2.2 illustrates where the input data are used within the program.

So far, we have regarded an initial value problem, and the initial concentrations are therefore named **control variables**. The algorithm can be extended to the use of other control variables such as boundary values or, for tropospheric cases of special importance, to emission rates (see for example Elbern et al. (1999a, 2000)).

2.2 Alternative approaches

4D var data assimilation can be motivated from the point of view of control theory. The concept of controllability can be described as the idea of introducing a deterministic forcing term in the evolution equation to drive the system toward a pre-specified state within a certain period of time (Todling,

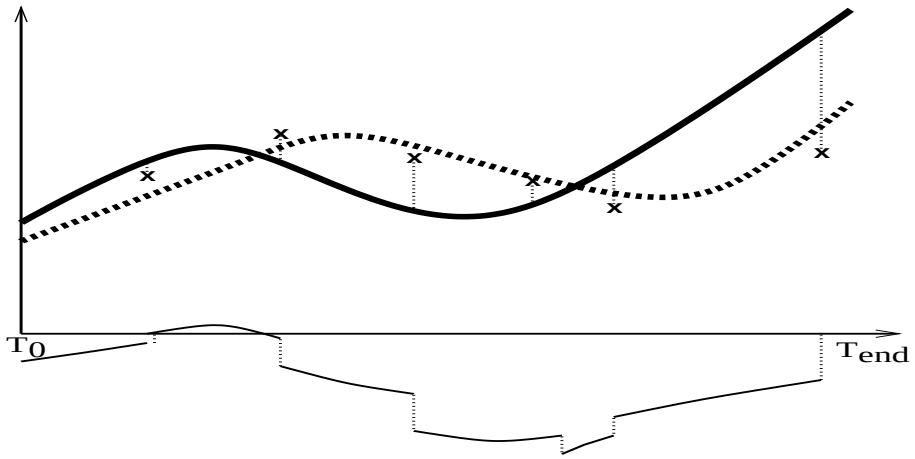

Figure 2.1: *Principle of 4D var data assimilation: the thick continuous line indicates the first direct model trajectory, the dashed line the optimized direct model trajectory.* **x** *indicate measurements, the thin continuous line refers to the trajectory of the adjoint model where discontinuities are due to forcing by observations.*

1999). In 4D var, this is obtained by the use of the cost function and the variational principle. Kalman filtering constitutes a different approach to the data assimilation problem and stems from estimation theory. Thus, it usually involves a sequential estimation process with a melding scheme that is based on a minimization of the expected error of the estimate in terms of the statistics of both model and data errors (Todling, 1999). The term model error refers to the deviation of the forecast prediction from the true evolution (Bouttier and Courtier, 1999). The Kalman filter propagates the error covariance matrices in time which results in huge computational demands that have so far hindered the implementation of a complete Kalman filter in atmospheric modelling. However, in contrast to the iterative procedure in 4D var, only one integration is required. For this reason, different simplifications of the Kalman filter have been developed, which are used in atmospheric modelling.

A reduced rank square root Kalman filter for a tropospheric CTM is used by van Loon et al. (2000). The name of the method refers to the approximations of the error covariance matrices employed in this implementation.

In general, the Kalman filter takes into account a model error. In the special situation, where the model is assumed to be perfect, the analysis of the complete Kalman filter and the optimal analysis of 4D var are equivalent at time T_{end}, the end of the considered assimilation period. Because of its smoothing characteristics, 4D var provides a smoothed trajectory throughout the assimilation interval, but in contrast to the Kalman filter, it does not provide an estimate of the quality of the analysis.

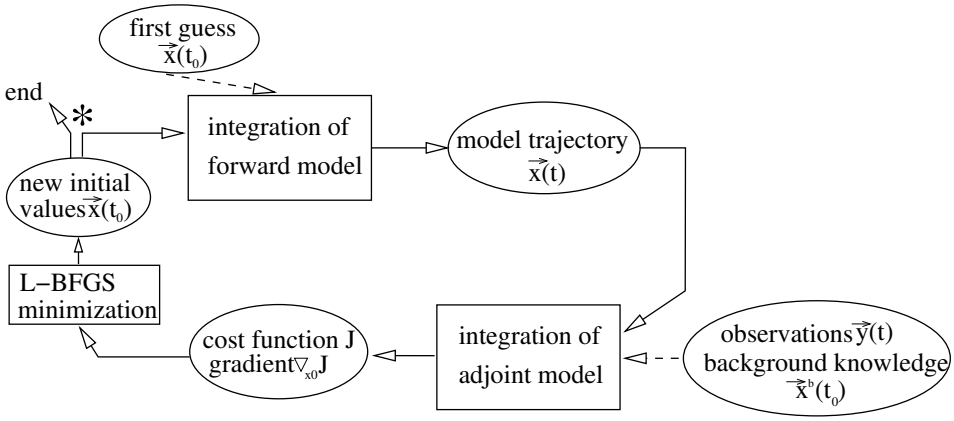

Figure 2.2: *Role of first guess, background and observations in the integration of the AMMOC-CTM. At $*$ the program is terminated if a maximum number of iterations is reached or if the cost function is small enough.*

Within the 4D var data assimilation approach it is also possible to allow for a model error and thus consider the model equations to be a soft constraint.

Another data assimilation method that should be mentioned here is 4D-PSAS (Physical-space Statistical Analysis). The method belongs to the category of variational approaches, but minimization is performed in observation space, which often has a smaller dimension than the model space. Courtier (1997) showed that under the perfect model assumption 4D var and 4D-PSAS give the same result with the same cost.

For further information, the interested reader can consult the following papers describing the various data assimilation methods in more detail: Talagrand and Courtier (1987); Daley (1991); Talagrand (1991, 1997); Robinson et al. (1998); Bouttier and Courtier (1999); Todling (1999).

CHAPTER 3

The CRISTA-Instrument

The **CR**yogenic **I**nfrared **S**pectrometer and **T**elescopes for the **A**tmosphere consists of three telescopes with four spectrometers which measure the infrared emission of more than 15 atmospheric trace gases in the height range from 8 km to 150 km depending on the measurement mode (Offermann et al., 1999). The instrument performed two missions on the free flying **S**huttle **Pa**llet **S**atellite (SPAS) of the Space Shuttle in November 1994 (STS 66) and August 1997 (STS 85). CRISTA is a limb-scanning instrument and achieves its vertical resolution by means of successive scans at different elevation angles (see Fig. 3.2). CRISTA measurements are characterised by a high horizontal resolution (see Fig. 3.1) due to the use of three telescopes with viewing directions 18° apart and helium cooling, which makes high measurement frequency possible. CRISTA is the first instrument combining high sensitivity, sufficiently high spectral resolution, and a high spatial density of measurement points in all three dimensions (Grossmann, 2000). Latitudinal coverage extended from 67° north to 57° south on the first mission and was increased to about 74° in both hemispheres on the second mission by slewing all the telescopes to point poleward at high latitudes. The size of the air mass sampled by one measurement is determined by the measurement geometry. Fig. 3.2 displays the instrument's line of sight in the atmosphere. In principle, the emissions of all molecules along this line contribute to the detector signal recorded by the spectrometer. The most important contribution is due to molecules situated at altitudes between the tangent height and the satellite height (300 km). Those molecules at a great distance which are situated above may be neglected because of the attenuation of the signal with increasing distance. Under the assumption of a constant mixing ratio of the emitting species, 50% of the signal originate

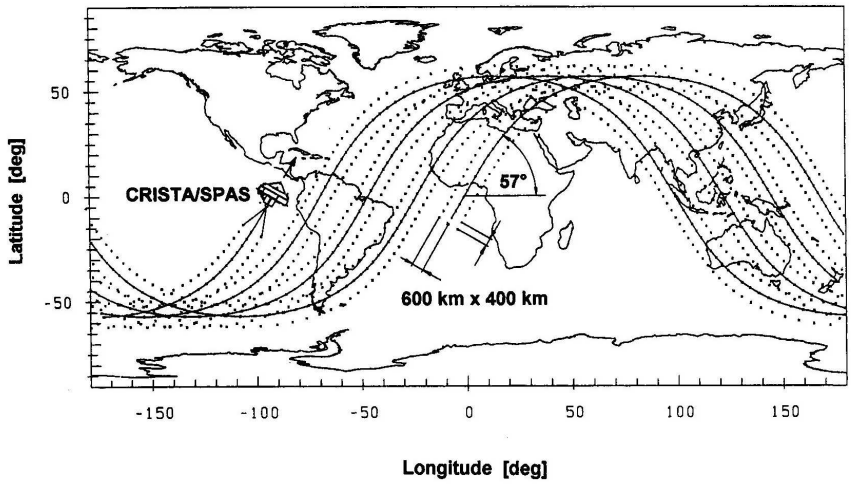

Figure 3.1: *Flight track of the CRISTA-SPAS which carried the CRISTA instrument. Solid lines indicate the flight track and the measurement locations for the center telescope, dotted lines indicate the measurement locations for the two lateral telescopes. The resolution of 600 km × 400 km is valid for stratosphere-mesosphere mode (16-79 km altitude, 55 hours of data); in stratosphere mode, it was increased to 600 km × 200 km (16-44 km altitude, 77 hours of data). From Riese et al. (1999a).*

from a 2 km thick layer above the tangent point (Riese et al., 1999a). In the case of strong vertical gradients, the contribution of this layer can even amount to 80% of the signal (Spang et al., 1997). The CRISTA analysis volume element measures 20 km across track, 2 km in the vertical, and 200 km along track according to Grossmann (2000) or 300 km according to Riese et al. (1999a). In order to match the high horizontal resolution of the CRISTA instrument and to reproduce the resolved small-scale structures (see for example Fig. 11.1), the resolution of the COMMA model grid was increased from the standard (64*35+2) grid boxes to (96*71+2) grid boxes per layer (see Chapter 5). In the vertical, linear interpolation is performed between concentrations at different tangent heights to obtain the concentration at the model levels. The zonal and meridional length of the sampled air volume for different latitudes are calculated and compared to the COMMA resolution in Appendix C. As the horizontal extension of the analysed air volumes is mostly smaller than the extension of the COMMA grid boxes, each measurement is attributed to the closest model grid point. Concerning the temporal resolution, all measurements between $t - \frac{\Delta t}{2}$ and $t + \frac{\Delta t}{2}$, where Δt= 4 min. denotes the model time step, are assumed to be taken at t. Detailed error statistics necessary for 4D var data assimilation were provided by the CRISTA group for CFC-11, O_3, N_2O, HNO_3, $ClONO_2$ and

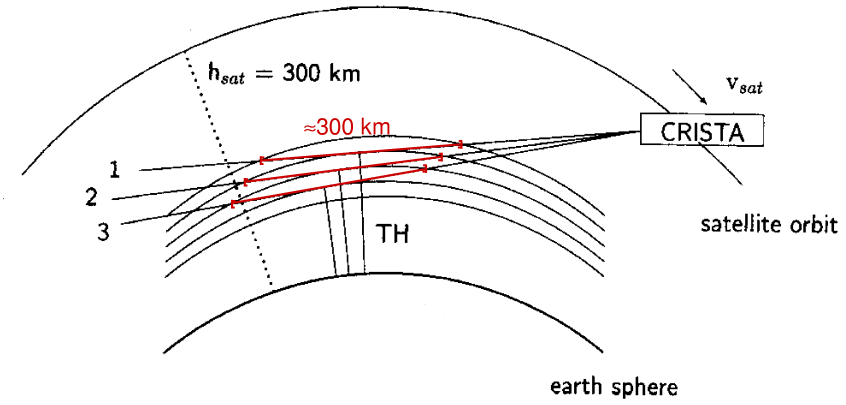

Figure 3.2: *Measurement geometry of the limb-scanning CRISTA instrument. The marked segments indicate the path through the atmospheric layer to which the signal is attributed. TH denotes the tangent height, which is the altitude of the tangent point, of the lines of sight. From Riese et al. (1999a).*

CH_4. The measurements of these species are employed in the present work. The horizontal data density depends on the measurement mode. Mode 1 delivered data for the stratosphere and mesosphere up to 79 km altitude. The horizontal data density is reduced compared to measurement mode 2, where the stratosphere was sampled up to an altitude of 44 km only. Over the period of some hours, oversampling and detector tests were carried out. The sampling durations of the different modes are listed in Table 3.1. The systematic error component of the retrieved trace gas mixing ratios includes errors due to calibration problems, instrument effects, uncertainties of the spectral parameters used for the retrieval, uncertainties of the forward radiance module, and errors of the retrieved temperature profiles that enter the trace gas retrieval. Sources of the random error component are detector noise, raw data correction, wavelength reconstruction, and tangent height reconstruction (Riese et al., 1999a). Both error components have to be considered in the 4D var procedure since the systematic error component cannot be subtracted from the observations.[1] To display CRISTA measurements, interpolation has been performed onto a $2^\circ \times 2^\circ$ grid, which has a higher resolution than the model grid but is a lower limit to the measurement resolution in most areas except for the higher latitudes (see Appendix C).

[1]The term systematic error is employed in the sense of measurement *accuracy*. The systematic error may contain a bias that could be removed if it was known. This bias might show a dependence on multiple factors such as meteorological situation and altitude.

Day	mode 1 's/m' [h]	mode 2 's' [h]	other modes [h]
308:12-309:12	19h20	—	—
309:12-310:12	4h30	18h20	—
310:12-311:12	—	24h	—
311:12-312:12	—	23h50	—
312:12-313:12	15h30	—	—
313:12-314:12	15h55	—	8h05
314:12-315:12	—	7h15	16h35h
315:12-316:12	3h45	9h00	—

Table 3.1: *Measurement mode durations [hours] for the 24 hour assimilation periods. Mode 1 is stratosphere-mesosphere mode, mode 2 is stratosphere mode with increased horizontal data density in the stratosphere. Other modes refer to detector checks and oversampling testing times. The julian days 308–316 correspond to Nov. 4–Nov. 12.*

3.1 CRISTA measurement campaign in November 1994

The CRISTA instrument was utilised for the first time during the **At**mospheric **L**aboratory for **A**pplications and **S**cience (ATLAS)-3 space shuttle mission, which took place between November 3 and 12, 1994. In addition to CRISTA, the **A**tmospheric **T**race **Mo**lecule **S**pectroscopy (ATMOS) instrument and **M**illimeter-wave **A**tmospheric **S**ounder (MAS) on the space shuttle and other space-born instruments observed the atmosphere: the **U**pper **A**tmosphere **R**esearch **S**atellite (UARS) carried the **M**icrowave **L**imb **S**ounder (MLS) and the **Hal**ogen **O**ccultation **E**xperiment (HALOE), which measured ozone. In addition, the **S**tratospheric **A**erosol and **G**as **E**xperiment (SAGE) II and **P**olar **O**zone and **A**erosol **M**easurement (POAM) II instruments delivered data during this period. A coordinated campaign including ground-based, airplane, balloon, and rocket observations permitted extensive validation through measurement intercomparison. The meteorological conditions in the stratosphere during the ATLAS-3 mission are described in Manney et al. (1996). While the northern hemisphere polar vortex had started to develop above 35 hPa and was slightly shifted towards 0° longitude, the southern hemisphere polar vortex, which had started to decay, was still strong below 16 hPa. It was shifted towards 270° longitude at all levels. The above authors also examined high-resolution potential vorticity fields, and found indications of atmospheric variability relevant for trace gas transport, which was stronger than the meteorological analyses indicated.

The ozone observations by the above mentioned instruments have been compared in Manney et al. (2001) by mapping them to equivalent latitude–

potential temperature space. They found agreement between the instruments within 0.5 ppmv or 5 % in the upper stratosphere and 0.25 ppmv in the lower stratosphere, and explained larger differences in the mid-stratosphere as sampling differences. The method of Manney et al. considers the meteorological conditions of the sampled air mass, but needs additional evaluation if the lifetime of ozone is comparable to or shorter than the timescales for dynamical changes. Further, it needs reconsideration if some chemically driven changes are relevant that may not correlate well with PV (see Manney et al. (2001)). In further studies, other trace gases have been investigated as well: partitioning within the odd nitrogen family (NO + NO_2) with a focus on the northern hemisphere has been examined in Riese et al. (2000). The investigation was extended globally and included horizontal distributions of NO_2 in Küll et al. (2002). Chlorine nitrate tracer studies were carried out in Riese et al. (1999a). CFC-11 as a dynamical tracer in the lower stratosphere, especially in the polar vortices, was analysed in Spang et al. (1997). Smith and Riese (1999) detected inertial instability in temperature measurements, which were confirmed through small perturbations in methane and ozone. In Riese et al. (1999b) a simple direct insertion assimilation scheme was used to assimilate CFC-11, nitrous oxide and methane into the NCAR ROSE CTM. Bacmeister et al. (1999) employed isentropic trajectory mapping for comparison with aircraft observations of ozone and CFC-11 and for the comparison of HNO_3 with aircraft observations of odd nitrogen. Errera and Fonteyn (2001) were the first to use an advanced data assimilation system for CRISTA data. They validated the assimilation result by comparison with ATMOS and HALOE data.

CHAPTER 4

Short summary of the dynamics of the stratosphere

Interest in the dynamics of the middle atmosphere in the context of chemical data assimilation originates from the strong influence of dynamics on the chemistry of the middle atmosphere. Atmospheric trace gases can be chemically inactive in the source regions near the surface of the earth and become active after transport to the middle atmosphere. For example, CFC-11 is emitted in the lower troposphere and transported to the stratosphere where it undergoes photolysis and can finally cause ozone depletion. On the other hand, chemistry is also important for dynamics due to possible modifications of the radiative flux divergence in the atmosphere. This is particularly true for ozone as a strong absorber of solar UV radiation.

To judge the importance of transport for the concentration of a given trace gas, one compares its chemical timescale (half life due to chemical destruction) to the characteristic transport timescales. If the chemical lifetime is much larger than the transport timescales, the species will eventually be homogeneously distributed, unless the strength of the source varies strongly. For example, N_2 and O_2 are homogeneously distributed in the lower and middle atmosphere. As atmospheric velocities are strongly anisotropic, one has to distinguish meridional, zonal and vertical timescales. On the other hand, if the transport timescales are much larger than the chemical timescale, species relax towards chemical equilibrium before transport can significantly redistribute them. Some chemistry-transport models take advantage of this feature by introducing the family concept. For example, the interconversion reactions between O_3, O^3P and O^1D are so fast that these three species can be treated as one (named odd oxygen family) for transport calculations and afterwards redivided into individual members before performing subsequent chemistry calculations. The family concept is not used in the model

presented here because it is not advisable for adjoint calculations: for the adjoint model, the redivision into individual members is difficult to treat.

One encounters a more difficult situation when the chemical timescale is approximately equal to one of the transport timescales. Then, detailed information about atmospheric dynamics and chemical reactions is needed to analyse the species' atmospheric distribution. Figure 4.1 shows the vertical distribution of several important trace gases. For example, tropospheric production of nitrous oxide (N_2O) is due to soil bacteria. Its lifetime in the troposphere and lower stratosphere lies in the range of 10–100 years. In the middle stratosphere, however, its chemical lifetime becomes comparable to transport timescales. As a result, its mixing ratio decreases with altitude, and N_2O is an interesting tracer to examine transport processes.

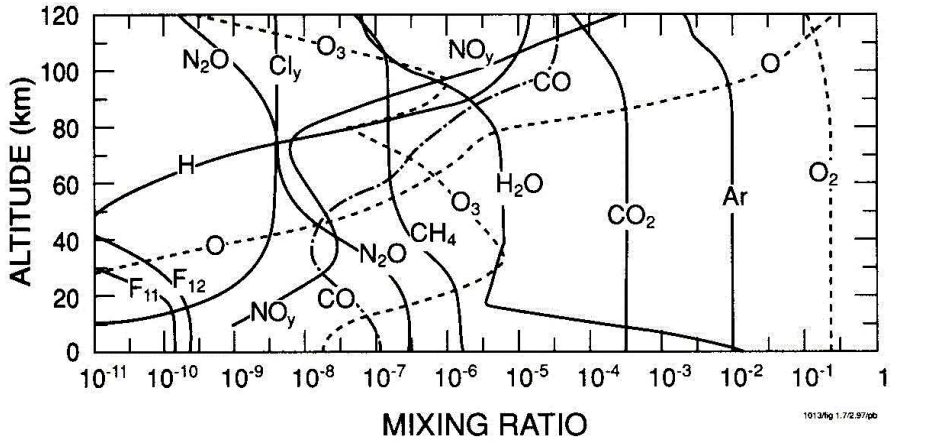

Figure 4.1: *Average profiles of atmospheric trace gases up to 120 km altitude. From Brasseur et al. (1999).*

Transport from the troposphere to the stratosphere takes place mostly in the tropics. At mid-latitudes, stratosphere-troposphere exchange can occur through mesoscale events such as tropopause folds, cut-off lows, streamers, and the sinking motion of the tropopause in spring. These mid-latitudinal exchange mechanisms are of special importance for the budget of the lowermost stratosphere, as they are not followed by large-scale upward transport into the middle stratosphere. The energy for the large-scale rising motion in the tropics stems from intensive insolation stored in the form of latent heat. This results in the formation of large convective clouds. These clouds often penetrate through the tropopause, which is situated at approximately 18 km altitude in the tropics, into the stratosphere.

The stratosphere is characterised by strong static stability due to the temperature increase through the absorption of solar radiation by ozone. The static stability slows down vertical motion, so that horizontal movement clearly dominates stratospheric transport. In the lower stratosphere,

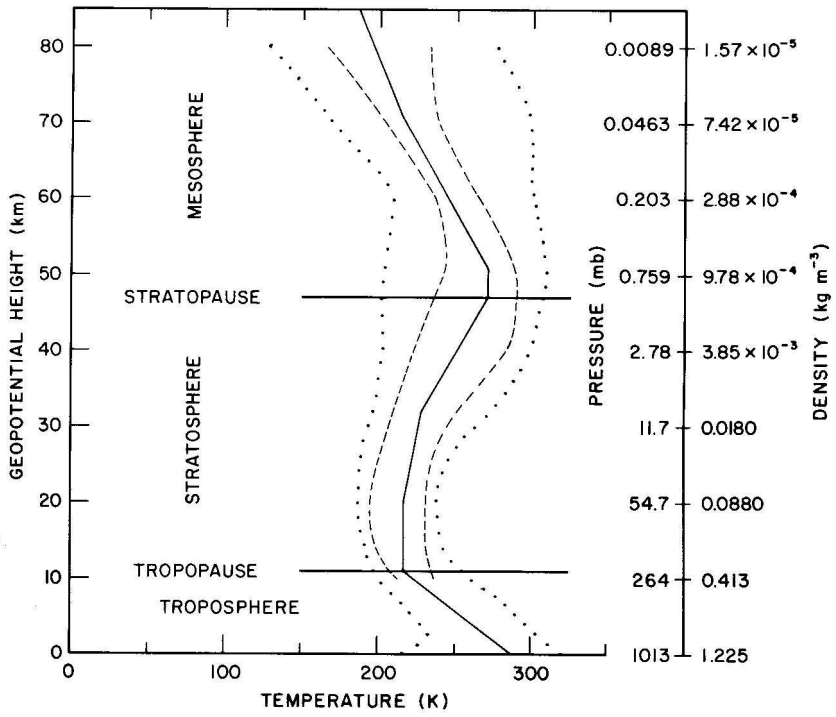

Figure 4.2: *Temperature profile of the US standard atmosphere (1976). Dashed lines show the lowest and highest monthly mean temperatures obtained for any location between equator and poles, whereas the dotted line shows estimates of the 1% maximum and minimum temperatures that occur during the warmest and coldest months, in the most extreme locations. From Gill (1982).*

the rising motion in the tropics is followed by poleward transport with a dominance for transport towards the winter pole. Above 30 mbar, the dominant zonal movement is characterised by winter westerlies and summer easterlies due to the temperature gradient between the summer and the winter pole. The much weaker meridional circulation from the summer to the winter pole is responsible for rising at the summer and sinking at the winter pole. This circulation is driven by waves, especially Rossby waves in the winter hemisphere. In a mid-latitude region called the surf zone, breaking of Rossby waves is responsible for mixing processes, which smooth latitudinal concentration gradients. Poleward of the surf zone, the polar vortex edge is formed by strong zonal winds and strong potential vorticity gradients that hinder meridional exchange processes.

Wave-mean flow interactions dominate the zonal wind structure in the tropics. They lead to the creation of the quasi-biannual oscillation (QBO), a long-period variation (of about 27 months) with descending regions of

easterlies and westerlies. The QBO can be observed between 10 and 30 km altitude, in a latitude band extending 20–25° into both hemispheres. Above the QBO, zonal wind changes are characterised by a semi-annual oscillation (SAO) with easterlies during equinoxes and westerlies during solstices.

In the mesosphere, temperature decreases with altitude and vertical displacement occurs at a faster rate. This vertical structure up to the mesopause is shown in Figure 4.2. Above the mesopause, at about 100 km, the absorption of solar radiation by atomic oxygen leads again to a temperature increase.

Knowledge about transport processes in combination with chemical conversion reactions is needed for the verification and interpretation of synoptic maps produced by the assimilation of remote sensing data in chemistry-transport models.

CHAPTER 5

The Cologne Model of the Middle Atmosphere: COMMA

The **Co**logne **M**odel of the **M**iddle **A**tmosphere (COMMA) is a three-dimensional Eulerian model that was originally developed to investigate the dynamical behavior of the stratosphere and mesosphere and the influence of radiation on both. It originated in a hemispheric model developed by Klinker (1981) and Rose (1983). Jakobs (1986) extended its domain into the thermosphere and into a global model and introduced additional physical processes which are relevant for the upper part of the middle atmosphere, particularly gravity wave breaking and dissipation. COMMA is a mechanistic model which now includes a detailed treatment of the radiation budget. It has been used for the simulation of dynamical consequences of the Antarctic ozone hole (Dameris et al., 1991) and for calculations of the dynamics and the energy budget at the mesopause (Berger and Ebel, 1996). A description is given by Ebel et al. (1995). In a subsequent development phase, a chemistry module for the domain below 80 km and a transport module were implemented. The addition of these modules allows for transport studies (Günther and Dameris, 1995) and examinations of the chemical behavior of the middle atmosphere (Hendricks et al., 2001). Baier (2000) developed an adjoint model of the dynamics module to assimilate wind and temperature fields. The assimilation system provided improved ozone forecasts for middle and high latitudes.

For the present study, a chemistry-transport-model version named COMMA-CTM was designed, which uses meteorological analysis as input for both the transport and the chemistry module. To this end, the dynamical part of the model was disentangled from the chemistry-transport part and replaced by routines that supply wind and temperature fields. These may be for example analyses from General Circulation Models (GCMs) like the

ECMWF model or the UKMO model.

The time evolution of the atmospheric state is described by a system of coupled advection-diffusion-chemistry equations,

$$\frac{\partial c_i}{\partial t} = -\nabla(\mathbf{u}c_i) + \nabla(K\nabla c_i) + f_i(\mathbf{c}) + E_i \ . \tag{5.1}$$

Here, c_i refers to the mixing ratio of the i-th model species, and $\mathbf{c}$ denotes the vector of all mixing ratios. The f_i represent the chemical reactions, which are described by the difference between production and loss reaction: $f_i(\mathbf{c}) = P(\mathbf{c}) - L\dot{c}_i$. The E_i denote additional source and sink terms, for example emission or sedimentation, and $\mathbf{u}$ is the wind field. In the present case it is given by the analyses of the United Kingdom Meteorological Office (UKMO) for the UARS project (Swinbank and O'Neill, 1994). Equation 5.1 defines an initial value problem. The horizontal discretization of the dynamical equations uses the Arakawa A-grid (Fig. 5.2) oriented along latitudes and longitudes. The grid for the chemistry-transport equations is shifted with respect to this grid. For these calculations, temperature and vertical wind speed are needed at the center of the grid box while the component of the wind field perpendicular to the boundaries is needed at the boundaries of the grid box. Therefore, wind fields and temperature must be interpolated. The southernmost and northernmost grid boxes are combined to form a so-called polar box to avoid the existence of triangular grid boxes. For the present work, the horizontal grid resolution has been increased from (64×35+2) to (96×71+2) grid points corresponding to a resolution of 3.75°long×2.5°lat. This choice matches the resolution of the UKMO analyses. While the horizontal resolution of the COMMA grid was increased, the vertical resolution was kept at 10 logarithmic pressure levels up to 0.408 hPa with a spacing of 5.75 gpkm. As the COMMA grid is shifted horizontally with respect to the UKMO grid for some parameters, the horizontal wind fields are interpolated in longitudinal direction while the temperature fields are interpolated in zonal direction. In the vertical, cubical spline interpolation was used to determine wind- and temperature fields at the COMMA altitudes.

The advection and the chemical transformation part of Equation 5.1 are solved sequentially. This separation is called operator splitting. For the chemical transformation of the atmospheric constituents the incoming solar radiation is of importance. Its intensity is determined mostly by the solar zenith angle. The photolysis rates are calculated by interpolation with respect to the ozone column, the solar zenith angle and the geometric height. We use a precalculated lookup-table for 34 photolysis reactions for this task. Besides these photolysis reactions, 114 reactions of second and third order are considered in the chemical mechanism which are solved using the second order Rosenbrock method. The reaction rates are taken from Hendricks et al. (2001). The Fortran code was generated by the **K**inetic **P**re**P**rocessor (KPP) (Damian-Iordache, 1996). This part of the model development was

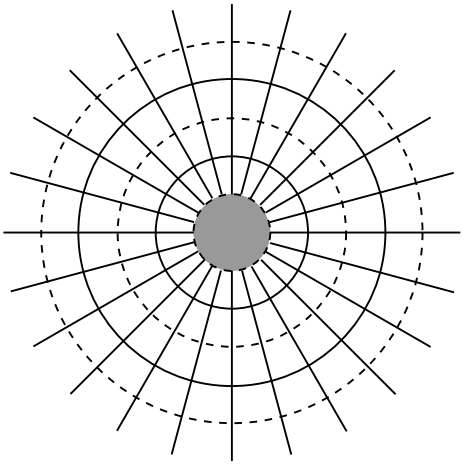

Figure 5.1: *Model grid of the AMMOC-CTM: dynamics grid (solid) is shifted with respect to the chemistry grid (dashed). At the poles, one box (shaded grey) covers all longitudes, meridional transport is calculated for all boundaries.*

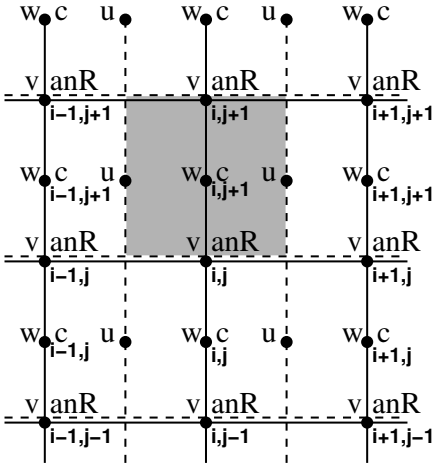

Figure 5.2: *Model grid of the AMMOC-CTM: indicated are the positions of the model state variables: anR: wind- and temperature; u,v,w: Courant numbers (zonal, meridional and vertical) for transport calculations; c: tracer concentration. The anR are the state variables of the dynamics kernel and used for grid classification according to Arakawa and Lamb (1977).*

carried out by A. Klyuchnikova and J. Schwinger. The automation by KPP implies that changes in the chemical mechanisms can be performed more easily than in the case of hand-coding. Another advantage of KPP lies in its capacity to efficiently exploit the sparsity of the Jacobian. The entry (ij) of the Jacobian is different from 0 if the species i and j react with each other. In large atmospheric reaction mechanisms, usually only about 10 % of the entries are different from 0. KPP arranges the reaction equations such that the matrix entries different from 0 are arranged numerically favorable. Because heterogeneous reactions are not yet implemented in this model version, its application may be limited to periods where the influence of PSCs and sulfate aerosols is small. The identical twin experiments have been carried out accordingly. During the time period chosen for the real case experiment, no PSCs were observed. The influence of sulfate aerosols is discussed in Chapter 11.

Advection of the atmospheric species is calculated according to the Bott transport algorithm (Bott, 1989, 1992). Günther (1995) tested different transport algorithms, namely Smolarkiewicz, fourth-order Bott (monoto-

nous and nonmonotonous), Semi-Lagrange and Prather. His results showed that the Bott algorithm is the best choice as a compromise between precision and numerical demands. The idea of the Bott algorithm shall be demonstrated for the one-dimensional case: Crowley (1968) introduced the idea of using polynomials to approximate the tracer distribution and thereby obtain higher order accurate schemes. In this way, the tracer concentration c_j in the j-th grid cell x_j is approximated by a polynomial of the order l: $c_{j,l} = \sum_{k=0}^{l} a_{j,k} x'^k$ where $x'^k = \frac{(x-x_j)}{\Delta x}$ (with $-0.5 < x'^k < 0.5$) denotes the locations within j-th grid cell of length Δx. The coefficients $a_{j,k}$ are determined from the concentration c_j given at the grid points j. These coefficients as well as the Courant numbers (wind speed normalised to the grid cell size) at the boundaries are then employed to calculate the flux through the lateral boundaries of the grid cells. By flux limitation and weighting the calculated fluxes, care is taken with respect to the following issues:

- Weighting compensates for the fact that the integral of the fitted polynomial $c_{j,l}$ over the grid cell is not identical to $c_j \Delta x$.
- The sum of fluxes leaving a cell must be limited by the content of the cell.
- To avoid numerically unstable situations, at least a minimum quantity ϵ should remain in the cell.

In the three-dimensional case, changes due to zonal, meridional and vertical transport are calculated separately and the sum, limited by the total mass in the box, is subtracted from the tracer field. In contrast to semi-lagrangian transport algorithms as employed in Errera and Fonteyn (2001), the Bott transport algorithm is mass conserving. Additionally, it is positive definite. As the model resolution was increased to (96×71+2) horizontal grid points, the transport time step had to be adapted. It was chosen as 4 minutes to satisfy the Courant criterion ($\frac{u\Delta t}{\Delta x} < 1$) also at high latitudes where the grid cell size in zonal direction, Δx, becomes smaller. This guarantees that the content of a cell is not transported further than to the next grid cell during one time step. As chemical transformation and transport are calculated alternatingly, the outer chemical time step and thus the maximum inner chemical time step were also set to 4 minutes.

5.1 Modifications of the COMMA-CTM for adjoint model development

The development of the adjoint model code required some changes to the COMMA-CTM in order to keep the system numerically stable. In the advection routines, the weighting of the calculated fluxes is stabilized numerically

against division by zero through addition of a small number. As derivation for the adjoint code leads to a square of this number in the denominator, it had to be increased to remain distinct from zero for the given machine precision. As the family concept is not suitable for adjoint calculations, the solver was changed to the Rosenbrock method treating all species separately.

CHAPTER 6

Development of the adjoint model

The adjoint model can be obtained either by deriving the continuous adjoint equations from the tangent-linear continuous forward model equations and then formulating the finite-difference program code of the continuous adjoint equations ("finite difference of adjoint") or by deriving the finite-difference adjoint equations directly from the finite difference of the forward model ("adjoint of finite difference"). Sirkes and Tziperman (1997) have compared the two approaches for a primitive equations ocean general circulation model and came to the conclusion that, when only the gradient at the initial time is needed, one may use the adjoint of finite difference formulation, even though the adjoint solution may contain strong computational modes which are legitimate from a numerical point of view. The present work, where the main interest is in the gradient at the initial time, one encounters the above described situation. Hence, the adjoint of finite difference method was employed because we can use automatic adjoint compilers for this purpose. Chapter 7 describes two possible approaches implemented in the AMMOC-CTM to alleviate the problem of computational modes. The disadvantage of the finite difference of adjoint approach is seen to lie in the fact that it is accurate to only within $O(\Delta x, \Delta t)$. Sandu et al. (2002) emphasized that the use of the adjoint of finite difference approach has the advantage that the computed gradient is exact relative to the computed cost function. Further on, this procedure supports the principle of locality and readability called for by Talagrand (1991). Locality means that the adjoint model is constructed in a way that local changes in the forward model only require local changes in the adjoint model. Readability means that the adjoint code should be written in such a way as to enable any programmer to easily determine the correspondence between the forward and the adjoint model.

This can be fulfilled by the adjoint of finite difference approach as there is close correspondence between a line of code in the forward model and the related program code in the adjoint model. In addition, care should be taken to use a transparent notation, so that changes in the forward model can be performed and the location for the corresponding changes in the adjoint code can be determined easily. This allows one to keep the adjoint model system up to date with current forward model developments. However, it should be noted that readability to a certain extent hinders source code optimization, or, that the optimization of the adjoint model system has to be performed with care as not to violate locality and readability. Errera and Fonteyn (2001) used the finite difference of adjoint approach for the chemistry integration and the adjoint of finite difference approach for the transport integration.

Once the adjoint code is developed, it can be used not only for 4D var data assimilation, but also to determine perturbations to a given field that amplify most rapidly. In meteorological applications, this is of special interesting in order to assess the forecast error a priori. Furthermore, it can be used to determine gradients for sensitivity or diagnostic purposes. For details, see (Talagrand, 1991).

6.1 The adjoint compiler O∂yssee

The adjoint model code has been created with the help of O∂yssee. O∂yssee has been developed at the **In**stitut pour **R**echerche en **I**nformation et **A**utomation (INRIA) in Sofia Antipolis, France. Several other compilers are now available which also create the tangent-linear code of a given model code in Fortran or other programming languages or even the adjoint code of the tangent-linear code. For details, see
http://www-unix.mcs.anl.gov/autodiff/adtools/index.html. O∂yssee was chosen because it was available in a version that could be implemented free of charge on the local system. In addition to the program as a sequence of elementary arithmetical operations, the adjoint compiler needs to be passed a list of the variables which are to be considered independent and to be optimized. The adjoint program code was tested according to the method proposed by Chao and Chang (1992) for different numerical situations. The idea of the method is as follows: $\mathcal{M} : \mathbf{c}(t_0) \rightarrow \mathbf{c}(t_n) = \mathcal{M}(\mathbf{c}(t_0))$ denotes the model operator on the input $\mathbf{c}(t_0)$ to produce the output $\mathbf{c}(t_n)$ which can also be written componentwise as $c_j(t_n) = [\mathcal{M}(c_1(t_0), c_2(t_0), \cdots, c_n(t_0))]_j$. Then, the equation

$$\nabla_{c_i(t_0)} J = \sum_j \left(\frac{\partial \mathcal{M}}{\partial c_i(t_0)} \right)_j \nabla_{c_j(t_n)} J$$

holds for the cost function J (Chao and Chang, 1992). Elements of the ma-

trix $\frac{\partial \mathcal{M}}{\partial c_i(t_0)}$ can be determined either from the adjoint code or by application of a perturbation to the forward code. If the adjoint code is correct, both deliver identical results up to some discretization error. Using zero except 1 in the i-th line as input vector to the adjoint routine gives $\mathcal{G} = \begin{pmatrix} \frac{\partial \mathcal{M}_1}{\partial c_i(t_0)} \\ \vdots \\ \frac{\partial \mathcal{M}_m}{\partial c_i(t_0)} \end{pmatrix}$. On the other hand, the forward model can be integrated from two starting values $\mathbf{c}$ and $\tilde{\mathbf{c}}$ differing slightly in the i-th component. The components of $\mathcal{M}(\mathbf{c})$ and $\mathcal{M}(\tilde{\mathbf{c}})$ can then be compared componentwise via the difference quotient

$$\frac{\mathcal{M}_j(c_1(t_0), \cdots, c_i(t_0), \cdots, c_n(t_0)) - \mathcal{M}_j(c_1(t_0), \cdots, \tilde{c}_i(t_0), \cdots, c_n(t_0))}{c_i(t_0) - \tilde{c}_i(t_0)} \quad .$$

This should equal the j-th line of $\mathcal{G}$, $\frac{\partial \mathcal{M}_j}{\partial c_i(t_0)}$. This test led to the increase in the addend mentioned in Chapter 5.1. Promising progress has been achieved by Sandu et al. (2002): KPP has been enhanced for a given set of chemical reactions to produce not only the forward model code for, among others, the second order Rosenbrock method, but also the adjoint of its finite difference formulation. If this proves to be reliable, it would eliminate the need for adjoint compilers for the chemical transformation part.

6.2 Examples of adjoint subroutines

To illustrate the basic principle and an example of possible pitfalls, two short subroutines and their adjoints shall be described here. The first example is taken from Giering and Kaminski (1998).

```
subroutine itworks(x,y,z)
real x,y,z
...
z=x*sin(y**2)
...
return
end
```

We now assume x and y to be the independent variables to be optimized and the equation to be the l^{th} line of code in the routine. Information is passed from x and y to z. Therefore, information has to be passed in the adjoint code from the adjoint of z, named zccl, to the adjoints of x and y, named xccl and yccl. Linearization of this line then gives

$$\delta z^l = [sin(y^{l-1} * *2)] * \delta x^{l-1} + [x^{l-1} * cos(y^{l-1} * *2) * 2y^{l-1}]\delta y^{l-1} \quad .$$

The exponents $l-1$ and l refer to the values before and after execution of this line. To derive the adjoint code, this can be written in matrix form as

$$\begin{pmatrix} \delta z \\ \delta y \\ \delta x \end{pmatrix}^{l} = \begin{pmatrix} 0 & x^{l-1} * cos(y^{l-1} * *2) * 2y^{l-1} & sin(y^{l-1} * *2) \\ 0 & 1 & 0 \\ 0 & 0 & 1 \end{pmatrix} \begin{pmatrix} \delta z \\ \delta y \\ \delta x \end{pmatrix}^{l-1} .$$

The corresponding adjoint equation is given by transposing the matrix

$$\begin{pmatrix} \delta^* z \\ \delta^* y \\ \delta^* x \end{pmatrix}^{l} = \begin{pmatrix} 0 & 0 & 0 \\ x^{l-1} * cos(y^{l-1} * *2) * 2y^{l-1} & 1 & 0 \\ sin(y^{l-1} * *2) & 0 & 1 \end{pmatrix} \begin{pmatrix} \delta^* z \\ \delta^* y \\ \delta^* x \end{pmatrix}^{l-1} .$$

This can be written in source code as

```
subroutine itworksccl(x,y,z,xccl,yccl,zccl)
real x,y,z,xccl,yccl,zccl
...
yccl=yccl+zccl*x*cos(y**2)*2*y
xccl= xccl+ zccl*sin(y**2)
zccl=0
...
return
end
```

The sequence of the assignments ensures that the adjoint variable zccl is not set to zero before its information is passed to xccl and yccl.

As an example of an encountered pitfall, the following assignment shall be considered:

`y(i)=y(n)` where i$\in \{1, \ldots, n\}$

The matrix form is

$$\begin{pmatrix} y(i) \\ y(1) \end{pmatrix} = \begin{pmatrix} 0 & 1 \\ 0 & 1 \end{pmatrix} \begin{pmatrix} y(i) \\ y(1) \end{pmatrix} . \tag{6.1}$$

Transposition gives

$$\begin{pmatrix} \delta^* y(1) \\ \delta^* y(i) \end{pmatrix} = \begin{pmatrix} 0 & 0 \\ 1 & 1 \end{pmatrix} \begin{pmatrix} \delta^* y(i) \\ \delta^* y(1) \end{pmatrix} .$$

Written in source code format we find

```
yccl(1)=yccl(i)+yccl(1)
yccl(1)=0
```

This is erroneous for i=1 as in this case, the forward statement is simply the identity which corresponds to no information transfer. In that case, the information content in the adjoint variable yccl(1) should not be changed either. But the derived code sets yccl(1)=0 in the last statement. The reason for this resides in the fact that in the first line of the matrix in Equation 6.1, 1 is placed on the off-diagonal entry while it should be on the main diagonal for i=1 (and in fact, we have only a 1∗1 matrix). The easiest way to eliminate this problem is to use the `i`-loop starting at 2. A correct derivation could also consist in using an auxiliary variable h and substituting the forward equation by two equations:

```
h=y(1)
y(i)=h
```

As adjoint code we obtain:

```
hccl=hccl+yccl(i)
yccl(i)=0
yccl(1)=yccl(1)+hccl
hccl=0
```

which is correct even in the case i=1. This example was chosen to illustrate how difficult it is to ensure that the derived adjoint code is correct and to show that in testing the adjoint code one has to take care to include exceptional cases as well.

6.3 Storage strategy for the AMMOC-CTM

As the adjoint integration is performed along the trajectory of the model state, the intermediate values of the forward model are needed in reverse order for the adjoint model. As a trade-off between storage space and computing time, it was decided to save the state of the model twice for every time step: after the calculation of transport and of chemistry. The intermediate model state values and auxiliary fields are recalculated in the adjoint model using parts of the forward model code. This is illustrated in Figure 6.1. In addition, the photolysis rates and the Courant numbers are calculated only during the first forward integration and read during all subsequent forward and adjoint model integrations. On today's newest supercomputers, disk storage could be substituted by main memory storage which would lead to a considerable speed-up.

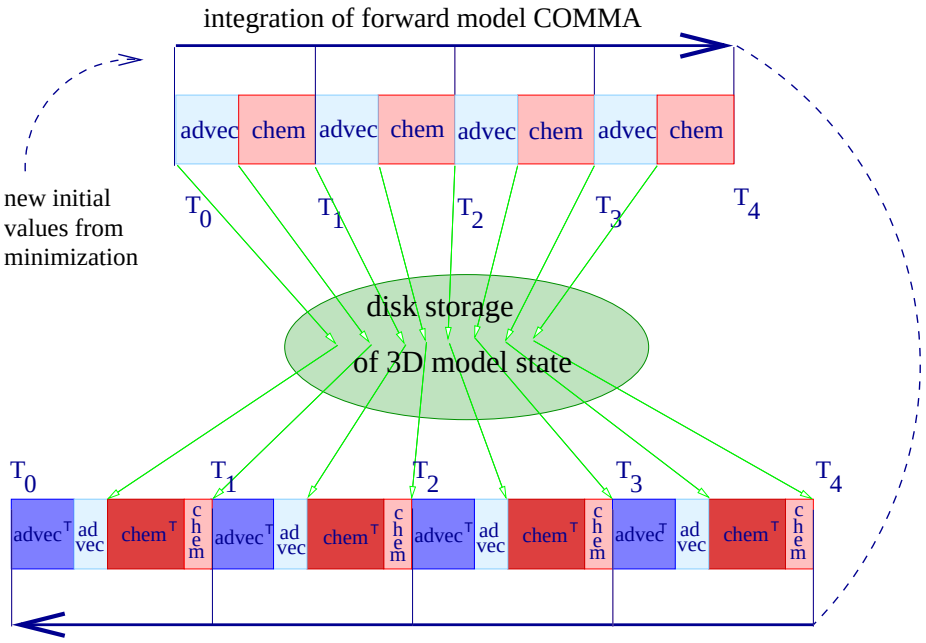

Figure 6.1: *Storage and recalculation strategy for four timesteps of one iteration of the adjoint chemistry-transport model system AMMOC-CTM. The three-dimensional model state is saved after calculation of advective and chemical changes at each timestep. The intermediate values required by the adjoint model are recalculated in the adjoint model. Light colors indicate direct model routines, bold colors indicate adjoint model routines. The values stored last are needed first.*

CHAPTER 7

Specification of a curvature penalty term in the definition of the cost function

In the standard formulation of 4D var data assimilation the cost function describes the deviation of the model from observations and the deviation of the model from the background state as discussed in Chapter 2.1. When looking at CRISTA measurements interpolated on a $2^\circ \times 2^\circ$ grid (see for example Figure 11.1), it becomes clear that the trace gas fields are smooth to a certain extent: the mixing ratio usually does not change more than a factor of two from box to box.

On the other hand, if the observation error covariance matrices are diagonal, as in the present study, a numerically unstable situation can potentially arise. If a grid box but not its neighbouring box is attributed a measurement, the adjoint mixing ratio is given by $\frac{1}{\sigma_i^2}(H_{ij}c_j - y_i^o)$, while the adjoint mixing ratio in the neighbouring box remains equal to 0. This can produce new initial mixing ratios characterised by abrupt changes if the model state c_j deviates considerably from the observation y_i^o. Furthermore, these peaks can also emerge for species which are unmeasured but chemically coupled to measured species. The peak structure can be especially pronounced if a species has a low mixing ratio.

One approach to avoid the creation of these peaks is a modification of the weighting matrices $\mathbf{R}$ and $\mathbf{B}$ in the cost function. In addition to the already described error covariances, they can be designed to imply horizontal field correlations. In this way, a measurement at one grid point is used to correct correlated grid points as well. This requires knowledge of the correlation length and strength for all species as well as knowledge of the possible dependence of the correlation on meteorological and/or chemical regimes. Further on, the use of off-diagonal elements in $\mathbf{B}$ is numerically

demanding since the required inversion of $\mathbf{B}$ leads to a largely occupied matrix and an ill-posed problem that requires preconditioning to ensure stable minimization.

Lacking knowledge about horizontal field correlations, we have followed two other approaches to obtain smoother analyses: In a first attempt, the gradient field is smoothed before minimization with the weight 4 for the central grid box and 1 for the four adjacent grid boxes. In the following, this approach is called "averaging smoothing".

In addition, a variational and hence fully consistent approach was implemented as well. It is closely related to the method presented by Wahba and Wendelberger (1980). These authors tested it by application to the height field in a meteorological model. To damp spurious oscillations introduced by the attribution of measurements to the closest grid point only, an additional forcing term was introduced in the cost function. By this term the curvature of the analysed mixing ratio field of a species at a given pressure level is controlled. We minimise

$$\tilde{J} = \frac{1}{2} \int_0^{2\pi} \int_0^{\pi} [\Delta \mathbf{c}(t_0)]^T \mathbf{A}^{-1} [\Delta \mathbf{c}(t_0)] \sin\theta d\theta d\phi \ , \tag{7.1}$$

where $\mathbf{A}^{-1}$ is an as yet undetermined weighting matrix, and $\mathbf{c}$ is the trace gas mixing ratio field. This procedure yields smoothed fields for all species in the sense that their curvature is small. For minimization, $\nabla_{\mathbf{c}(t_0)} \tilde{J}$ is needed. A small variation of $\tilde{J}$ is given by

$$\begin{aligned}
\delta\tilde{J} &= \tilde{J}\left(\mathbf{c}(t_0) + \delta\mathbf{c}(t_0)\right) - \tilde{J}\left(\mathbf{c}(t_0)\right) \\
&= \frac{1}{2} \int_0^{2\pi} \int_0^{\pi} \left[\Delta(\mathbf{c}(t_0) + \delta\mathbf{c}(t_0))\right]^T \mathbf{A}^{-1} \left[\Delta(\mathbf{c}(t_0) + \delta\mathbf{c}(t_0))\right] \sin\theta d\theta d\phi \\
&\quad -\frac{1}{2} \int_0^{2\pi} \int_0^{\pi} \left[\Delta\mathbf{c}(t_0)\right]^T \mathbf{A}^{-1} \left[\Delta\mathbf{c}(t_0)\right] \sin\theta d\theta d\phi \\
&= \frac{1}{2} \int_0^{2\pi} \int_0^{\pi} \big\{ [\Delta\mathbf{c}(t_0)]^T \mathbf{A}^{-1} [\Delta\mathbf{c}(t_0)] + 2[\Delta\mathbf{c}(t_0)]^T \mathbf{A}^{-1} [\Delta\delta\mathbf{c}(t_0)] \\
&\qquad + [\Delta\delta\mathbf{c}(t_0)]^T \mathbf{A}^{-1} [\Delta\delta\mathbf{c}(t_0)] \big\} \sin\theta d\theta d\phi \\
&\quad -\frac{1}{2} \int_0^{2\pi} \int_0^{\pi} [\Delta\mathbf{c}(t_0)]^T \mathbf{A}^{-1} [\Delta\mathbf{c}(t_0)] \sin\theta d\theta d\phi .
\end{aligned}$$

Since $\delta\mathbf{c}(t_0)$ is infinitesimal, terms of order $(\delta\mathbf{c}(t_0))^2$ can be neglected

$$\delta\tilde{J} = \frac{1}{2}\int_0^{2\pi}\int_0^{\pi} 2[\Delta\delta\mathbf{c}(t_0)]^T\mathbf{A}^{-1}[\Delta\mathbf{c}(t_0)]\sin\theta d\theta d\phi \ .$$

As we integrate over the surface of a sphere, we can apply Green's theorem

$$\begin{aligned}\frac{1}{2}\int_F\int [\Delta uv - u\Delta v]\, dF &= \int_{\partial F}\left(\frac{\partial u}{\partial n}v - u\frac{\partial v}{\partial n}\right) dS \\ &= 0 \ .\end{aligned}$$

The last equality follows as the sphere has a closed surface, i.e., $\partial F = 0$. Thus with $u = \delta\mathbf{c}(t_0)$ and $v = \Delta\mathbf{c}(t_0)$ we find

$$\delta\tilde{J} = \int_0^{2\pi}\int_0^{\pi}[\delta\mathbf{c}(t_0)]^T\mathbf{A}^{-1}[\Delta^2\mathbf{c}(t_0)]\sin\theta d\theta d\phi \ .$$

As a consequence,

$$\nabla_{\mathbf{c}(t_0)}\tilde{J} = \mathbf{A}^{-1}\Delta^2\mathbf{c}(t_0) \tag{7.2}$$

is the functional derivative of $\tilde{J}$ required for the minimization. To employ the curvature term for 4D var data assimilation, a routine was implemented that calculates the horizontal component of the Laplacian of a field. The integral of $\tilde{J}$ was replaced by a sum; $\Delta\mathbf{c}$ was calculated with respect to the adjacent grid boxes.

Smoothing of the trace gas fields is more important for the first iterations than for latter ones because the first iterations are characterised by larger corrections. Our objective is to capture the large-scale structures during the first iterations. During later iterations, when the global characteristics should be well described by the model, the necessary corrections are expected to be small and local. Therefore, we expect the above described peak problem to be less severe. In consequence, $\mathbf{A}^{-1}$ was chosen to decrease with increasing number of iterations. In this way, it is possible to approach the small-scale structures present in the measurements during the later iterations. In the end of the assimilation process, the contribution of the curvature term to the cost function should be smaller than the measurement and background contribution. Reducing the contribution of the curvature penalty term to nearly zero in later iterations makes these assimilation experiments amenable to the a posteriori analysis discussed in Chapter 12.

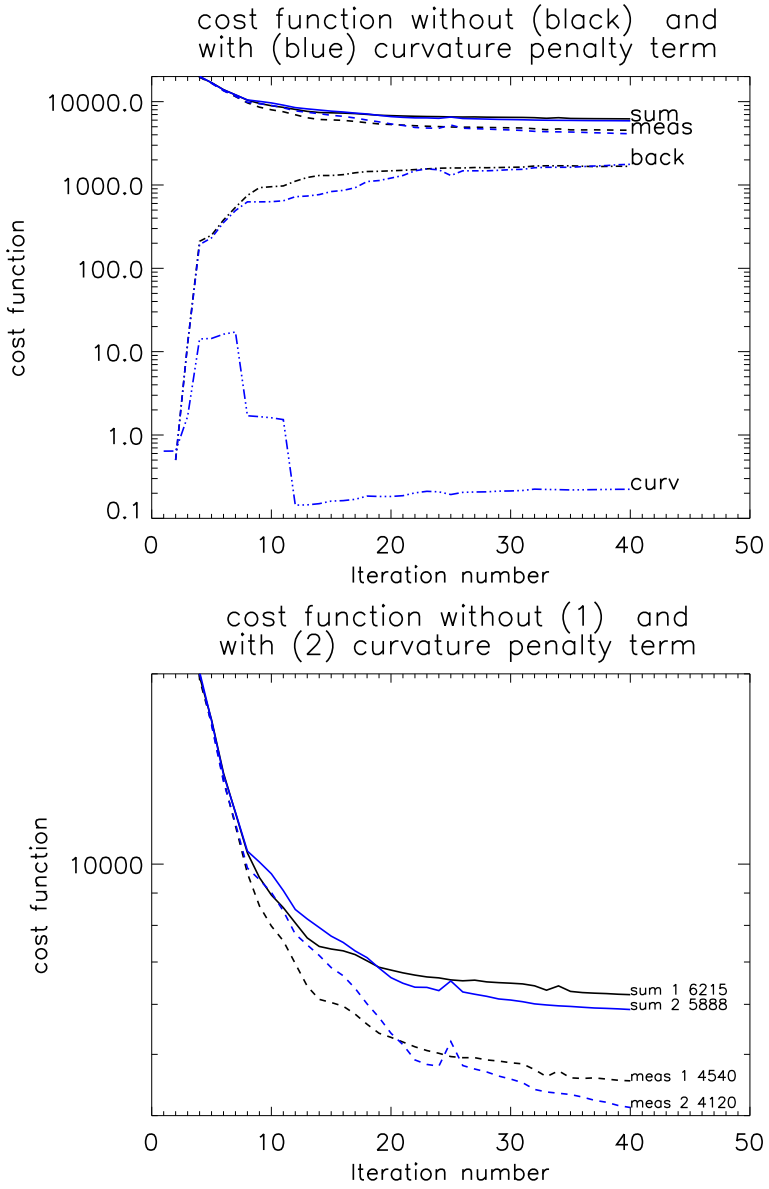

Figure 7.1: *Upper part: development of the cost function for two different smoothing techniques. 1) averaging smoothing (black line), 2) curvature penalty term smoothing (blue line). The solid lines show the sum of all forcing contributions, the dashed lines represent the measurement contributions. The dashed-dotted lines show the contributions of the background term and the dashed-triple dotted line the contributions of the curvature term. The lower figure shows the cost functions and the measurement contribution in more detail.*

As a consequence of adapting $\mathbf{A}^{-1}$ and, thus, changing the cost function, the minimization algorithm has to start anew collecting information about the new Hessian matrix. The restart of the minimization algorithm possibly leads to an increased number of iterations. Figure 7.1 displays the cost function development for Nov. 4-5, 10.9 hPa, calculated with the averaging smoothing and the curvature penalty smoothing for comparison. Both experiments start with the same cost in the first iteration. The weight for the curvature contribution was reduced in iterations 8 and 12 as can be seen by the abrupt change in the cost function. In these iterations, due to the changed cost function, the L-BFGS had to start approximating the Hessian matrix anew. This reduced performance (i.e. smaller reduction of the cost function) is visible in iterations 9/10 and 13/14 in the enlarged plot, but this is negligible compared to the overall better performance of the curvature penalty smoothing. The reduced cost is due to a closer correspondence of the model with measurements.

Finally, it should be added that the curvature term is zero not only for a constant function, but also for a linear function. This solution is not permitted in zonal direction because the latitudes are "closed". In meridional direction it is permitted since the curvature is not calculated for the polar and their adjacent boxes because of the specific grid structure at the poles. Hence, with respect to the curvature penalty term the polar boxes act like the free ends of a rope.

7.1 Curvature penalty term in comparison to background error correlations

The main incentive for the implementation of the curvature penalty term in the cost function was the observation that the analyses at the end of the assimilation period were less smooth than the measurements interpolated on a $2^\circ \times 2^\circ$ grid. As these analyses are used as first guess and background for the following assimilation period, a potentially unstable and undesired situation could arise. As a remedy, we implemented the curvature penalty term in the cost function. Its effect can be illustrated by the following toy model. It consists of 10 grid points with periodic boundary conditions. Neglecting the temporal aspect, the cost function can be minimised directly by setting $\nabla J = 0$. Solving for $\mathbf{c}$, one obtains

$$\mathbf{c} = [\mathbf{B}^{-1} + \mathbf{H}^T\mathbf{R}^{-1}\mathbf{H}]^{-1}[\mathbf{B}^{-1}\mathbf{c}^b + \mathbf{H}^T\mathbf{R}^{-1}\mathbf{y}^o] \ .$$

Including the curvature penalty term and setting $\alpha := \mathbf{A}^{-1}$ and $\mathbf{Dc} := \Delta\mathbf{c}$, the solution is

$$\mathbf{c} = [\alpha\mathbf{D}^2 + \mathbf{B}^{-1} + \mathbf{H}^T\mathbf{R}^{-1}\mathbf{H}]^{-1}[\mathbf{B}^{-1}\mathbf{c}^b + \mathbf{H}^T\mathbf{R}^{-1}\mathbf{y}^o] \ .$$

The background field was chosen to oscillate between 5 and 7. The weight α for the curvature penalty term was chosen to be large (0.3) to clearly illustrate its effect. It reduces the oscillation of the analysis as compared to the background field as can be seen in Figure 7.2. When adding a measurement at grid point 5 which is far away from the background, the analysis is corrected toward the measurement at the place of measurement as well as the neighbouring grid points.

We now examine the case where the oscillation of the background originates in instabilities of former analysis procedures. To this end, we take the measurement to be the average background value (Figure 7.4). In this case, the analysis at grid point 5 is corrected toward the measurement while the neighbouring grid boxes are a little drawn away from the measurement, but this effect is much smaller than the smoothing effect so that overall, the analysis is closer to the measurement, which we assumed to be representative, than the first guess.

Another method often suggested to smooth the analysis is the use of off-diagonal elements in the background error covariance matrix. However, we consider this approach less suitable for our problem because it only leads to a considerably smoothed field if the fluctuations in the background field are smaller than the deviations between background and measurements (Figure 7.3). In the present example, as discussed above, we assumed that this condition is violated. Using a background error covariance matrix with variance 1 and covariance 0.45 between neighbouring grid points, the grid boxes adjacent to the measurement location are corrected in the same direction as the measurement grid box and therefore away from the measurement (Figure 7.5).

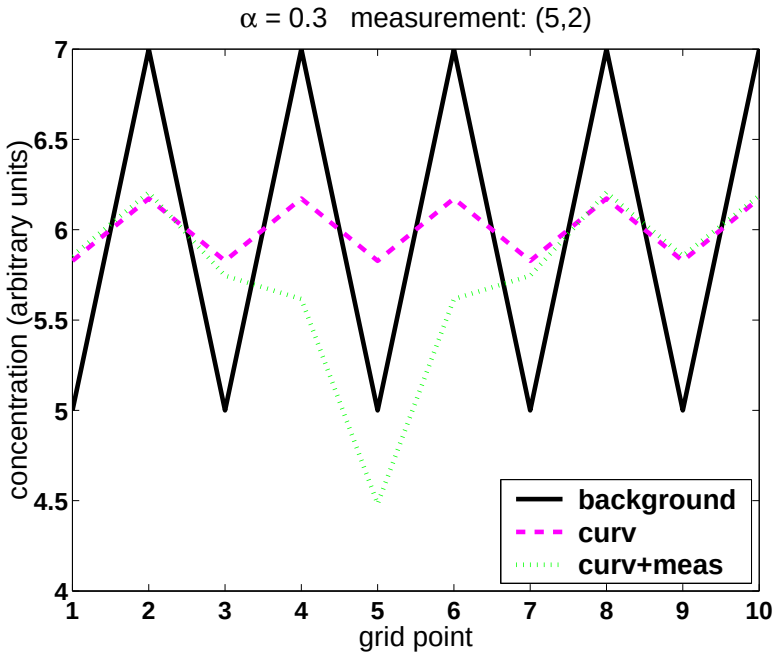

Figure 7.2: **Toy model smoothing by curvature penalty term.** *Measurement (5,2) is an outlier. Solid black line: background; dashed red line: result of curvature term; dashed-dotted green line: result of curvature term plus measurement.*

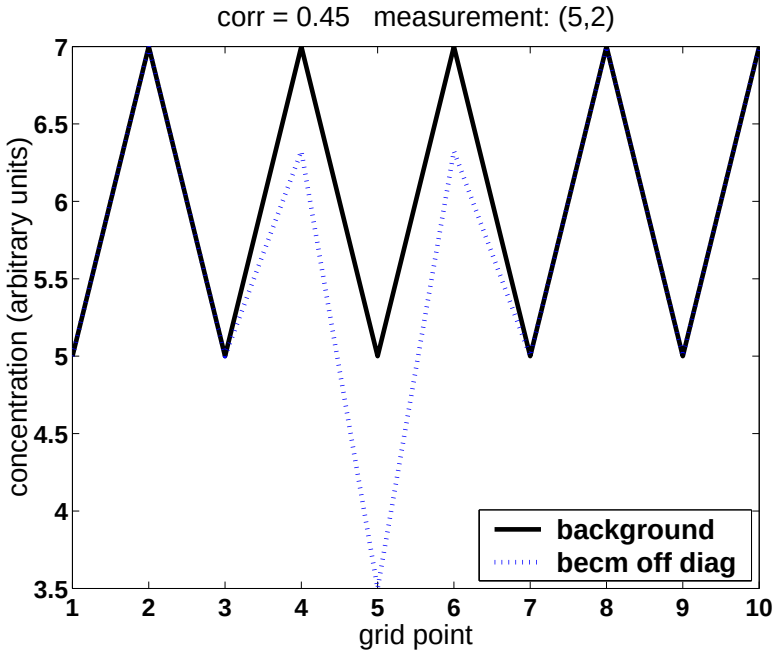

Figure 7.3: **Toy model smoothing by background covariance.** *Measurement (5,2) is an outlier. Solid black line: background; dotted blue line: result of background error covariance matrix containing off-diagonal entries.*

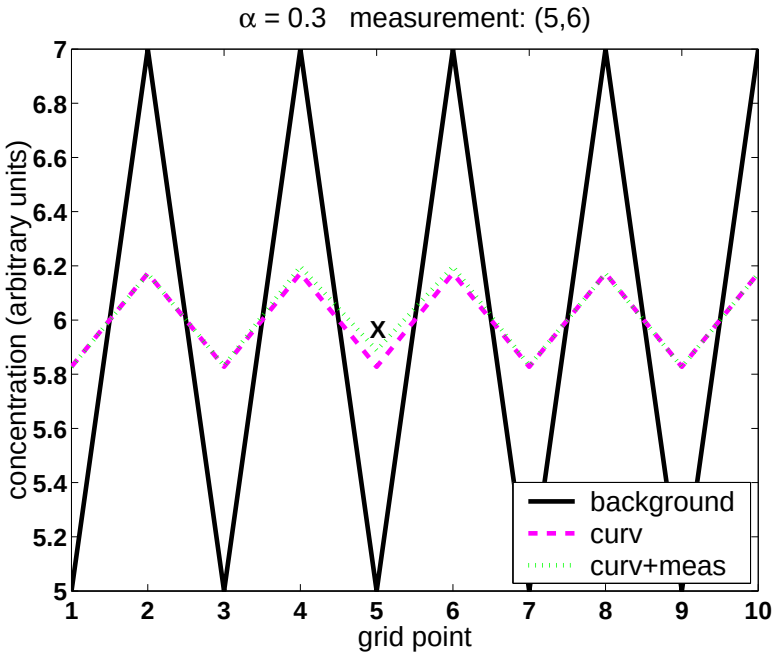

Figure 7.4: **Toy model smoothing by curvature penalty term.** *Measurement (5,6) equals the average of the background. Solid black line: background; dashed red line: result of curvature term; dashed-dotted green line: result of curvature term plus measurement.*

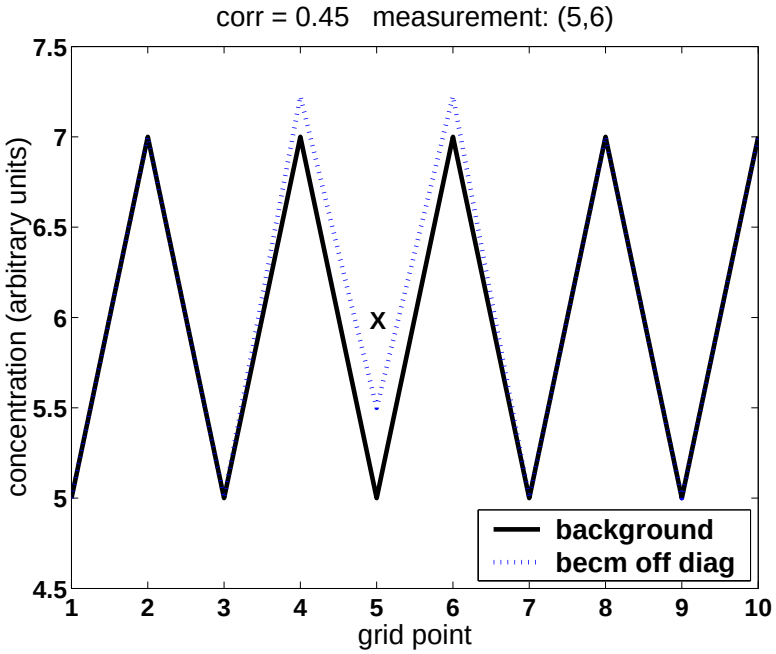

Figure 7.5: **Toy model smoothing by background covariance.** *Measurement (5,6) equals the average of the background. Solid black line: background; dotted blue line: result of background error covariance matrix containing off-diagonal entries.*

CHAPTER 8

Minimization

8.1 The L-BFGS minimization algorithm

We assume that the employed first guess is sufficiently close to the minimum and that the cost function is smooth in a sufficiently large area around the minimum so that the cost function can be approximated by a quadratic function in the region encompassing the first guess state and the minimum. These assumptions seem to be justified since the model is free of phase transitions or any other discontinuous physical processes. For the 3D var case which is obtained from Equation 2.3 for the case n=0, the cost function is quadratic and the Hessian matrix $\mathbf{B}^{-1} + \mathbf{H}^T\mathbf{R}^{-1}\mathbf{H}$ is positive definite. Thus, the state which solves $\nabla J = 0$ is a minimum. The employed L-BFGS (**l**imited memory **B**royden, **F**letcher, **G**oldfarb, **Sh**anno) minimization algorithm (Nocedal, 1980; Liu and Nocedal, 1989) constitutes a quasi-Newton method which is devised to minimize a function by determining the zero of its gradient. As the minimum of the cost function can be found at the zero of the corresponding gradient, the problem can be solved by a Newton method if the function is sufficiently smooth. For a quadratic function h, the classical Newton method described by the following iteration rule determines the zero of the gradient in one iteration:

$$\mathbf{x}_k \rightarrow \mathbf{x}_{k+1} = \mathbf{x}_k - \mathbf{H}^{-1}\left(\mathbf{x}_k\right)\mathbf{g}\left(\mathbf{x}_k\right) \ ,$$

where $\mathbf{H}$ denotes the Hessian matrix and $\mathbf{g}$ the gradient. For other functions which can be approximated locally by quadratic functions several iterations are necessary, provided that $\mathbf{x}_0$ is sufficiently close to the minimum. As the determination of the inverse of the Hessian matrix is numerically demanding, the quasi-Newton methods take approximations of $\mathbf{H}_k := \mathbf{H}^{-1}\left(\mathbf{x}_k\right)$ instead

(Stoer, 1994). The disadvantage lies in the loss of quadratic convergence of the algorithm which is inherent in the Newton method. The BFGS minimization algorithm is a quasi-Newton method of the Oren-Luenberger class which can be described as follows:

- choose a starting vector $\mathbf{x}_0 \in \Re^n$ and a positive definite matrix $\mathbf{H}_0 \in \Re^{n \times n}$ and set $\mathbf{g}_0 = \mathbf{g}(x_0)$

For k =0,1,... do

- if $\mathbf{g}_k = 0$ finish: $\mathbf{x}_k$ is stationary point of h
- calculate the new search direction $\mathbf{s}_k := \mathbf{H}_k \mathbf{g}_k$
- set the new vector $\mathbf{x}_{k+1} = \mathbf{x}_k - \lambda_k \mathbf{s}_k$ by (approximately) minimizing $h(\mathbf{x}_{k+1}) \approx \min\{h(\mathbf{x}_k - \lambda_k \mathbf{s}_k) \mid \lambda \geq 0\}$ and set $\mathbf{g}_{k+1} := \mathbf{g}(\mathbf{x}_{k+1})$, $\mathbf{p}_k := \mathbf{x}_{k+1} - \mathbf{x}_k$, $\mathbf{q}_k := \mathbf{g}_{k+1} - \mathbf{g}_k$
- calculate the new approximation to the Hessian matrix

$$\mathbf{H}_{k+1} = \mathbf{H}_k + \left(1 + \frac{\mathbf{q}_k^T \mathbf{H}_k \mathbf{q}_k}{\mathbf{p}_k^T \mathbf{q}_k}\right) \frac{\mathbf{p}_k \mathbf{p}_k^T}{\mathbf{p}_k^T \mathbf{q}_k} - \frac{1}{\mathbf{p}_k^T \mathbf{q}_k} \left(\mathbf{p}_k \mathbf{q}_k^T \mathbf{H}_k + \mathbf{H}_k \mathbf{q}_k \mathbf{p}_k^T\right) .$$

After proposing the new vector $\mathbf{x}_{k+1}$, the minimization routine returns control to the main program to calculate $h(\mathbf{x}_{k+1})$. During the next call to the minimization, it is checked whether $\mathbf{x}_{k+1}$ and $h(\mathbf{x}_{k+1})$ fulfill the two criteria

- decrease condition: $h(\mathbf{x}_k - \lambda_k \mathbf{s}_k) \leq h(\mathbf{x}_k) - \epsilon \lambda \mathbf{g}(\mathbf{x}_k) \mathbf{s}_k$
- curvature condition: $|\mathbf{g}(\mathbf{x}_k - \lambda_k \mathbf{s}_k) \mathbf{s}_k| \leq \epsilon^{'} |\mathbf{g}(\mathbf{x}_k) \mathbf{s}_k|$

where $0 < \epsilon, \epsilon^{'} < 1$.

Communication between the routines was enhanced so that only the accepted $\mathbf{x}_{k+1}$ and $\mathbf{g}_{k+1}$ are stored on hard disk. This is necessary because h is not exactly quadratic and the minimization algorithm therefore sometimes proposes a new first guess which is not accepted due to the above criteria. In this way, it is ensured that only the accepted $\mathbf{x}_{k+1}$ and $\mathbf{g}_{k+1}$ are stored on hard disk. Under certain conditions, the algorithm can show even superlinear convergence.

In the L-BFGS version storage space is saved by a different treatment of $\mathbf{H}_{k+1}$ with separate storage of the newly obtained information from each iteration. This is done in the form of two vectors at a time, which are of the dimension of the model state to be determined. Thus, storage space and computing time for the inverse of the Hessian matrix are reduced. The L-BFGS algorithm was found to be one of the most efficient when the dimensions of the control variables are greater than 10^5 (Zhang et al., 2000) and to exhibit a good convergence rate (Zou et al., 1993).

8.2 Preconditioning

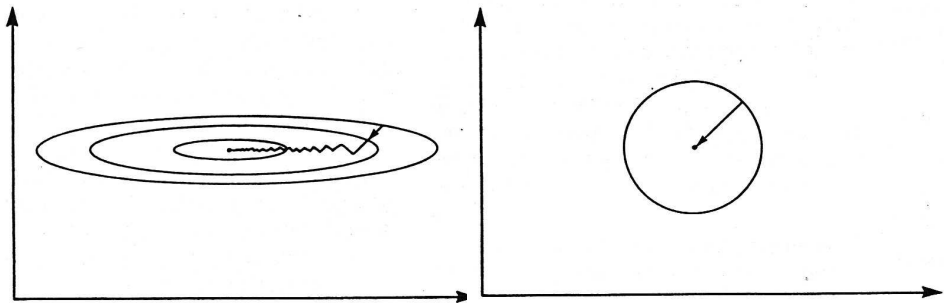

Figure 8.1: *Examples of cost function isopleths. The right picture shows a circle where the gradient is directed towards the minimum. The left picture shows the less favorable case of ellipsoidal isopleths where the local gradient is not directed towards the minimum. From Chao and Chang (1992).*

The visualization of the shape of isopleths of the cost function in control variable space in Figure 8.1 illustrates a difficulty for the minimization procedure: if the isopleths are elongated ellipsoids instead of circles, the gradient does not point into the direction of the global minimum. The ellipticity is measured by the condition number of the corresponding Hessian matrix (ratio between the largest and the smallest eigenvalue). The idea of preconditioning is to change the space of control variables to decrease the condition number and to retransform to the original space after minimization. As the best preconditioning depends on the final configuration of the assimilation system, a rather simple preconditioning has been implemented so far: prior to the minimization, the state variables are divided by their first guess value to obtain data of the order of magnitude 1. Accordingly, the gradient of the cost function is multiplied with the same value. After the minimization, the new initial concentrations are retransformed by multiplication with the first guess value. As in every iteration the same fields are used for preconditioning, consistency is given.

8.3 Changes to the L-BFGS minimization routine

Communication between the L-BFGS minimization routine and other routines was increased as already mentioned in Section 8.1 to allow for changes in the definition of the cost function between iterations.

Another weakness of the original routine was the fact that only the L-BFGS routine had information about which and how many new initial values it accepted. Therefore, they had to either be handled inside the L-BFGS routine or to be stored to disk for every iteration. In the latter case,

after completion of all iterations, it had to be decided with the help of the standard output which was the last accepted model state and to discard the others. As handling the output of the data inside L-BFGS did not seem wise, communication was enhanced so that after completion of L-BFGS it could be decided whether to store the iteration's model state to disk.

CHAPTER 9

Configuration of the AMMOC-CTM system

At the center of the AMMOC-CTM system one finds the COMMA-CTM described in chapter 5. It is named 'forward model'. Its counterpart which requires more computing time is the adjoint code, called 'backward model'. The chemistry module and its adjoint were kindly provided by J. Schwinger and A. Klyuchnikova. The system is completed by the L-BFGS minimization routine. These three are called iteratively in this order until the cost

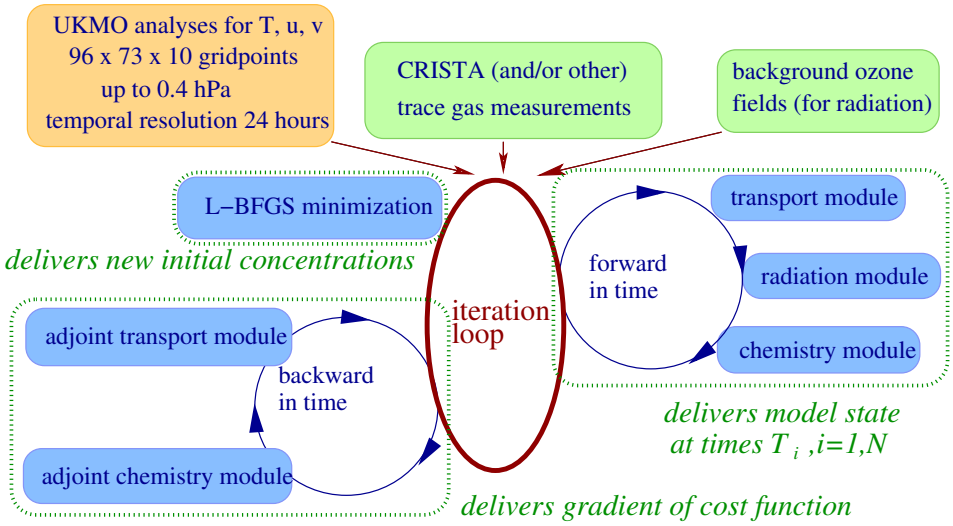

Figure 9.1: *Model configuration of the adjoint chemistry-transport model system. For one iteration, an integration of the direct model has to be carried out (forward in time) followed by an integration of the adjoint model (backward in time) before a call to the minimization routine.*

function reaches its minimum or the iteration count reaches a given maximum. Minimization is performed for 28 species, excluding long-lived CFCs which do not interact significantly on the timescale of 24 hours, and short-lived species such as O^1D which are determined by the equilibrium with other species instead of their initial values. The species considered in the minimization procedure are the same that are considered as background knowledge in real case experiments. They are listed in Table 9.1.

The minimization routine first checks whether the initial values it previously suggested should be accepted (only if it is not the first iteration) and it calculates new initial values. The new initial values are then used for the next iteration. Photolysis rates calculated in the radiation module are not subject to optimization and therefore do not possess an adjoint counterpart. The contribution of the curvature penalty term to the cost function and its gradient is calculated after the backward model. A list of all routines and their task is given in appendix B.

N_2O	BrCl	$BrONO_2$	N_2O_5	Cl_2O_2	HNO_4
CH_4	HNO_3	H_2	H_2O_2	HBr	Cl_2
$ClONO_2$	HOBr	HOCl	HCl	OClO	NO_3
H_2O	Cl	NO_2	BrO	O_3	HO_2
Br	NO	ClO	OH		

Table 9.1: *Species included in the minimization procedure.*

CHAPTER 10

Identical Twin Experiments

Identical twin experiments constitute an opportunity to test the capability and limits of the assimilation model system. The insight gained is useful for the interpretation of the real case experiments described in Chapter 11. To this end, an integration of the chemistry-transport model is performed to obtain artificial "measurements": selected elements of the state vector of the system. This model integration is called "reference run". The assimilation system is then employed with different initial concentrations called "first guess" and a subset of the state vector of the reference run is used in the place of real measurements in the assimilation system. In this way, it can be examined to which extent the assimilation system is able to reproduce the reference run. Besides testing the correct setup of the assimilation system, the choice of selected observations in time, geographical location and in the space of chemical species concentrations allows one to test the capability of the system to estimate the "truth" also for unobserved elements of the state vector. In contrast to real case experiments, model errors due to the inaptitude of the model to represent reality can be excluded because the "truth" is constructed by the model. This implies that representativity does not pose a problem. If desired, random errors could be added to the calculated observations.

10.1 Configuration of the Identical Twin Experiments

In this section, the set-up of the identical twin model configuration is described. The assimilation period is limited to 24 hours. Fisher and Lary (1995) came to the conclusion that the tangent linear equation is valid over

a 48-hour period for finite variations in at least some important directions in phase space. Our choice of 24 hours is motivated by the fact that CRISTA obtained a near-global coverage in 24 hours, thus the 24 hour assimilation period leads to an update of the whole domain measured by CRISTA. When choosing the length of the assimilation period, one has to consider that it should be shorter than the range of atmospheric predictability and should be long enough to allow for a temporal development in order to take advantage of the four-dimensional nature of the technique.

One issue in identical twin experiments is the specification of error covariance matrices. As the first guess is purposely chosen different from the truth, the use of a background term in the cost function would force the analysis towards the first guess and thus away from the "measurements". On the other hand, the system can be underdetermined without background error covariance matrices. In the identical twin experiments presented here, we chose not to specify any background term in the cost function with a view to test whether the system is capable of finding the minimum of the cost function. As a consequence, the setup of the identical twin experiments cannot be analysed a posteriori with the methods discussed in Chapter 12. However, if the problem is underdetermined or at most a one-to-one problem and all observations are taken from the same reference run, it is in principle possible that the system reproduces the initial state of the reference run. The measurement error was chosen as 10% of the first guess of the respective species in a given grid box, with a minimum of 0.01 ppb.

10.2 Identical Twin Box Experiments

A sequence of experiments referred to as BOX was set up to investigate the properties of the chemical part of the assimilation system. In particular, we wanted to inquire in how far information about the species measured by CRISTA is suited to determine the mixing ratio of unmeasured species. We therefore ignore transport in this case. This implies that there is no coupling between different grid points. The only relationship between the boxes is given during the minimization procedure where the L-BFGS minimization algorithm chooses one step size for the state vector describing all grid boxes.

Interest in the chemical transformation part in a 2D context stems from the different chemical regimes in different regions of the world. The most apparent reason for the differences is the length of the day. In the period chosen for investigation in November, the polar night region extended from 72.5°N to the pole.

For the assimilation experiments BOX1 and BOX2, the forward model was run for four 24h periods to approach chemical equilibrium in all grid boxes. The model state at the end of this pre-run was used as first guess for the assimilation system. Then, the volume mixing ratios were multi-

experiment	**BOX1**
date	Nov. 6, 1994 (for radiation)
altitude	10.9 hPa
temperature	taken from UKMO analyses
assimilation period	24 hours, 12 UTC – 12 UTC
observation time	14 UTC and 02 UTC
observations employed for 28 species	N_2O, BrCl, $BrONO_2$, N_2O_5, Cl_2O_2, HNO_4, CH_4, HNO_3, H_2, H_2O_2, HBr, Cl_2, $ClONO_2$, HOBr, HOCl, HCl, OClO, NO_3, H_2O, Cl, NO_2, BrO, O_3, HO_2, Br, NO, ClO, OH
observation locations	all grid boxes
Pre-run	4 days chemistry with photolysis rates for Nov. 6
IT-distortion	factor 2 for reference run
iterations	60
experiment	**BOX2**
setup	as for experiment BOX1 except:
observations employed for 5 species	N_2O, CH_4, HNO_3, $ClONO_2$, O_3 “CRISTA-species”

Table 10.1: *Setup of the assimilation experiments BOX1 and BOX2.*

plied by 2 to give the initial values of the 24 hour reference run. Due to the nonlinearity of the chemical reactions, this reference run describes the relaxation of the model towards a new chemical equilibrium. The mixing ratios of 28 species listed in Table 10.1 at 14 UTC and 2 UTC produced by a reference run were considered to be observed for experiment BOX1. The chosen species are identical to those considered in the minimization process. (See Chapter 9 for a discussion of the selection.) The choice of 28 observed species out of 41 model species allows one to investigate whether the observed species are corrected. For experiment BOX2 only those 5 species measured by CRISTA, which are used for the real case experiments in Chapter 11 and are called CRISTA species in the following, were used as observations. The forward model of the assimilation system was then started with the equilibrium model state as described above to assimilate the data generated by the reference run.

The performance of the experiments is summarised in Figures 10.1 and 10.2 showing the evolution of the cost functions. The cost functions seem not to have saturated yet. Nevertheless, the reduction from $1.4{\cdot}10^7$ to $1.5{\cdot}10^4$ is significant. This is reflected by the close correspondence of analysis and measurements in many grid boxes and by small values of the gradient for extended regions.

The polar night region north of 72.5°N is of special interest. Being deprived of sunlight for extended periods the polar night region is charac-

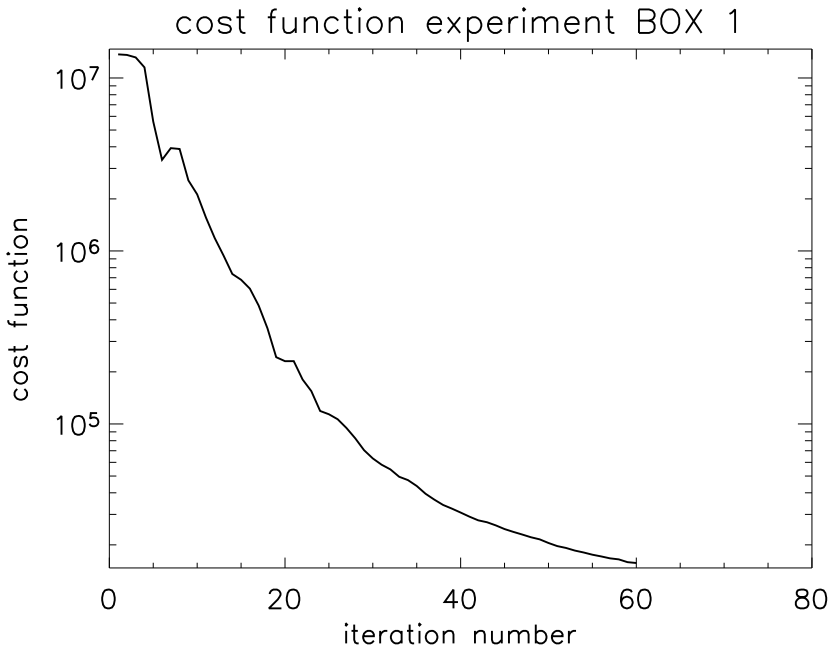

Figure 10.1: *Cost function for assimilation experiment BOX1. From the reference run, 381 808 elements were used as observations.*

terised by the absence of any photolysis reactions and thus by a different chemical regime than lower latitudes and the summer pole. It is interesting to examine the polar night region in the identical twin box experiments to investigate whether the trace gas distribution is corrected in the absence of photochemical reactions. The polar night region is clearly visible in the gradient field of the cost function with respect to NO_3 at 10.9 hPa for the last iteration of experiment BOX1 (Figure 10.3). This gradient is larger than in most sunlit areas. The same is true for NO_2. The visible wave one structure in the polar night area stems from the employed UKMO temperature field shown in Figure 10.4. It is already present in the concentration field after the spin-up time (Figure 10.5). The large gradient implies that the model has not been able to correct these species as can also be seen in the temporal evolution of the trace gas concentrations for the grid box displayed in Figure 10.7. The applied errors for NO_2 and NO_3 are large compared to their mixing ratios. Nevertheless, as only reference run values are used as information, and as the system is therefore underdetermined, the model would be expected to correct these species. In contrast, in the presence of photochemical reactions, the model is able to correct NO_2 and NO_3 concentrations, even if these species are not observed like in assimila-

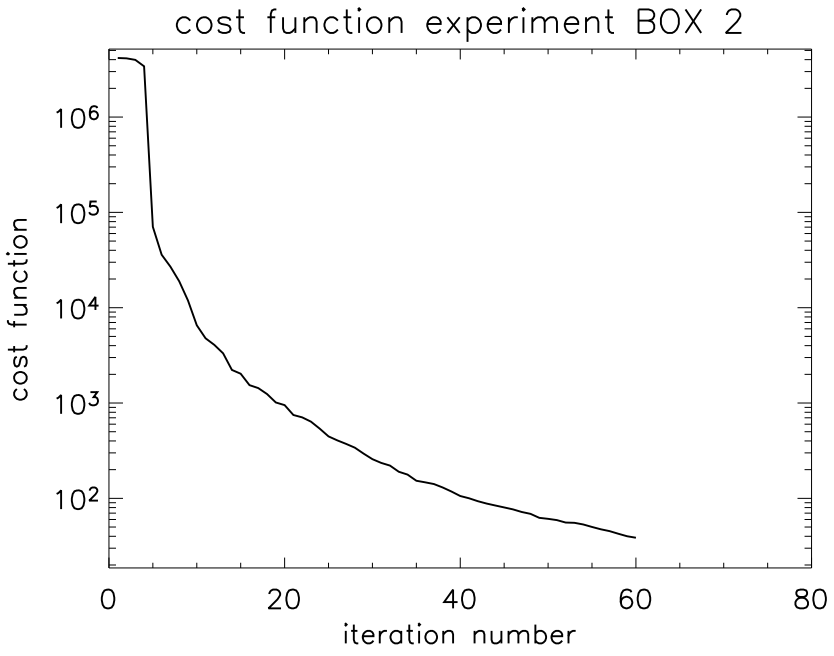

Figure 10.2: *Cost function for assimilation experiments BOX2. From the reference run, 68 180 elements were used as observations.*

tion experiment BOX2 and even though their mixing ratio may be small at initial time. The results for one grid box at 0°N, 0°E is shown in Figure 10.8. Here, the largest values of the mixing ratio are of the order of the smallest employed errors.

The dependence of the chemical coupling of NO_3 to CRISTA species on the presence of photolysis reactions is visible in the horizontal gradient field of the cost function with respect to NO_3 for the last iteration of experiment BOX2 (Figure 10.6). This horizontal gradient field is different from zero only in the sunlit areas. This shows that in the polar night area one cannot expect NO_3 to be corrected on the basis of information taken from the CRISTA species.

These findings are relevant with respect to the real case experiments presented in Chapter 11. Even though the region north of 67°N was not observed by CRISTA during the first flight, parts of the polar night region are related to the observed region through transport. Therefore, a difficulty to correct the model state towards CRISTA observations might arise if the information due to an observation of a nitrate species is distributed through chemical coupling to the adjoint variables of NO_2 or NO_3 and then transported into the polar night area. There, as discussed above, these species

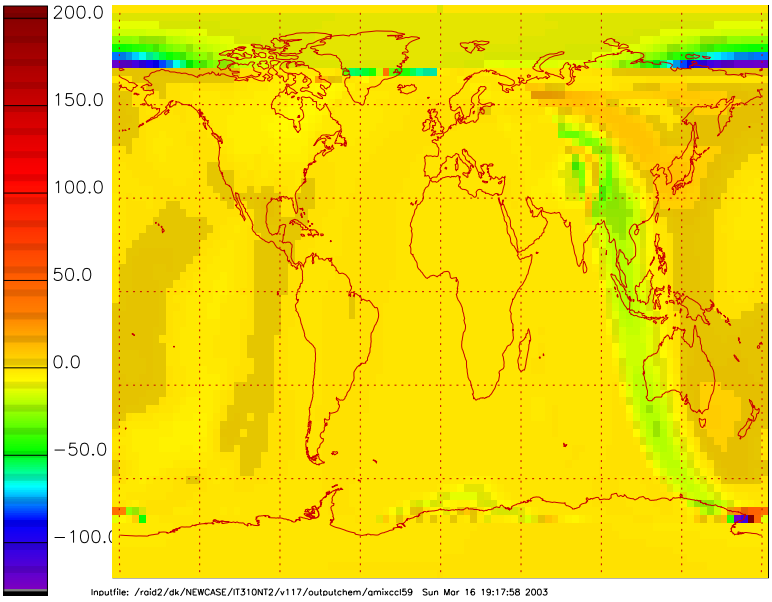

Figure 10.3: *Gradient [ppb^{-1}] of the cost function (Equation 2.7) with respect to NO_3 at 10.9 hPa on Nov. 6, 12 UTC for experiment BOX1.*

are not properly corrected and in consequence, the observation cannot be reproduced.

The result for HNO_4 in the experiment BOX2 (Figure 10.8) shows a distinctly larger deviation between reference run and analysis at the beginning of the assimilation interval than at the end. This effect might be due to the relaxation of the system towards chemical equilibrium. In addition, Fisher and Lary (1995) found that a good analysis at initial time is not mandatory for subsequent times due to transient effects of chemical disequilibrium. Therefore, the end of the assimilation interval was chosen for analysing the agreement. We compared the deviation of the analysis from the reference state to the deviation of the first guess from the reference state. In Figures 10.10 to 10.17, this relative error is displayed in percent for those species with a concentration larger than 10^{-14} ppb and whose error is smaller than 100% for the two experiments BOX1 and BOX2 and for different photochemical regimes. Further on, CFCs are ignored due to the employed concentration threshold. No improvement is expected for them since they interact only very weakly during the assimilation period. To ensure a sound statistical basis, averaging over several longitudes was performed. Figures 10.10 and 10.14 display the results for the latitudinal circle 80°S for experiments BOX1 and BOX2, respectively. For experiment BOX1, the analysis of most species, for which observations were provided to the assimilation system, was significantly improved. Only slight improvements are visible for HOBr, OClO,

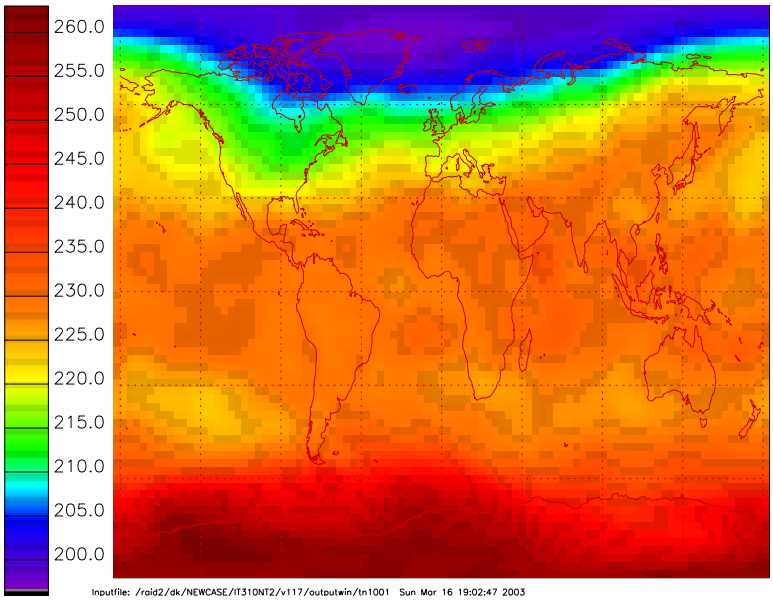

Figure 10.4: *UKMO temperature [K] at 10.9 hPa on Nov. 6, 12 UTC employed for the spin-up phase of assimilation experiments BOX.*

BrCl and $BrONO_2$. Even though HBr, BrO and Br were observed, their concentration was not improved. The species H, O^3P and O^1D were unobserved but improved due to chemical coupling to observed species. Their relative error was reduced to less than 0.34%. The mixing ratio of these short-lived species is determined by the concentration of longer-lived species which were observed. In the case of providing the reference run values of the CRISTA species to the assimilation system, only slight improvements were detectable for OClO, BrCl, $BrONO_2$. No correction was obtained for H_2, HBr, HOBr, BrO, Br and NO. The poor performance of the bromine species is plausible since no bromine species was considered to be observed. Among the CRISTA species, $ClONO_2$ shows the largest error with a value of 4.9%. Overall, this shows that the observation of the 5 CRISTA species suffices to correct a large number of other species, but the analysis improves upon observing more species as in the case of BOX1. In consequence, by assimilating CRISTA data we can expect to correct several of the model species, but we do not await improvement for bromine species and have to deal carefully with NO.

The assimilation results for the polar night area, where the latitudinal circle at 72.5°N was chosen for the calculation of the relative error, were the least satisfying of both experiments. They are displayed in Figures 10.11 and 10.15. In the case of BOX1, only few of the observed species were significantly corrected. One reason for this effect is that the errors

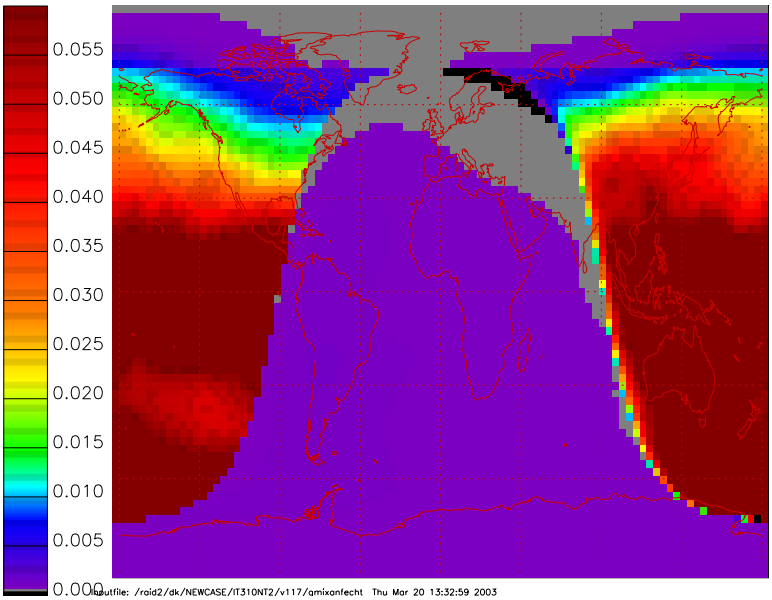

Figure 10.5: *NO_3 [ppb] first guess field for assimilation experiment BOX1 after spin-up period. Plot range limited to display the wave one structure at the polar night edge. Actual maximum is 0.31 ppb.*

for species with low mixing ratios were assumed to be rather large due to the employed threshold of a minimum error of 0.01 ppb. The analysis fits the provided measurements within the assumed errors. Nevertheless, as the model is only constrained by observations and no background information is employed, the polar night area again seems to be difficult for assimilation. In addition to the observed species only HO_2 is significantly improved in the case of BOX2. In the real case experiment we therefore do not expect to obtain corrections of unmeasured species in the polar night area.

The relative error at equatorial latitudes was calculated for two different longitudinal areas to distinguish whether the beginning and end of the assimilation period were daytime or nighttime. Longitudes 0–71.25°W (Figures 10.12 and 10.16) are sunlit at 00 UTC, while longitudes 150°W–138.75°E (Figures 10.13 and 10.17) are in darkness at 00 UTC. This is of relevance for the quality of the assimilation result: for example in BOX2 in latitude band 0–71.25°W, a good analysis was obtained for NO_2 while in latitude band 150°W–138.75°E no significant improvement was obtained for this species. In comparison, Figures 10.9 and 10.8 show the temporal evolution of trace gas concentration at 150°W, 0°N and 0°N, 0°E, especially the too large increase of NO_2 in Figure 10.9. In the case of experiment BOX1, the assimilation results of these two latitude bands differ especially for BrCl and BrO. Thus, in real case experiments with CRISTA data we cannot expect

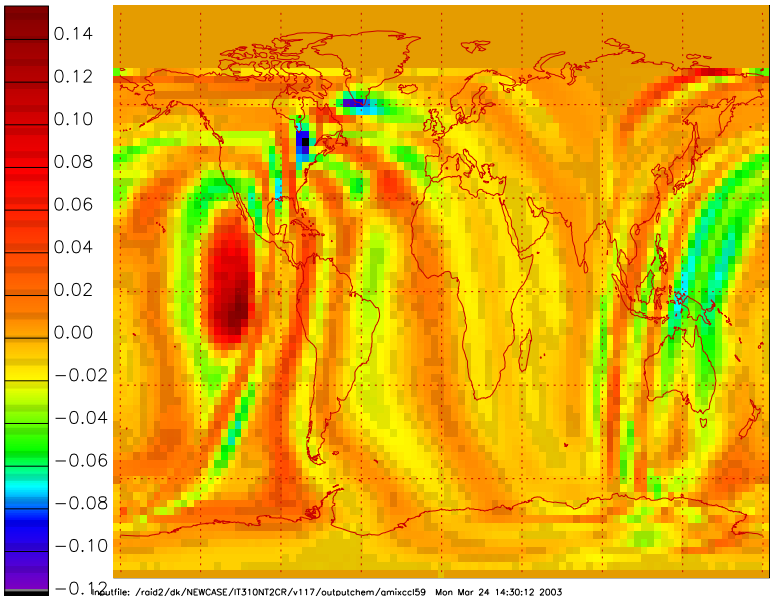

Figure 10.6: *Gradient [ppb^{-1}] of the cost function (Equation 2.7) with respect to NO_3 at 10.9 hPa on Nov. 6, 12 UTC for assimilation experiment BOX2.*

the analysis of NO_2 to be of equal quality under all conditions.

Another area of special interest constitute those grid boxes where the first measurement in the assimilation interval is supplied at sunrise and where the day is very short (grid box 81,65; 60°W, 70°N) or the night is very short (grid box 46,8; 168.75°E, 72.5°S). These grid boxes are characterised by the largest values in the gradient of the cost function for NO_3 (Figure 10.3) as well as for NO_2 and ozone in the case of experiment BOX1. The temporal evolution of selected trace gas concentrations and corresponding gradients in this grid box are displayed in Figures 10.18 and 10.19. This leads to the conclusion that the model has difficulties to exploit measurements taken at an instance of rapid change.

10.2.1 Discussion

In summary, the set-up of the model system has been tested by identical twin experiments. The cost function was reduced by several orders of magnitude in the course of 60 iterations. As the reduction during the last 20 iterations was comparably small, we considered 40 iterations to be sufficient for the real case experiments, especially for later days of the assimilation period where the first guess can be assumed to be closer to the truth than here, where the first guess was purposely chosen different from the reference run considered

to be the truth. The results indicated that observations provided at two times determine the trace gas mixing ratios during the whole assimilation interval.

Assimilation was most successful for the polar day in the southern hemisphere. There, the state of most of the species was improved by the assimilation. In particular, supplying information about the CRISTA species at two times reduced the relative error of the mixing ratio at the end of the 24 hour assimilation period to less than 4.8%. Further on, many unobserved species were significantly corrected. They included O^1D, O^3P which were practically error-free as well as NO_3, HNO_4, Cl_2, HCl, N_2O_5, Cl, H, OH, NO_2, HO_2, H_2O_2, ClO, HOCl, H_2O and Cl_2O_2. Large errors were still present for the bromine species and OClO.

In the polar night area, besides the observed species, only HO_2, NO_3 and HOCl were considerably corrected.

NO_3 and HOCl are the only non-CRISTA species that are significantly corrected in all four areas, NO_3 even better than HOCl. HNO_4 is corrected to errors less than 30 % outside the polar night area.

If the end of the assimilation interval is during daytime, the following species are significantly corrected to show errors between 20% and 50 %: Cl_2O_2, H_2O_2, ClO, OH, NO_2 and Cl.

For the assimilation of CRISTA data outside the polar night area we therefore expect to obtain good analyses of the observed species as well as for NO_3 and HNO_4 and during the day for the short-lived O^1D and O_3 as their average error was less than 20% in the identical twin experiments. Significantly improved analyses are expected for many other species, including N_2O_5, H_2O_2, HOCl, H_2O, Cl, HO_2, ClO, OH and H. Only slight improvement is expected for the bromine species.

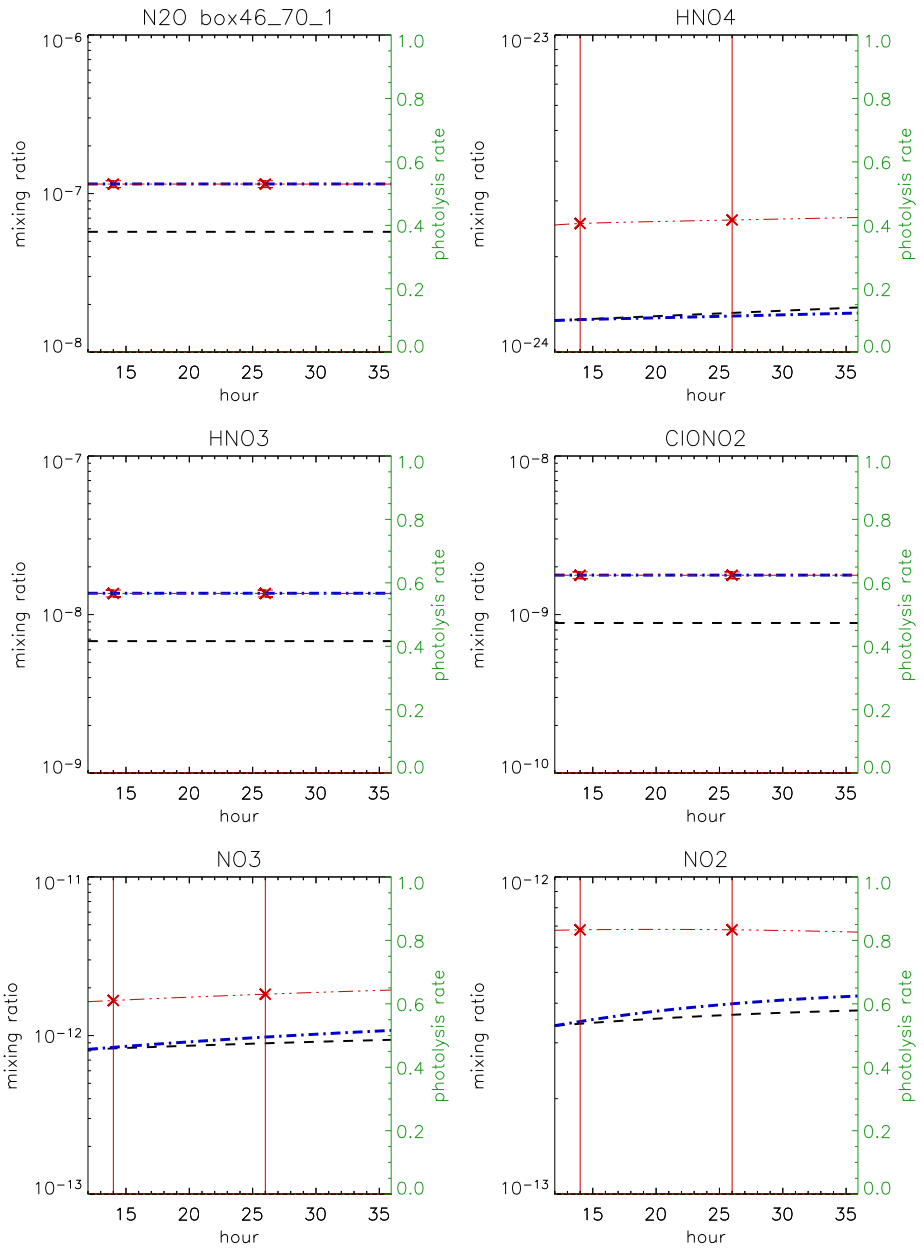

Figure 10.7: *Trace gas concentrations at 82.5°N, 168.75°E (polar night) during experiment BOX1. Dash-triple dotted red line: reference run; red crosses: employed measurements; dashed black line: first guess run; dash-dotted blue line: analysis run; dotted green line (in subsequent figures): photolysis rates.*

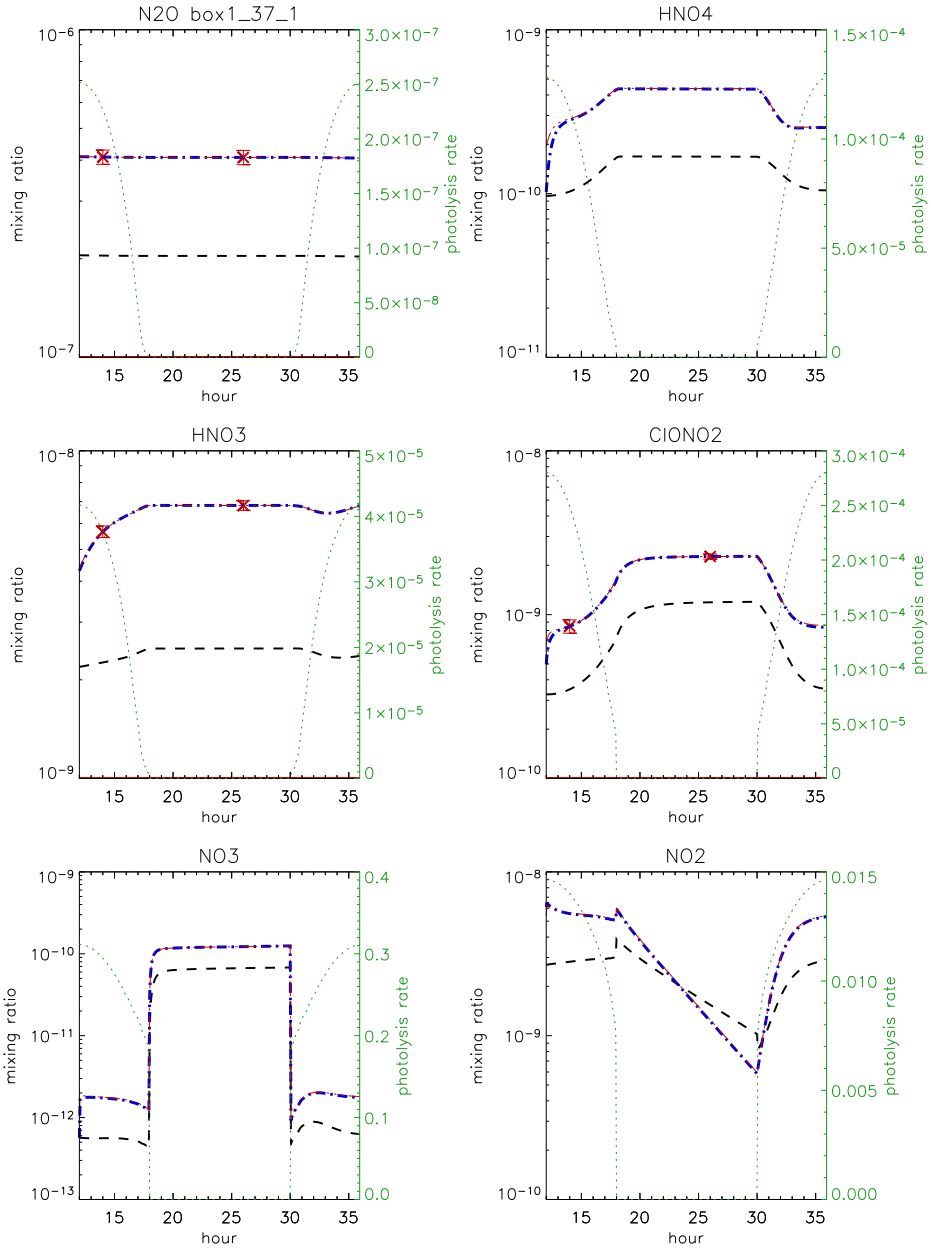

Figure 10.8: *Trace gas concentrations at 0°N,0°E during experiment BOX2. For legend, see Figure 10.7.*

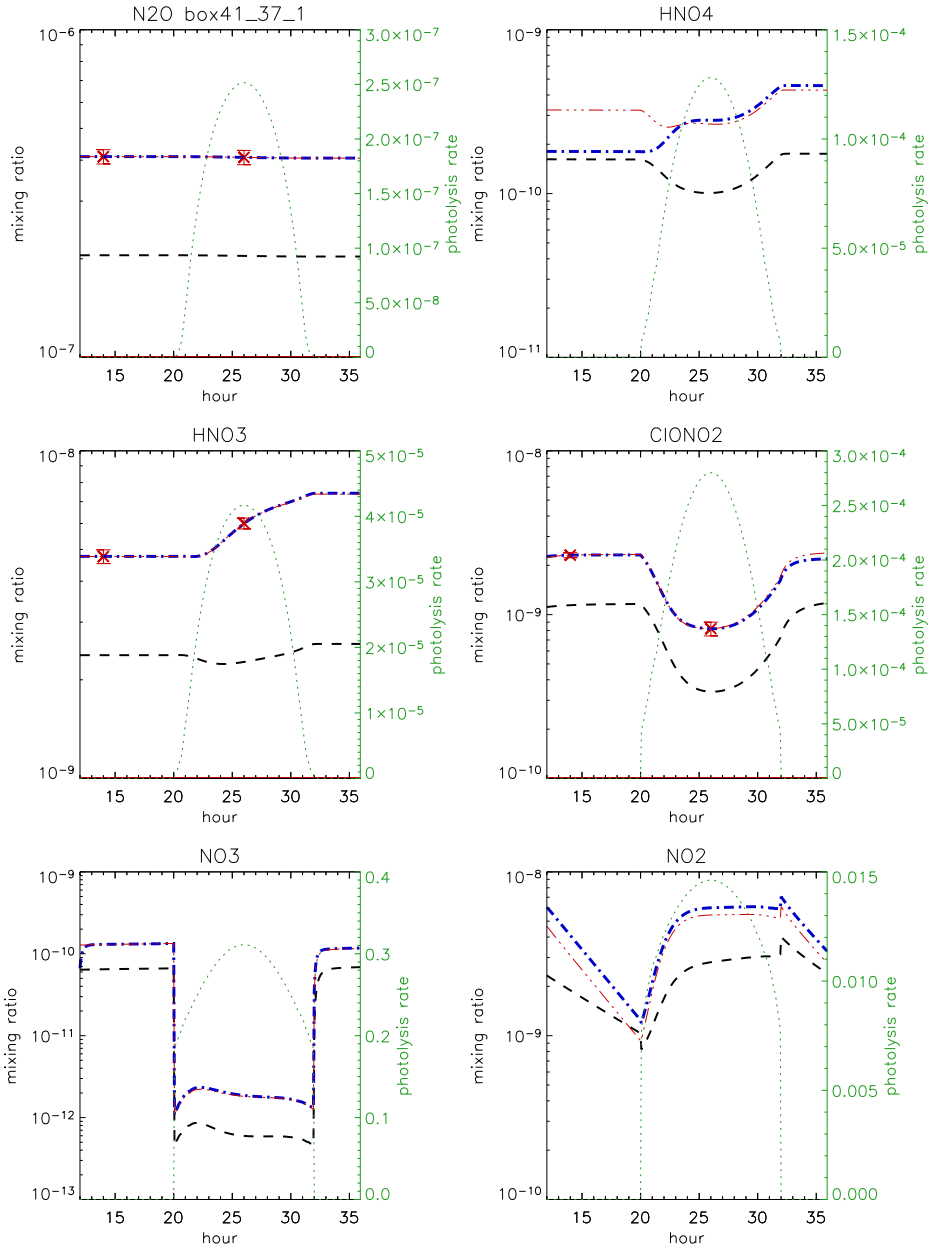

Figure 10.9: *Trace gas mixing ratio at 0°N, 150°E during experiment BOX2. For legend, see Figure 10.7.*

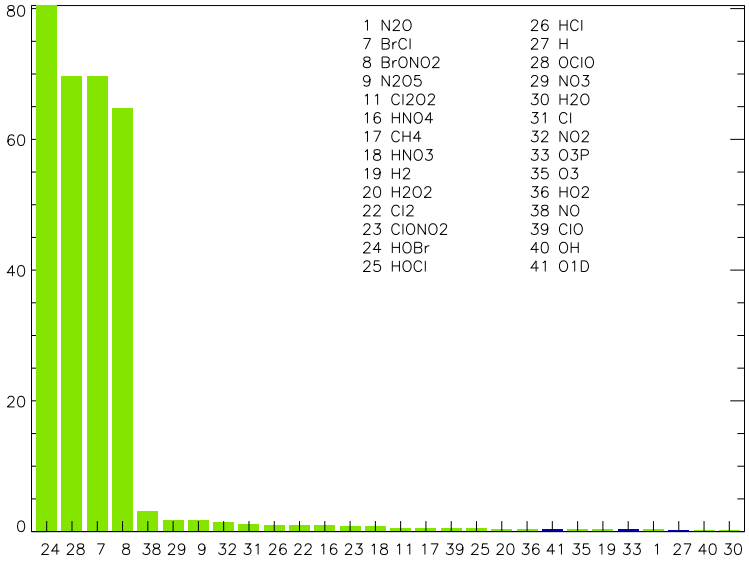

Figure 10.10: *Zonally averaged analysis error at latitude 80°S, experiment BOX1. Green/light gray bars indicate measured species, blue/dark gray bars indicate unmeasured species. Omitted are species with errors larger or equal to 100 %.*

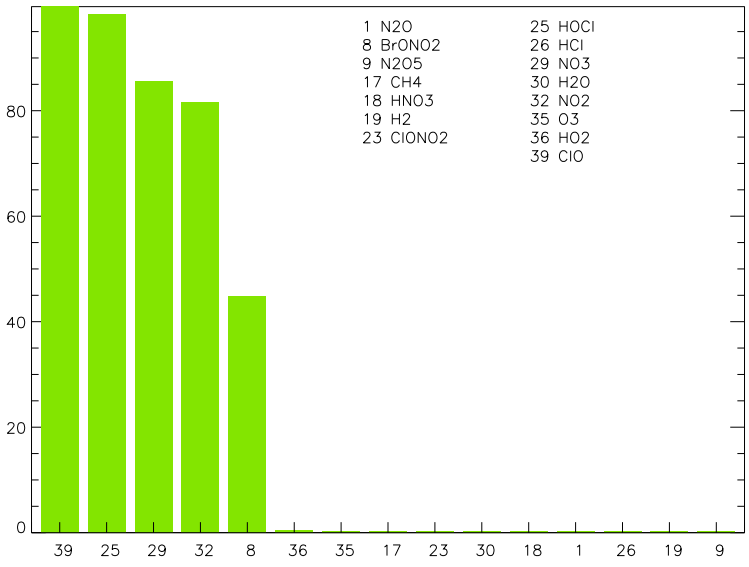

Figure 10.11: *Zonally averaged analysis error at latitude 72.5°N, experiment BOX1. For legend see Figure 10.10.*

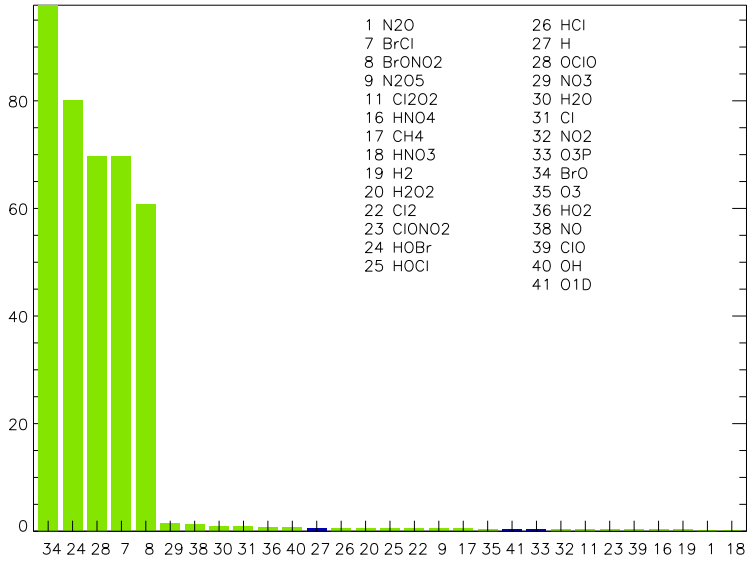

Figure 10.12: *Analysis error averaged over longitudes 0° W–71.25° W at the equator for experiment BOX1. For legend see Figure 10.10.*

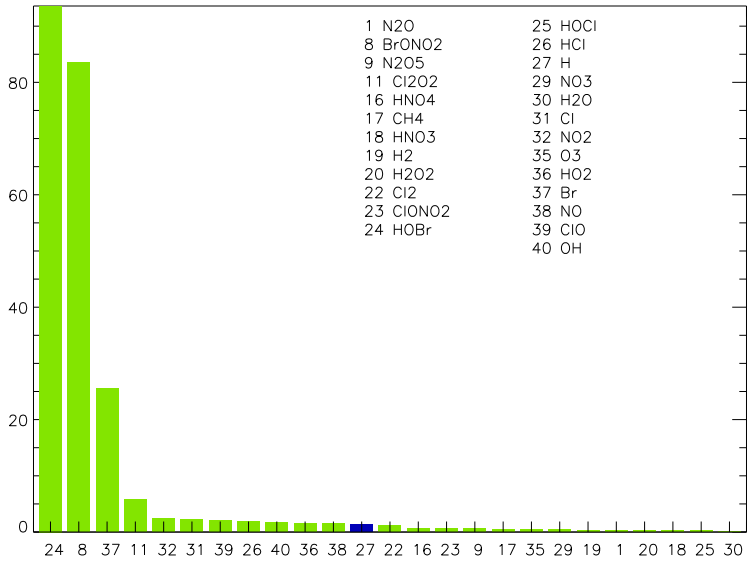

Figure 10.13: *Analysis error averaged over longitudes 150° W–138.75° E at the equator for experiment BOX1. For legend see Figure 10.10.*

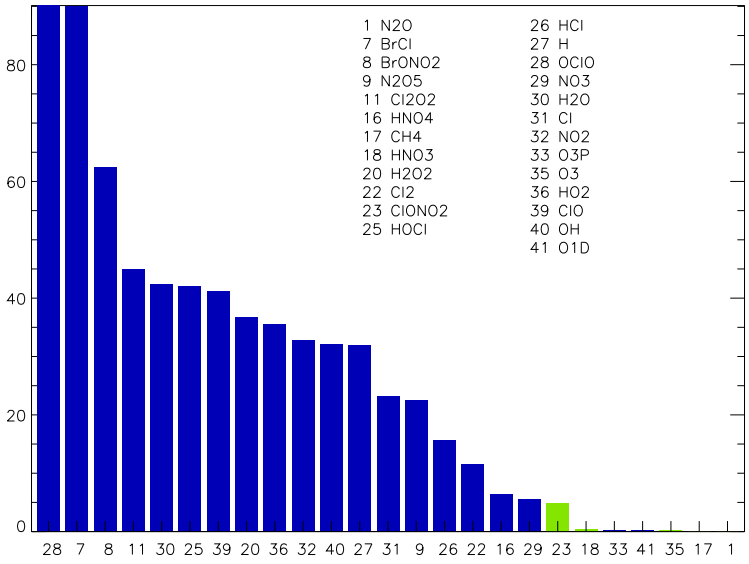

Figure 10.14: *Zonally averaged analysis error at latitude 80°S, experiment BOX2. Green/light gray bars indicate measured species, blue/dark gray bars indicate unmeasured species. Omitted are species with errors larger or equal to 100 %.*

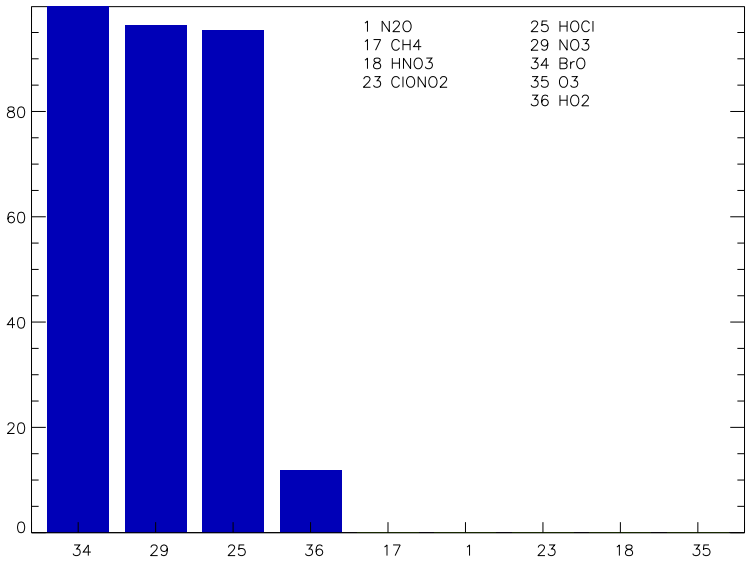

Figure 10.15: *Zonally averaged analysis error at latitude 72.5°N, experiment BOX2. For legend see Figure 10.14.*

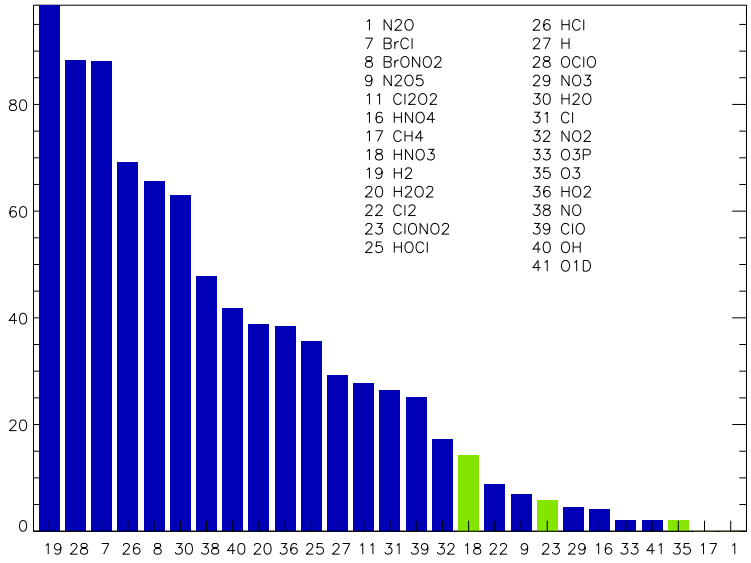

Figure 10.16: *Analysis error averaged over longitudes 0° W–71.25° W at the equator for experiment BOX2. For legend see Figure 10.14.*

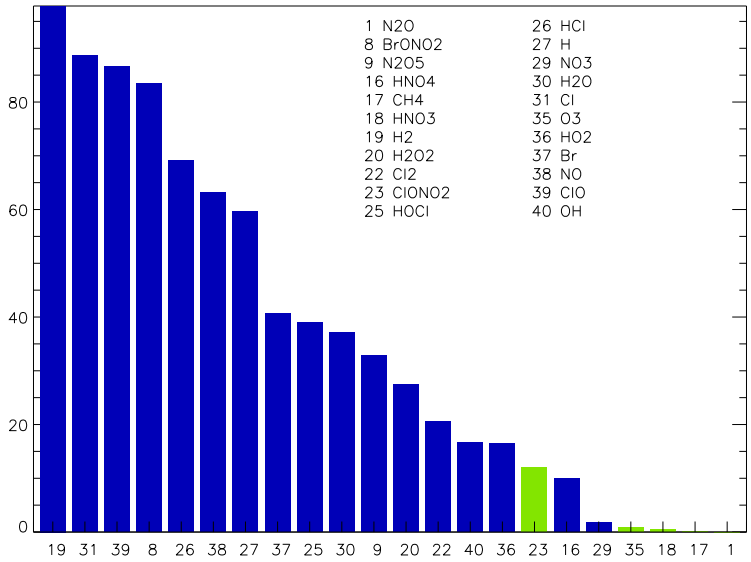

Figure 10.17: *Analysis error averaged over longitudes 150° W–138.75° E at the equator for experiment BOX2. For legend see Figure 10.14.*

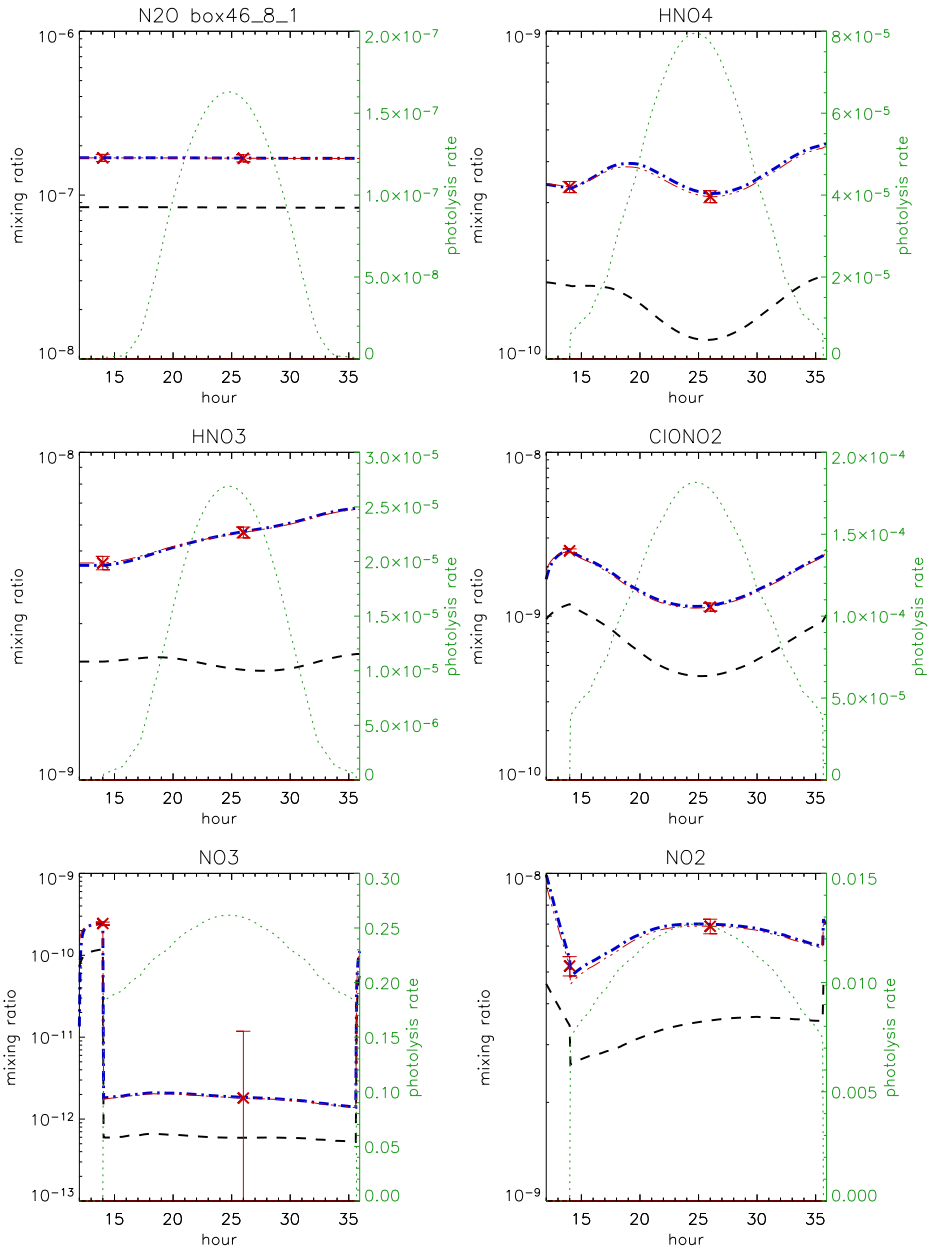

Figure 10.18: *Trace gas mixing ratio at 72.5°S, 168.75°E during experiment BOX1. Dash-triple dotted red line: reference run; red crosses: employed measurements; dashed black line: first guess run; dash-dotted blue line: analysis run; dotted green line: photolysis rates.*

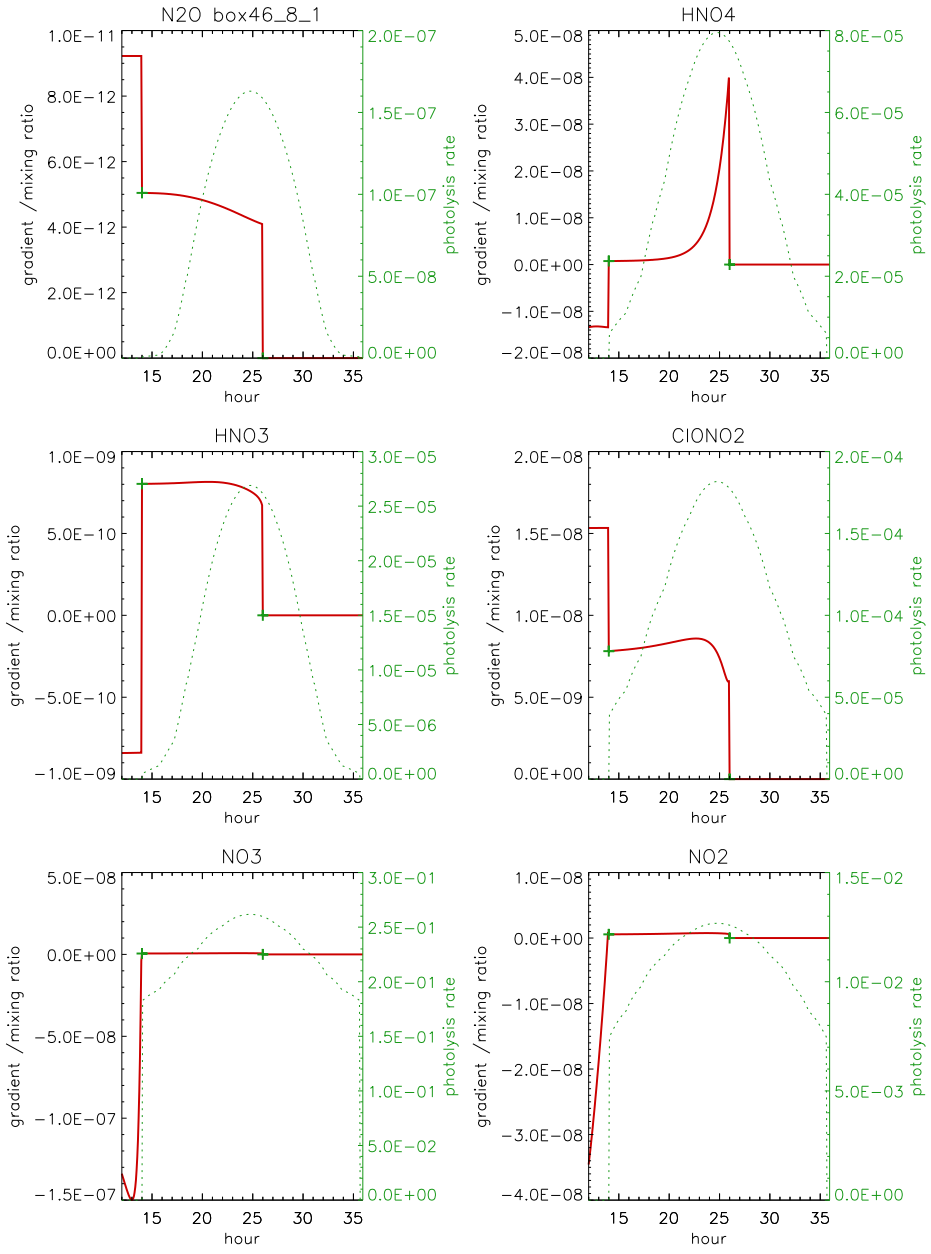

Figure 10.19: *Gradient of the cost function with respect to certain trace gas concentrations at 72.5° S, 168.75° E during experiment BOX1 in red (solid). Green crosses indicate time of measurement for species listed in Table 10.1. Green dotted line: photolysis rates.*

CHAPTER 11

Real Case Experiments

In this chapter, the results from assimilating CRISTA measurements into the AMMOC-CTM will be presented. The first CRISTA episode in November 1994 was chosen for investigation. In this 10 day period during late Antarctic spring, no polar stratospheric clouds occurred so that the use of a model without heterogeneous chemistry is justified. For the chosen episode which was 3 years after the Mount Pinatubo eruption of 1991, Küll (2002) determined that the aerosol loading was still enhanced and that the chemical state of the atmosphere below 15 hPa at northern latitudes was influenced. Therefore, we investigated chemical transformations only at the 10.9 hPa level. The possible daily coverage of the globe between 67° north and 57° south by the CRISTA instrument delivers a wealth of data in this latitude band, but leaves the poles without observations.

11.1 Practical issues

The high computational and storage demands for an adjoint model system computing both transport and chemical transformation for the described chemistry model with 41 species excluded the use of a (3+1)-dimensional model within the framework of this thesis. A (2+1)-dimensional model was employed instead. The results presented here have been obtained by excluding vertical transport and limiting the model to one altitude. As described in Chapter 4, the stratosphere is stably stratified and characterised by long time scales for vertical transport (approximately 20 m/day) in comparison to the chosen duration of the assimilation interval. In consequence, the model represents the relevant processes quite well despite its vertically limited extension.

11.2 Specification of the Error Covariance Matrices

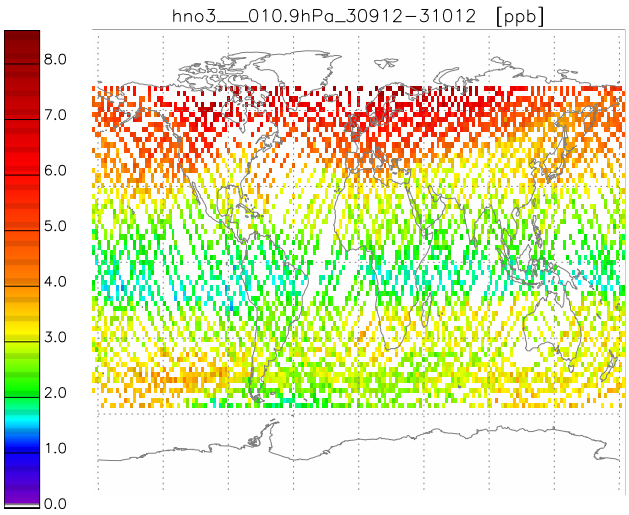

Figure 11.1: *CRISTA HNO_3 measurements between Nov. 5, 12 UTC and Nov. 6, 12 UTC interpolated on 2° by 2° grid.*

In real case experiments, the assimilation system has to determine a compromise between the available information sources of diverse precision. Their relevance for the analysis is weighted by the error covariances. As discussed in Chapter 3, the measurements were attributed to the grid box closest in time and location. This corresponds to **H** in Equation 2.1 being an indicator matrix composed of 0's and, at grid points where observations are available, of 1's.

The various contributions to the CRISTA measurement error were discussed in Chapter 3. In addition to this, the covariance matrix **R** of the cost function (Equation 2.1) has to include the error of representativeness. This is due to the limited resolution of the model grid as compared to the resolution of the measurement technique. The limb scanning mode implies horizontal averaging as discussed in Appendix C. The error related to this fact should already be included in the systematic component of the measurement error. Figure 11.1 shows CRISTA measurements interpolated on a 2° by 2° grid. This grid is considerably finer than the model grid (see Appendix C). As there are visible horizontal correlations, it is justified that each measurement is representative of a model grid box and it suffices to employ the systematic and random errors provided by the retrieval. These errors are listed in Table 11.1.

Further on, the high temporal resolution of the CRISTA measurements needs to be considered. This is respected by assimilating all measurements separately, even if multiple measurements are attributed to the same grid box for the same point in time.

For the background, an error of 100 % of the first guess was tentatively assumed. It is thus much larger than the measurement error because of the high quality of the CRISTA data.

11.3 Configuration of the AMMOC-CTM

For the real case experiment AVER at 10.9 hPa altitude (ca. 32 km), the model was initialized with zonally averaged CRISTA data for the measured species with extension of the southern-/northernmost averages towards the poles. For the other species, results from a box model run were employed. The averaging smoothing technique for the gradient was used. Experiments run without spin-up time showed that the assimilation system only provides a satisfying analysis if the first guess was in chemical equilibrium. Therefore, before starting the assimilation, the following calculations were performed to allow the model to spin up: 1 day chemical transformations without transport, zonal averaging for all species at latitudes 57.5–90°N to smooth the discontinuity developed at the polar night edge, followed by 1 day chemical transformations and transport calculations. Then the assimilation was carried out for a 24 hour period. The result at the end of the assimilation period was used to initialize the next day's experiment. To stabilise the model at the polar night edge on the second day of the assimilation period, zonal means were used north of 72.5°N for initialization. From the third day on, the assimilation result at the end of the previous assimilation period was taken as first guess, using zonal averages for NO_2, HNO_4, HBr, Cl_2, HOBr, HOCl, OClO, BrO and ClO north of 72.5°N. To ensure a stable integration, obviously large gradients were reduced before calling the minimization routine. Minimization was performed for 28 species listed in Table 9.1, omitting CFCs and fast-reacting species such as O^1D, O^3P, and OH. For each day, 40 iterations were permitted.

species	error [%]	covariance [ppb^2]
N_2O	26.1	1.39e+3
CH_4	24.9	6.37e+4
HNO_3	10	1.16e-1
$ClONO_2$	28.6	9.7e-2
O_3	10.5	6.17e+5

Table 11.1: *CRISTA observation errors.*

altitude	10.9 hPa
assimilation period	24 hours (12 UTC to 12 UTC) between Nov. 05, and Nov. 12, 1994
minimum inner chemical time step	10 sec
transported species	28
species evaluated for the cost function	
a) measurements	CRISTA 1 Level 2 Version 5 : O_3, N_2O, HNO_3, $ClONO_2$, CH_4
b) background	28
number of iterations	40
errors for	100 % for diagonal elements,
background error	minimum 0.01 ppb
covariance matrix	0 % for off-diagonal elements

Table 11.2: *Setup of assimilation experiment AVER.*

11.4 Results of experiment AVER

Table 11.3 displays the quality of the analysis as reflected by the value of the cost function for all days of assimilation experiment AVER. A close correspondence between model and observations/background was obtained for all days as the cost function value is reduced in later iterations. The improvement on Nov. 10-11 was the least, reflected by the fact that only 15 of 39 new initial values proposed by the minimization algorithm were accepted, suggesting there was contradictory information, information loss, development of an unrealistic gradient, or errors in the employed wind field. Loss of information can occur if information contained in an adjoint variable is passed to another variable which is not included in the minimization process (see Table 9.1). The assimilation result of the next day showed a larger improvement, which suggests that on Nov. 10-11 there were specific reasons inhibiting a more satisfying decrease of the cost function. At first sight, it is surprising that the cost function of the first iteration is higher on the second day than on the first day. The explanation is given by the third column in the same table: the number of observations. On the first day, CRISTA started measuring at 16:41 UTC in stratosphere-mesosphere mode, thus, some areas were not covered by measurements, others with a reduced density, and the assimilation system was therefore less constrained by measurements, resulting in a smaller cost function value. On this day, unobserved regions could not be improved in the analysis. As an example, Figure 11.2 shows the difference between the model state during the first iteration and during the final analysis for N_2O at 00 UTC, the middle of the assimilation interval. The trace gas field in a large area over Europe and Asia was left unchanged. Starting on Nov. 5, 17:44 UTC until Nov. 8, 11:49 UTC, CRISTA was operating in stratosphere mode, resulting in a

considerably higher measurement density at this altitude in the described latitude band. The ratio cf1/nobs (see Table 11.3) is considerably less on Nov. 5-6 than on Nov. 4-5, implying Nov. 5 was initialized better than Nov. 4, the model has thus "learned" from the assimilation on the previous day. From the third day on, the cost function of the first iteration normalised by the number of observations is between 1.4 and 2.2 and thus smaller than the first day; taking Nov. 10-11 as an exception, the ratio is less than 1.8 and smaller than the first two days. This shows that the model needed two days to produce an analysis which is a valuable first guess for the next assimilation period. The brevity of the spin-up period is to a large extent due to the high measurement density of CRISTA.

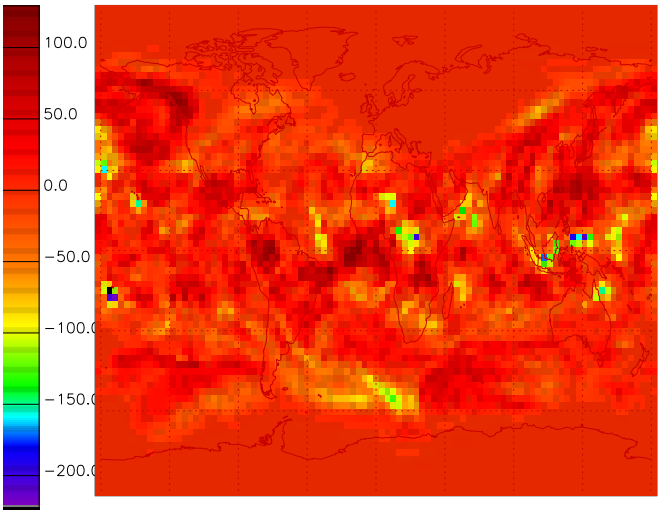

Figure 11.2: *Change of N_2O [ppb] on the first day of the episode.*

11.4.1 Detailed analysis for specific regions and atmospheric constituents

In the northern hemisphere, CRISTA measured southward of 67°, which corresponds to grid box 64. The polar night extended from the north pole to grid box 66. Therefore, the model had to cope with a twofold discontinuity: the data edge and the polar night edge. As discussed in Chapter 10.2, the reduced chemical activity during the polar night hinders successful approximation of the measurements by the model in that area. Even though CRISTA did not measure at these latitudes, some measurements were taken close enough that the information was transported into the polar night area during the 24 hour assimilation period.

At this altitude, nitrous oxide is an interesting tracer. Its mixing ratio at equatorial latitudes is larger than at middle or polar latitudes. Figures 11.3 to 11.5 show measurements, first guess and analysis for the first day. Due

day	cost function first iteration (cf1)	cost function last iteration	number of observations (nobs)	$\frac{\text{cf1}}{\text{nobs}}$
Nov. 4-5	56 059	6 215	14 340	3.91
Nov. 5-6	69 894	11 343	32 906	2.12
Nov. 6-7	55 515	15 815	40 283	1.38
Nov. 7-8	48 413	4 871	31 536	1.54
Nov. 8-9	20 751	1 832	12 726	1.63
Nov. 9-10	44 372	8 924	20 329	2.18
Nov. 10-11	64 545	19 889	36 106	1.79
Nov. 11-12	25 565	8 872	17 062	1.50

Table 11.3: *Cost function and observation density for assimilation experiment AVER.*

to the assimilation, the modelled maximum is reduced from 327 ppb to 285 ppb. The displayed measurements' maximum is 226 ppb, but the actually measured maximum of 272 ppb is higher than that of the displayed measurements. This discrepancy is due to the averaging over all measurements in this grid box during a 24 hour period for the visualisation. Thus, the analysis maximum agrees with the measured maximum within the error bounds of 37 ppb. Transport during the spin-up has transported nitrous-oxide rich air towards the south pole. Assimilation has reduced mixing ratios close to southern South America in the air mass belonging to the polar vortex. Figures 11.6 to 11.8 show measurements, first guess and analysis for the last day. Again, due to the assimilation, the modelled maximum is reduced, in this case from 327 ppb to 285 ppb, compared to the measured maximum of 272 ppb. One reason might be measurements of the previous days as the maximum measured the day before was 290 ppb. The assimilation result now clearly shows the southern polar vortex with low nitrous oxide mixing ratios displaced towards South America. Further on, a streamer of N_2O rich air extends from low latitudes over Asia. The N_2O mixing ratios north of 72.5°N are reduced compared to the first day. This seems realistic since the air mass sampled over the North Atlantic is assumed to belong to the northern polar vortex. These examples illustrate how information is transported from observed to unobserved regions during the assimilation period.

Figure 11.9 shows the analysis for N_2O in the southern hemisphere on Nov. 6, 00 UTC. At 40°S, a streamer of N_2O rich air is visible. Riese et al. (2001) showed that this is a remnant of tropical air. On Nov. 11, 00 UTC (Figure 11.10) N_2O rich air is found at the south pole which is still connected to its source region.

Chlorine nitrate shows the complementary nature of modelling and observations: the analysis on Nov. 11 (Figure 11.11) reveals that daytime

mixing ratios are considerably lower than nighttime mixing ratios. Values less than 0.5 ppb appear mostly south of 40°N because chlorine nitrate relaxes slowly during the day towards the minimum and the day is short north of this latitude. For comparison, Figure 11.12 shows CRISTA measurements on the same day. Due to the low observation density on this day, the averaging effect is small. As one can see, the measured values are larger than the minimum modeled daytime values. This is due to the local time of measurements: $ClONO_2$ mixing ratios reach low values only some time after sunrise, but CRISTA daylight measurements south of 40°N are taken rather soon after sunrise when $ClONO_2$ mixing ratios are still large. (The local time of CRISTA shifts about 22 minutes per day (Riese, 2000), thus, 3 hours during the episode.)

11.5 Use of the curvature penalty term in the cost function: experiment CURV100

Making use of the curvature penalty term of the cost function instead of the averaging smoothing technique, an assimilation experiment was carried out which was otherwise identical to the above described experiment AVER. As discussed in Chapter 7, the weights of the curvature penalty term were chosen to be 10^{-9} for the first 7 iterations, 10^{-10} for iteration 8 to 11 and 10^{-11} for all later iterations and replaced averaging of the calculated gradient before calling the minimization routine. Figures 11.13 to 11.14 show the assimilation results corresponding to those of Section 11.4.1. The maximum of the analysis is again higher than that of the measurements. It is outside the error bound even for the higher mixing ratio measured the day before. Table 11.5 lists the contribution of the different terms to the cost function. For the last iteration, the contribution of the curvature term is several orders of magnitude smaller than both the measurement deviation and the background deviation and reflects the fact that the employed curvature term weights are less than the measurement and background weights. This is mandatory to make this experiment amenable to the a posteriori verification of the employed error covariances described in Chapter 12.

11.6 Comparison of the assimilation experiments AVER and CURV100

For several species the analyses for CURV100 are less smooth than the analyses for AVER. This can be attributed to the small weights for the curvature penalty term compared to the averaging of the gradient in AVER which implied that each of the four adjacent grid boxes' gradients contributed 12.5% to the gradient at the center grid point. Comparison of the mea-

day	cost function first iteration (cf1)	cost function last iteration	number of observations (nobs)	$\frac{\text{cf1}}{\text{nobs}}$
Nov. 4-5	56 059	5 888	14 340	0.4106
Nov. 5-6	77 194	13 156	32 906	0.3998
Nov. 6-7	65 178	18 913	40 283	0.4695
Nov. 7-8	51 891	4 972	31 536	0.1577
Nov. 8-9	20 906	1 503	12 726	0.1181
Nov. 9-10	46 059	8 892	20 329	0.4342
Nov. 10-11	69 697	18 882	36 106	0.5509
Nov. 11-12	26 074	7 350	17 062	0.5202

Table 11.4: *Cost function and observation density for assimilation experiment CURV100.*

day	background contribution	measurement contribution	curvature contribution	cost function total
Nov. 4-5	1 767	4 120	0.23	5 888
Nov. 5-6	2 003	11 152	0.27	13 156
Nov. 6-7	1 127	17 785	0.26	18 913
Nov. 7-8	1 110	3 861	0.20	4 972
Nov. 8-9	531	972	0.08	1 503
Nov. 9-10	887	7 939	0.17	8 826
Nov. 10-11	1 759	17 123	0.24	18 882
Nov. 11-12	416	6 934	0.08	7 350

Table 11.5: *Background, observation and penalty term's contribution to the cost function for the analyses of assimilation experiment CURV100.*

day	cost function AVER	cost function CURV100
Nov. 4-5	56 059	56 059
Nov. 5-6	69 894	77 194
Nov. 6-7	55 515	65 178
Nov. 7-8	48 413	51 891
Nov. 8-9	20 751	20 906
Nov. 9-10	44 372	46 059
Nov. 10-11	64 545	69 697
Nov. 11-12	25 565	26 074

Table 11.6: *Forecast quality as measured by the observation contribution to the cost function for the first iteration for experiments AVER and CURV100.*

surement contribution to the cost function for the first iteration in Table 11.6 shows that the analyses of AVER give a better forecast than the analyses of CURV100 even though the analysis of CURV100 on some days is in closer correspondence with the observations than that of AVER. Thus, the smoothing influence seems to have a positive impact on the forecast quality of the analysis. In case of the weak curvature penalty term, the model is able to fit the observations during the assimilation interval, but the degree of fitting has a negative impact on the forecast quality. It is assumed that the representativity of the measurement was overestimated, or, in other words, an over-fitting occurred. This can happen if the measurement is different from the average value for the grid box. In principle, this should be avoided by the employed representativeness error, but the error is only relevant in comparison to other information. Here, the other information source is the background for which a large error was assumed. The size of the background error allows the assimilation system to produce an analysis close to the measurements because a large background error attributes more relevance to the observations. This means that an increase of the curvature penalty term weights and a decrease of the background error can possibly contribute to a better forecast. Therefore, a new series of assimilation experiments could be carried out where the curvature penalty term weights should be increased to see whether a smoother analysis is a better initialization for the next day. In the new experiment the contribution of the curvature penalty term should nevertheless remain small compared to the background and measurement contribution.

11.7 Assimilation experiment CURV50

day	cost function for CURV50
Nov. 5-6	77 188
Nov. 6-7	66 797
Nov. 7-8	53 069
Nov. 8-9	21 491
Nov. 9-10	47 369
Nov. 10-11	73 798
Nov. 11-12	26 080

Table 11.7: *Forecast quality as measured by the observation contribution to the cost function for the first iteration for experiment CURV50.*

The a posteriori examination of the experiments AVER and CURV100, which is discussed in detail in Chapter 12, revealed that the background error was probably smaller than 100 %. Therefore, to investigate the influence

of the background error covariance matrix on the quality of the analysis, a third assimilation experiment named CURV50 was carried out where, starting on the second day of the episode, the background error was assumed to be 50 % of the first guess value. In all other aspects the experiment was identical to experiment CURV100. The results confirmed the background error to be closer to 50 % than 100 %. Figures 11.15 shows the analysis of nitrous oxide on Nov. 11 for comparison with the previous experiments. It is much smoother than in experiment CURV100, but the forecast quality is not improved in terms of the observation contribution to the cost function during the first iteration as can be seen from the comparison of Tables 11.6 and 11.7.

11.8 Discussion

The assimilation of CRISTA data in the (2+1)D CTM was carried out successfully. One of the results are the produced synoptic maps. The map of nitrous oxide shows that at the end of the experiment, unobserved regions like the south polar vortex were provided with information due to transport from the observed region. This is due to the vortex being displaced towards South America during the episode so that the edge of the vortex extended into the area covered by CRISTA measurements. The streamer extending from low latitudes over Asia confirms the decision to increase the model resolution.

Chlorine nitrate maps show the advantage over interpolation as its lowest mixing ratios during the day in the southern hemisphere were not captured by CRISTA.

Even though CRISTA shows a high measurement density, not every model grid box in the observed region was attributed a measurement during each assimilation period. As a remedy, we employed two different methods to spread the information. Both allowed a stable integration. The use of the curvature penalty term in experiment CURV100 lead to a closer coincidence of measurements and analyses than in experiment AVER, at the expense of the forecast quality. The main reason for the better coincidence is that, in the last iteration, the effect of the curvature penalty term was smaller than the effect of the averaging smoothing method.

An a posteriori examination showed that the background error assumed for these two experiments was too large. This might be the reason for the over-fitting in experiment CURV100. This is confirmed for nitrous oxide in experiment CURV50 where the background error was reduced to 50% and which resulted in a smoother analysis.

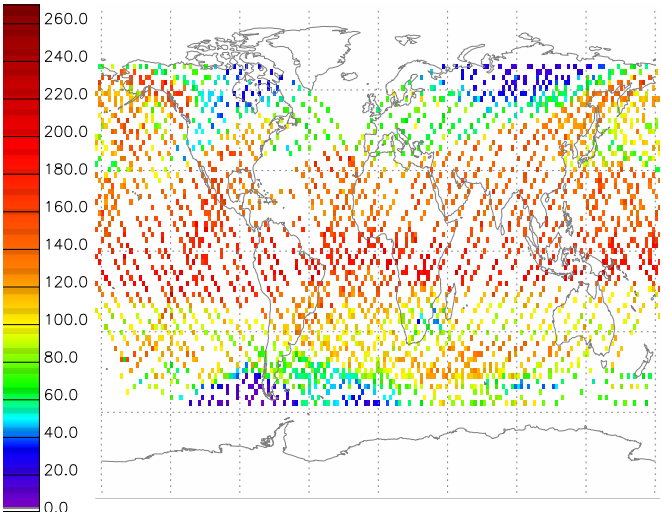

Figure 11.3: *Nitrous oxide measurements during the first day of the assimilation period, Nov. 4, 12 UTC to Nov. 5, 12 UTC, interpolated on 2x2° grid. Plotted maximum is 226 ppb due to averaging, measured maximum is 272 ppb.*

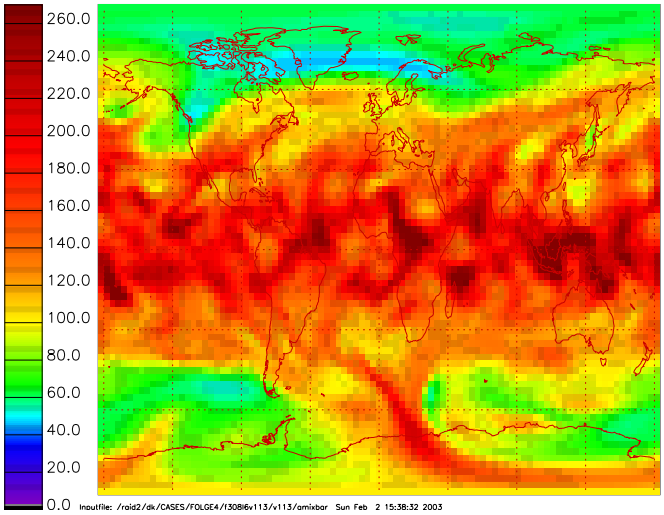

Figure 11.4: *Nitrous oxide first guess Nov. 4, 12 UTC after 48h spin-up period experiment AVER. Maximum is 344 ppb.*

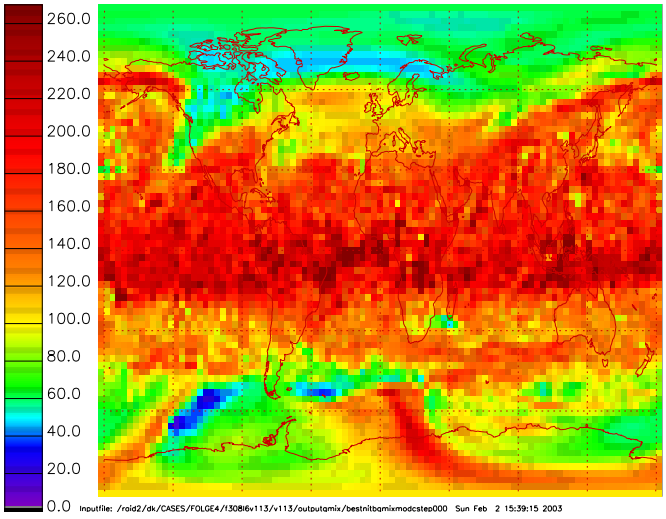

Figure 11.5: *Nitrous oxide assimilation result Nov. 4, 12 UTC experiment AVER. Maximum is 315 ppb.*

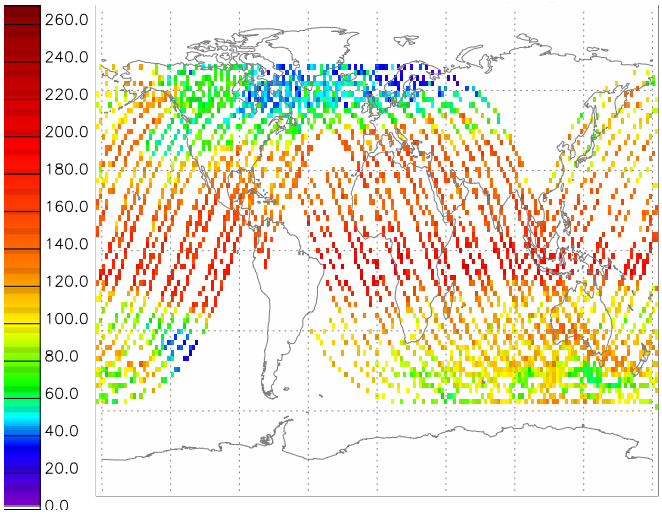

Figure 11.6: *Nitrous oxide measurements during the last day of the assimilation period, Nov. 11, 12 UTC to Nov. 12, 12 UTC interpolated on 2x2° grid. Plotted maximum is 215 ppb, measured maximum is 255 ppb.*

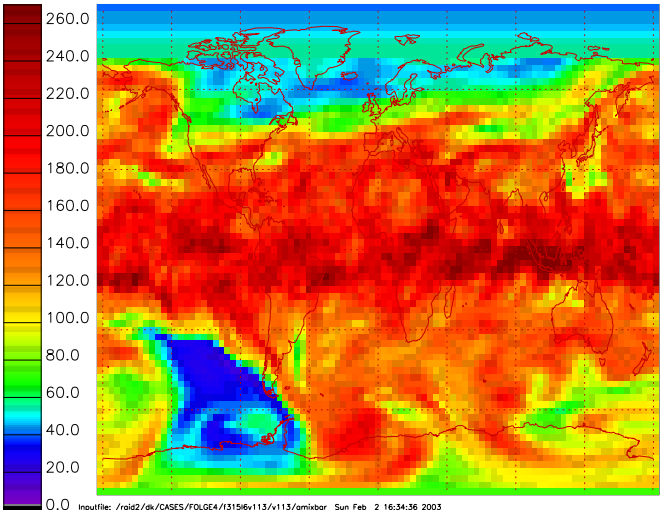

Figure 11.7: *Nitrous oxide first guess Nov. 11, 12 UTC experiment AVER. Maximum is 327 ppb.*

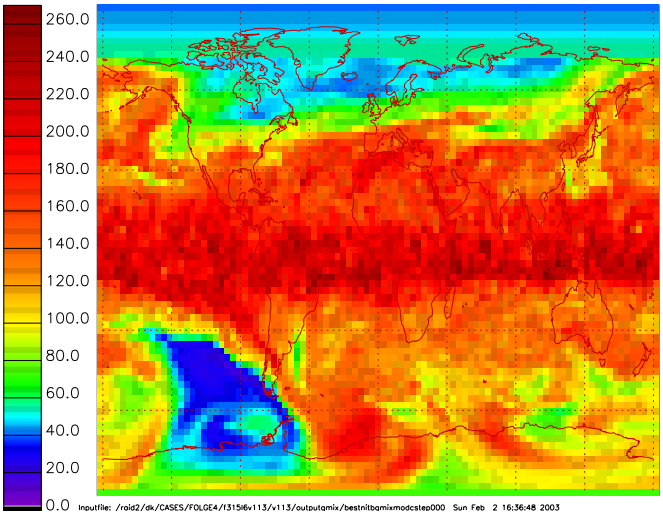

Figure 11.8: *Nitrous oxide assimilation result Nov. 11, 12 UTC experiment AVER. Maximum is 285 ppb.*

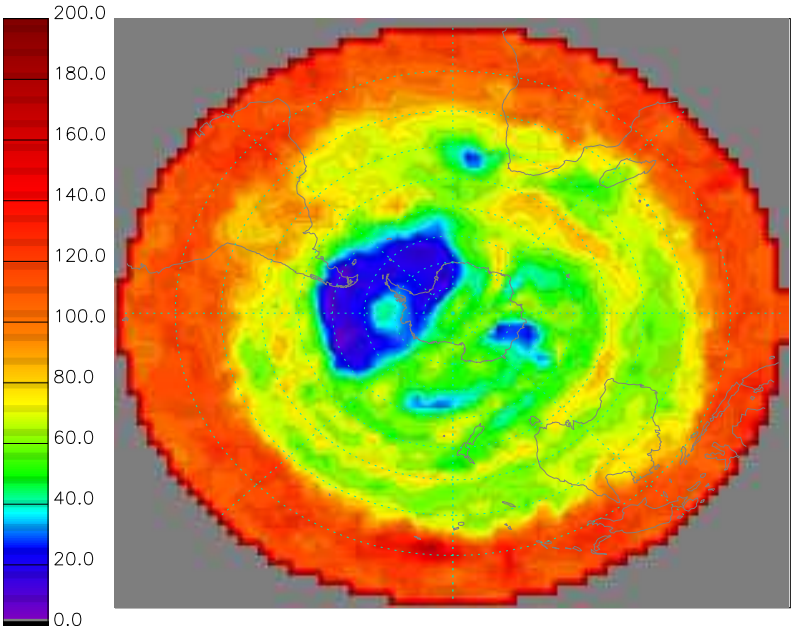

Figure 11.9: *Nitrous oxide analysis for the southern hemisphere on Nov. 7, 00 UTC. The N_2O rich streamer is visible at 40°S. Maximum is 380 ppb.*

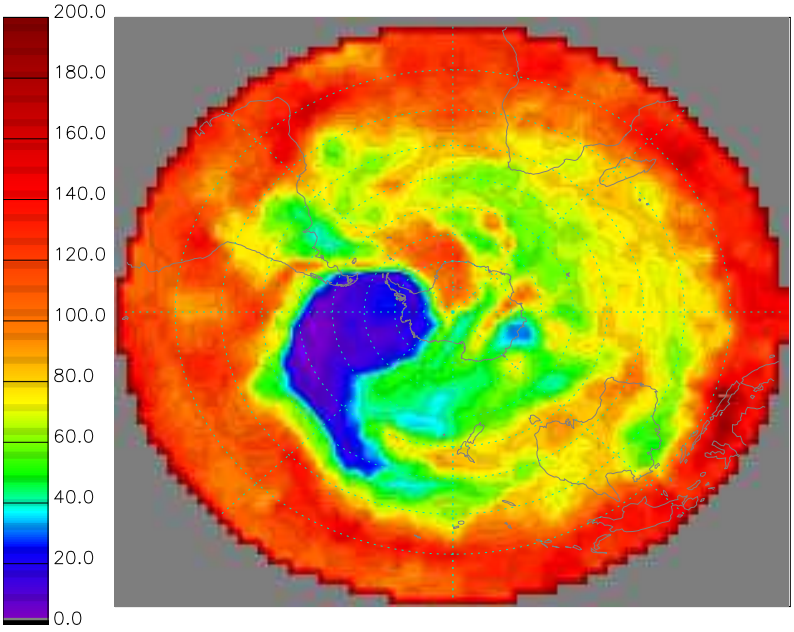

Figure 11.10: *Nitrous oxide analysis for the southern hemisphere on Nov. 12, 00 UTC. Maximum is 340 ppb.*

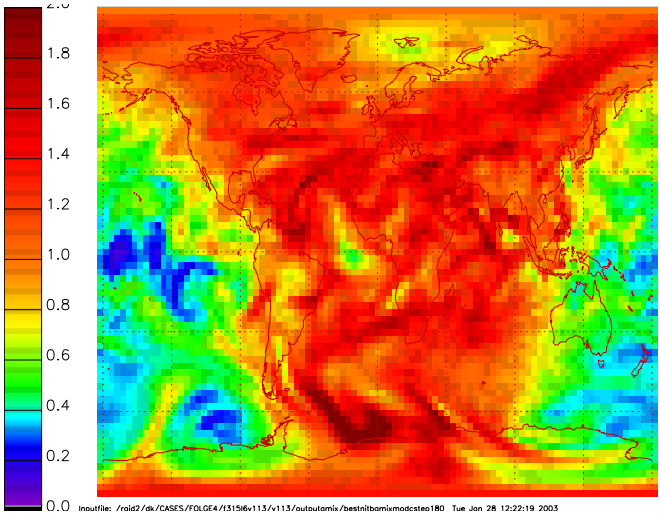

Figure 11.11: *Analysis of chlorine nitrate mixing ratio [ppb], Nov. 12, 00 UTC.*

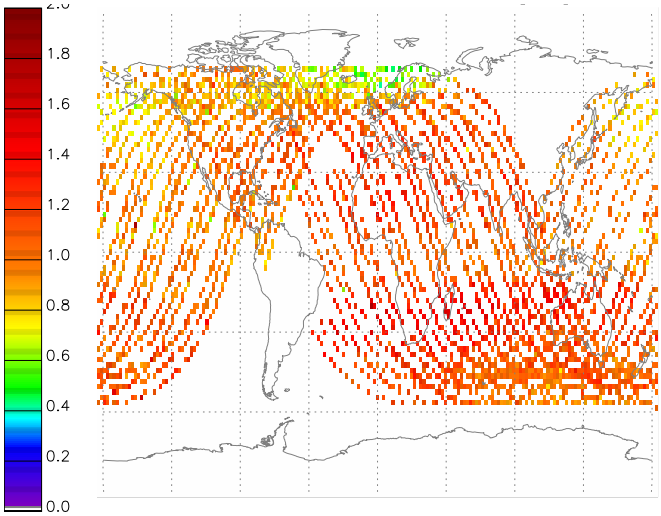

Figure 11.12: *Chlorine nitrate measurements between Nov. 11, 12 UTC and Nov. 12, 12 UTC on 2x2° grid.*

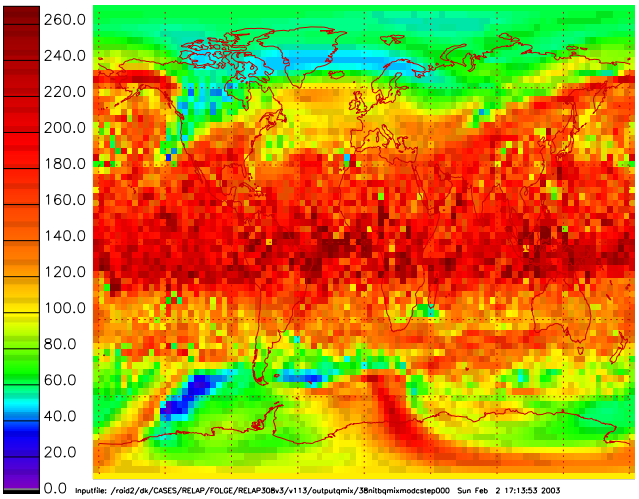

Figure 11.13: *Nitrous oxide assimilation result Nov. 04, 12 UTC for experiment CURV100. Maximum is 350 ppb. Compare to Figure 11.5.*

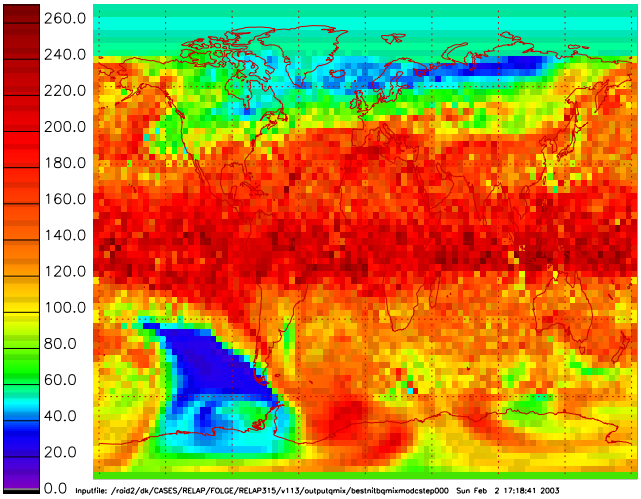

Figure 11.14: *Nitrous oxide assimilation result Nov. 11, 12 UTC for experiment CURV100. Maximum is 354 ppb. Compare to Figure 11.8.*

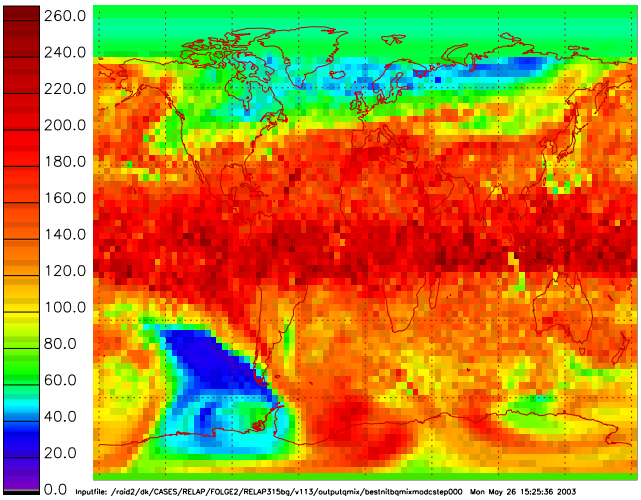

Figure 11.15: *Nitrous oxide assimilation result Nov. 11, 12 UTC for experiment CURV50. Maximum is 377 ppb. Compare to Figure 11.8 and 11.14.*

CHAPTER 12

A posteriori examination of the error covariance matrices

In sufficient vicinity of the optimal solution, the initial values of the model system are uniquely defined by measurements and background knowledge. The relative influence of the different information sources is weighted by the error covariance matrices in the cost function. Presently, only the variances are taken into account, thus only the main diagonal entries in the corresponding matrices are assigned. While the determination of the measurement error is performed by the experimenters, the background errors must be ascertained by the assimilation system. Nevertheless, efforts should be undertaken to verify the assumptions employed in the formulation of the cost function. Talagrand (1998) has proposed a test to control the chosen covariances a posteriori. Here, it suffices to demonstrate the idea for the 3D case, the extension to the 4D case is straightforward. In the following,

$$\mathbf{d} = \mathbf{y}^o - \mathbf{H}\mathbf{x}^b$$

denotes the innovation vector as the difference between measurement $\mathbf{y}^o$ and the background value $\mathbf{x}^b$ interpolated by $\mathbf{H}$ from the model grid space to the location of the measurement. $\mathbf{y}^o$ and $\mathbf{x}^b$ can be separated into the true values $\mathbf{y}^t$ and $\mathbf{x}^t$ and errors ϵ_y and ϵ_b so that $\mathbf{d} = \mathbf{y}^t + \epsilon_y - \mathbf{H}(\mathbf{x}^t + \epsilon_b)$. It is assumed that the background information determines the model state unequivocally without overdetermination. If there are p measurements, then p is the degree of total overdetermination. If we knew the 'true' observation and background error covariance matrices, $\mathbf{R}$ and $\mathbf{B}_o$, the minimum of the cost function was

$$J_{\min} = \frac{1}{2}\mathrm{trace}\left((\mathbf{H}\mathbf{B}\mathbf{H}^T + \mathbf{R})^{-1}\mathbf{d}\mathbf{d}^T\right) \ .$$

Under the assumption of uncorrelated background error and measurement error covariance matrices, one finds

$$\begin{aligned} E(\mathbf{d}\mathbf{d}^T) &= E(\epsilon_y \epsilon_y^T) + E(\mathbf{H}\epsilon_b \epsilon_b^T \mathbf{H}^T) \\ &= \mathbf{R} + \mathbf{H}\mathbf{B}\mathbf{H}^T \ , \end{aligned} \tag{12.1}$$

where E is the expectation value. Considering a sufficiently large number of observations, one obtains the following expectation for the minimum of the cost function:

$$\begin{aligned} E(J_{\min}) &= \frac{1}{2} E(\mathrm{trace}((\mathbf{H}\mathbf{B}\mathbf{H}^T + \mathbf{R})^{-1}\mathbf{d}\mathbf{d}^T) \\ &= \frac{1}{2} \mathrm{trace}((\mathbf{H}\mathbf{B}\mathbf{H}^T + \mathbf{R})^{-1} E(\mathbf{d}\mathbf{d}^T)) \\ &= \frac{1}{2} \mathrm{trace}(\mathbf{I}_p) = p/2, \end{aligned} \tag{12.2}$$

where in the last step Equation 12.1 was used.

The contribution of the curvature penalty term to the cost function at the minimum is much smaller than the background and measurement term contribution because of the small weights for later iteration. It was always less than 0.1%. Therefore, the contribution of the curvature penalty term can be neglected in the following. Further on, $\mathbf{H}$ was chosen to be an attribution of the observation to the closest model grid point. Therefore, it can be assumed in the following that the observations are given on the model grid and $\mathbf{H}$ can therefore be dropped.

In assimilation experiment AVER, the background variance was chosen to be 100% of the first guess. For the later days of the CRISTA episode, the number of observations was on average more than twice the value of the cost function at the minimum. Under the assumption that the employed measurement error variances are correct, this indicated that the first guess was better than assumed by the background error variances. As a consequence, the background variance was decreased to 50% in the following assimilation experiment CURV50, which in all other aspects was identical to experiment CURV100. Table 12.1 lists the value of $\frac{J_{\min}}{p}$ for the described experiments. The values for experiment CURV50 are on average closer to 0.5 than for the other two experiments. Therefore, it can be assumed that the background error is about 50% of the first guess value.

In another validation method the chosen covariance matrices are compared to the information minus analysis increment. The information vector $\mathbf{z}$ denotes the composite of background knowledge and observations. Another description of the atmospheric state is the obtained analysis $\mathbf{x}^a$. Under the assumption that background knowledge and observations are uncorrelated, the error covariance matrix of the information vector separates into $\mathbf{B}$ and

Table 12.1: $\frac{J_{\min}}{p}$ **for three assimilation experiments**

day	AVER	CURV100	CURV50
Nov. 4-5	0.4334	0.4106	
Nov. 5-6	0.3447	0.3998	0.4870
Nov. 6-7	0.3926	0.4695	0.5688
Nov. 7-8	0.1545	0.1577	0.2313
Nov. 8-9	0.1440	0.1181	0.2332
Nov. 9-10	0.4390	0.4342	0.4943
Nov. 10-11	0.5509	0.5203	0.5627
Nov. 11-12	0.5202	0.4308	0.5198
average over episode	0.3637	0.3615	0.4424

$\mathbf{R}$ and the information minus analysis (**ImA**) vector $\mathbf{z}-\mathbf{x}^a$ is separated into $\mathbf{x}^b-\mathbf{x}^a$ and $\mathbf{y}^\circ-\mathbf{x}^a$. For the true state $\mathbf{x}^t$, the following expression describes the expectation value of the ImA covariance matrix:

$$E((\mathbf{z}-\mathbf{x}^a)(\mathbf{z}-\mathbf{x}^a)^T) = E((\mathbf{x}^t-\mathbf{z})(\mathbf{x}^t-\mathbf{z})^T)-E((\mathbf{x}^a-\mathbf{x}^t)(\mathbf{x}^a-\mathbf{x}^t)^T) \quad (12.3)$$

The first covariance matrix on the right hand side is a block matrix composed of $\mathbf{B}$, $\mathbf{R}$ and zeros. The entries in the second covariance matrix on the right hand side are larger than zero. Therefore, the difference between the information vector $\mathbf{z}$ and the analysis $\mathbf{x}^a$ should at most be equal to the corresponding covariance in $\mathbf{B}$ or $\mathbf{R}$. A system that fulfills this condition is called efficient. The more information available, the less $E((\mathbf{z}-\mathbf{x}^a)(\mathbf{z}-\mathbf{x}^a)^T)$ should be so that in the end, the approximation

$$E((\mathbf{z}-\mathbf{x}^a)(\mathbf{z}-\mathbf{x}^a)^T) \leq E((\mathbf{x}^t-\mathbf{z})(\mathbf{x}^t-\mathbf{z})^T)$$

or

$$\begin{pmatrix} E((\mathbf{x}^b-\mathbf{x}^a)(\mathbf{x}^b-\mathbf{x}^a)^T) & 0 \\ 0 & E((\mathbf{y}^o-\mathbf{x}^a)(\mathbf{y}^o-\mathbf{x}^a)^T) \end{pmatrix} \leq \begin{pmatrix} \mathbf{B} & 0 \\ 0 & \mathbf{R} \end{pmatrix} \quad (12.4)$$

should hold. While the left hand side of Relation 12.4 can be calculated a posteriori from the analysis and the employed observations, the right hand side is given by the employed error covariances. In consequence, if a sound statistical basis is given by a sufficiently long assimilation period, we can check a posteriori whether the error covariance matrices are consistent with the obtained analysis. It should be kept in mind, however, that the result of the estimation process constitutes a balance between all employed information elements and their errors. This implies that a violation of Equation

12.4 must be interpreted in the context of the whole system. Further on, this test allows the falsification of the error covariance matrices, but Equation 12.4 can also be fulfilled by incorrect error covariance matrices in case the incorrections compensate each other.

The idea shall be illustrated by a one-dimensional example (where the estimation is based on one single realization). The truth shall be described by the function $x(t) = 2t$. The background information is $x^b(4) = 8$ with variance 1 and the observations are $y^o(2) = 3$ and $y^o(6) = 11$ with variance 1. The truth lies within the given errors. The method of least squares results in the analysis {(2,3.33),(4,7.33),(6,11.33)} that agrees with background and observations within the assumed error bounds. Evaluation of 12.4 gives the true statement

$$\begin{pmatrix} 0.45 & 0 \\ 0 & 0.11 \end{pmatrix} \leq \begin{pmatrix} 1 & 0 \\ 0 & 1 \end{pmatrix}.$$

Now assume degraded observations, but the same error variances (which are now too small): {(2,2),(4,8),(6,10)}. The analysis is then given by {(2,2.67),(4,6.67),(6,10.67)}. Relation 12.4 is then evaluated as

$$\begin{pmatrix} 1.2769 & 0 \\ 0 & 0.4489 \end{pmatrix} \leq \begin{pmatrix} 1 & 0 \\ 0 & 1 \end{pmatrix}.$$

Here, the statement for the background term is not true. In this example the errors for the observations were too small, but the contradiction is visible in the background term. This is due to the presence of two observations that forced the analysis away from the single background term. This example is plotted in Figure 12.1.

As the employed error covariance matrices are different from zero only for the main diagonal elements, it is sufficient to consider only the variances of the ImA covariance matrix. Therefore, for the a posteriori examination of the covariance matrices chosen for the CRISTA period, Relation 12.4 can be rewritten component-wise as

$$\mathbf{F} := \begin{pmatrix} \ddots & & & \\ & \frac{E((x^b_{ijkmt} - x^a_{ijkmt})^2)}{b_{ijkmt}} & & 0 \\ & & \ddots & \\ & 0 & & \frac{E((y^o_{ijkmt} - x^a_{ijkmt})^2)}{r_{ijkmt}} \\ & & & \ddots \end{pmatrix} \leq \mathbf{I}_{n+p} \ , \tag{12.5}$$

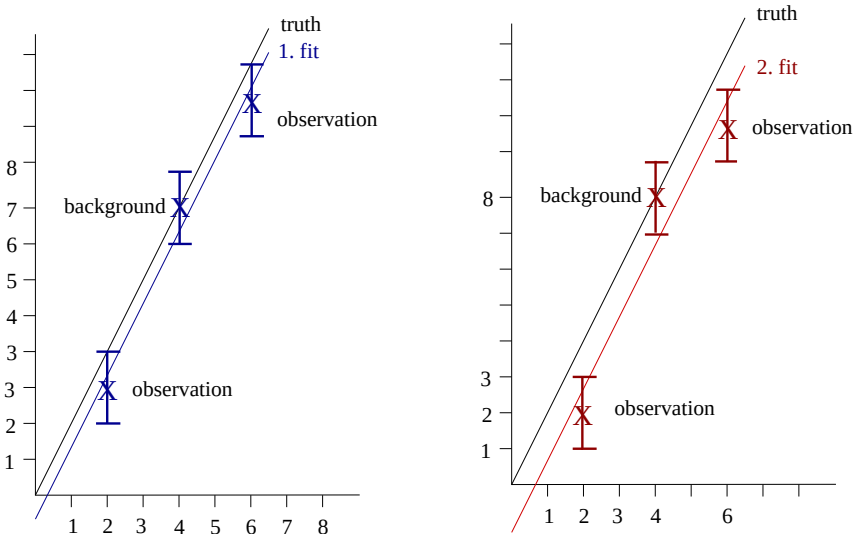

Figure 12.1: *Toy model plots illustrating the a posteriori error covariance matrices test described by Relation 12.4.*

where $t \in \{2, \cdots, 8\}$ are the start times of the assimilation periods, r_{ijkmt} is the observation error variance for gridpoint ijk at time t for species m, and b_{ijkmt} is the background error variance. If a sound statistical basis is given for the estimation and the system does not fulfill Relation 12.5, $\mathbf{B}$ or $\mathbf{R}$ are probably misspecified. This test allows the posteriori falsification of the employed error covariance matrices. To ensure a sound statistical basis, instead of comparing every entry of $\mathbf{x}^b - \mathbf{x}^a$ and $\mathbf{B}$ for the background term, we determined the average over all grid points and all days of the CRISTA period starting with the second day.

To this end, the average

$$\frac{\sum_{ijkt} \frac{(x^b_{ijkmt} - x^a_{ijkmt})^2}{b_{ijkmt}}}{M} \tag{12.6}$$

over all species was computed. In our case, b_{ijkmt} depends on the mixing ratio of species m at location ijk and time t as described in Chapter 11.3. M denotes the number of times $(x^b_{ijkmt} - x^a_{ijkmt})$ is evaluated.

For the measurements, the average

$$\frac{\sum_{\text{obs}} \frac{(y^\circ - x^a_{ijkmt})^2}{r_{ijkm}}}{N} \tag{12.7}$$

was calculated. Here, N is the total number of observations. We summed the contribution of all measurements during the CRISTA period. The measurement error variance r_{ijkm} depends on the latitude for ozone, for all other species it is constant.

day	5-6	6-7	7-8	8-9	9-10	10-11	11-12	average
Experiment CURV50								
meas.	0.703	0.978	0.293	0.210	0.748	0.850	0.878	0.709
bgr.	0.047	0.034	0.028	0.017	0.026	0.052	0.014	0.031
sum	0.750	1.012	0.321	0.227	0.774	0.902	0.892	0.740
Experiment CURV100								
meas.	0.678	0.883	0.245	0.153	0.781	0.948	0.813	0.689
bgr.	0.021	0.012	0.012	0.006	0.009	0.018	0.004	0.012
sum	0.699	0.895	0.257	0.159	0.790	0.966	0.817	0.701
Experiment AVER								
meas.	0.603	0.750	0.241	0.180	0.746	1.057	1.013	0.684
bgr.	0.015	0.007	0.011	0.007	0.014	0.009	0.002	0.009
sum	0.618	0.757	0.252	0.187	0.760	1.066	1.015	0.693

Table 12.2: *A posteriori evaluation of error covariance matrices: values of Terms 12.6 and 12.7 and their average over the episode for the three examined real case experiments. Days are given in days of the month of November.*

Table 12.2 displays the contribution to Equations 12.6 and 12.7 on each of the days of the assimilation experiment and the average over the episode. With the exception of experiment AVER on Nov. 10-11 and Nov. 11-12 and CURV50 on Nov. 6-7, all quotients are smaller than 1 and for the averages of each of the three experiments, the sum of the background and measurement contributions are smaller than 1. This shows that in general, the chosen error covariance matrices fulfill the necessary Criterion 12.4. As expected because of the smaller background error, the sum is larger for experiment CURV50 than for the other experiments. The small value of the background contribution is due to the fact that many of the species considered in the background term are coupled only weakly to the observed and therefore overdetermined species. This is clearly visible in Figure 12.2 which shows the contribution of the background term as a function of the species. The largest contributions stem from the observed species.

This test can be compared to the $p/2$ test described in Equation 12.2. The addends in Equations 12.6 and 12.7 are the addends of the cost function. If we define the norm

$$\|\mathbf{A}\| = \sum_{k=1}^{n} |a_{kk}|$$

for all diagonal matrices, then the norm of the matrix $\mathbf{F}$ defined in 12.5 is the trace of $\mathbf{F}$ and corresponds to $2\times\mathcal{J}_{\min}$. If the system is determined one-to-one, it is in principle capable of retrieving the corresponding state and thus reduce the cost function to zero. The one-to-one determination is

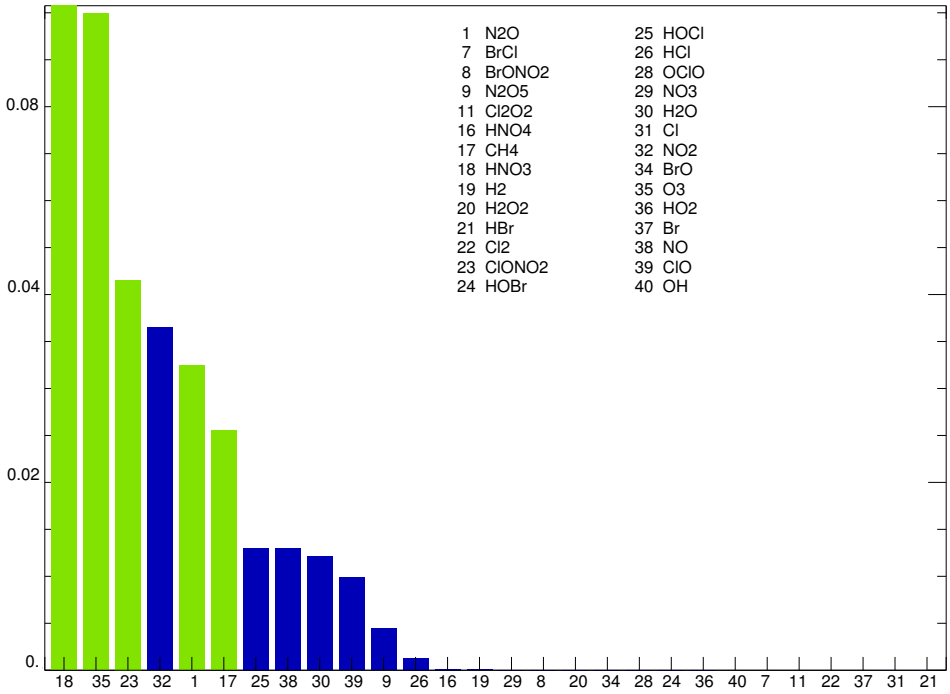

Figure 12.2: *Contributions to Equation 12.6 as a function of the species for experiment CURV50. Measured species are green/light gray and contribute the most.*

usually given by the background information. All additionally incorporated information, usually the observations, can be expected to be contradictory to the background as described by the error variances. Thus, $\|\mathbf{F}\|$ can be expected to be equal to p. This is illustrated by Equation 12.2.

If the statistical basis was insufficient for the above investigations, a similar approach could be used that can be employed for one single assimilation interval. Desroziers and Ivanov (2001) derived a perturbation technique that computes the expectation of sub-parts of the value of the cost function for given error covariance matrices based on Talagrand (1998).

CHAPTER 13

Summary and discussion of results

In the present work, a variational chemistry-transport model version of the Cologne model of the middle atmosphere was developed. It consists of the Eulerian Bott transport algorithm, a radiation module and a second order Rosenbrock chemistry solver coded by KPP. The horizontal grid resolution has been increased to 6818 grid boxes per layer to resolve fine-scale structures. The analyses of the UKMO for the UARS project extending to an altitude of 0.28 hPa are used for the wind- and temperature fields. This CTM forms the basis of the newly developed assimilation system AMMOC-CTM.

The properties of the assimilation system were investigated in identical twin experiments. In these experiments, the "measurements" are generated by the CTM. In this way, the truth is known and a choice can be made which information is provided to the assimilation system. We decided to carry out two experiments neglecting transport in order to identify the capacities of the assimilation system under different chemical regimes, in particular with respect to the polar night area. The significant reduction of the cost function by several orders of magnitude in the course of 60 iterations demonstrated the correct set-up of the assimilation system. Besides the CTM, it consists of the adjoint of the tangent-linearised version of the CTM and the L-BFGS minimization routine. In view of the chosen real case study of the CRISTA period in November 1994 we decided to compare the performance of the assimilation system given observations i) of all the species considered for minimization, and ii) only of those species measured by CRISTA (O_3, N_2O, HNO_3, $ClONO_2$ and CH_4). In this way, it was possible to determine which species can be corrected through CRISTA observations. Excluding the polar night area where mainly the measured species were corrected, we found that

CRISTA observations deliver good analyses for HNO_4 and NO_3 and help to correct $BrONO_2$, N_2O_5, H_2O_2, Cl_2, HOCl, H_2O, Cl, HO_2, ClO and OH. During daytime, improvement is additionally expected for Cl_2O_2, OClO and NO_2.

In the real case experiments it turned out to be essential to perform a four day spin-up integration to establish chemical equilibrium in the model before starting the assimilation process. Additional stabilising measures were needed to perform a sequence of experiments assimilating real CRISTA data. Without these measures, instabilities arose mostly close to the polar night terminator. Overall, the model was stable enough to allow for 24 hour assimilation periods, twice as long as in Errera and Fonteyn (2001).

One of the stabilising measures consists of a penalty term in the cost function which forces the newly proposed initial state to be smoother. This approach is mathematically consistent. It was motivated by the smoothness of the observations when interpolated on a 2° by 2° grid in contrast to less smooth analyses obtained without spreading the observation information to unobserved locations. The weights attached to the curvature penalty term were successively decreased so that the final analysis could capture all small-scale atmospheric structures. The superiority of the 4D var system over measurement interpolation was demonstrated by the analysis of chlorine nitrate that showed a significant diurnal variation.

A hallmark of the present work is the detailed and extensive a posteriori evaluation of the model performance. This analysis allows to check the consistency of the final result with the employed error assumptions. In this way, it was possible to verify that the analysis of the previous day is a suitable first guess with an error of the order of 50 %. Concerning the observations, the analyses agreed with them mostly within the assumed error bounds. As outlined in the chapter on the a posteriori examination, the reasons for the difference between an information source and the corresponding model state being larger than the assumed error can also be the misspecification of other pieces of information. Therefore, it is important to investigate the properties of the system as a whole. This consideration emphasizes the importance of an investigation of the background error as performed in this thesis. The analysis showed a visible dependence on the specification of the background error.

In a next step, it would be worthwhile to increase the vertical resolution and include vertical transport to obtain a fully three-dimensional model. Thereby, coupling of different layers, which is relevant on longer timescales, can be considered.

Another improvement will be the inclusion of heterogeneous chemistry. Küll et al. (2002) found that the effect of heterogeneous chemistry on N_2O_5 and NO_2 becomes important below about 20 hPa and is also evident in HNO_3.

Further validation of the assimilation results can be obtained by compar-

ison to ATMOS and HALOE measurements and the measurements carried out in the frame of the NDSC. Available NDSC data include mostly ozone, but sometimes also related species such as ClO vertical profiles.

After detailed validation, steps can be taken to speed up the calculations. This is needed to enable the use of the 3D model for near real time calculations. A significant speed-up of the system should be possible by increasing the minimum inner time step, which is presently 10 seconds, in the Rosenbrock solver. Further on, computing time could be saved during the adjoint chemistry calculations by using an interpolated value of the concentration at the inner time step of the Rosenbrock solver by interpolating between the concentrations at the points in time of the outer time step of four minutes which are presently saved on disk during the forward run. This would eliminate time-consuming recalculations of large parts of the forward chemistry module. The implied error should not hinder successful minimization.

Wahba and Wendelberger (1980) proposed a method to estimate the weighting matrix for the curvature penalty term, $\mathbf{A}^{-1}$ of Equation 7.1, from the data being analysed. It would be worthwhile to examine whether this estimation can be carried out in the context of chemical data assimilation.

In summary, we developed an adjoint CTM assimilation system that permits the routine assimilation of remote sounding data. Its capabilities were demonstrated in a (2+1) dimensional version by application to the CRISTA episode in November 1994. The inclusion of a curvature penalty term in the cost function allowed to stabilise the integration by forcing the model toward a smoothed initial state.

Bibliography

Arakawa, A. and Lamb, V. R., Computational design for the basic dynamical processes of UCLA general circulation model, in *General Circulation Models of the Atmosphere*, edited by B. Alder and J. Chang, vol. 17, pp. 174–264, Academic Press, New York, San Francisco, London, 1977.

Austin, J., Toward the Four Dimensional Assimilation of Stratospheric Chemical Constituents, *J. Geophys. Res.*, *97*, 2569–2588, 1992.

Bacmeister, J. T., Küll, V., Offermann, D., Riese, M., and Elkins, J. W., Intercomparison of satellite and aircraft observations of ozone, CFC-11 and NO_y using trajectory mapping, *J. Geophys. Res.*, *104*, 16,379–16,390, 1999.

Baier, F., *Entwicklung und Anwendung eines adjungierten Modells zur Simulation des Ozonhaushaltes der Stratosphäre während realer Episoden*, vol. 141, Mitteilungen aus dem Institut für Geophysik und Meteorologie der Universität zu Köln, Ph.D. dissertation, 2000.

Berger, U. and Ebel, A., Dependence of the energy budget at mesopause heights on variable circulation patterns, *Adv. Space Res.*, *17*, 111–116, 1996.

Bott, A., A positive definit advection scheme obtained by nonlinear renormalization of the advective fluxes, *Mon. Weather Rev.*, *117*, 1006–1015, 1989.

Bott, A., Monotone flux limitation in the area-preserving flux-form advection algorithm, *Mon. Weather Rev.*, *120*, 2592–2602, 1992.

Bouttier, F. and Courtier, P., Data assimilation concepts and methods, ECMWF Meteorological Training Course Lecture Series, 1999.

Brasseur, G., Orlando, J. J., and Tyndall, G. S., eds., *Atmospheric Chemistry and Global Change*, Oxford University Press, 1999.

Chao, W. C. and Chang, L.-P., Development of a Four-Dimensional Variational Analysis System Using the Adjoint Method at GLA Part I: Dynamics, *Mon. Weather Rev.*, *120*, 1661–1673, 1992.

Courtier, P., Dual formulation of four-dimensional variational assimilation, *Quart. J. Roy. Meteorol. Soc.*, *123*, 2449–2461, 1997.

Crowley, W. P., Numerical advection experiments, *Mon. Weather Rev.*, *96*, 1–11, 1968.

Daley, R., *Atmospheric data analysis*, Cambridge University Press, 1991.

Dameris, M., Berger, U., Günther, G., and Ebel, A., The ozone hole: dynamical consequences as simulated with a three-dimensional model of the middle atmosphere, *Ann. Geophys.*, *9*, 661–668, 1991.

Damian-Iordache, V., *KPP-Chemistry simulation development environment*, Master's thesis, University of Iowa, 1996.

DeMore, W. et al., Chemical Kinetics and Photochemical Data for Use in Stratospheric Modeling, Tech. Rep. 97-4, NASA, Jet Propulsion Laboratory, 1997.

Desroziers, G. and Ivanov, S., Diagnosis and adaptive tuning of observation-error parameters in a variational assimilation, *Quart. J. Roy. Meteorol. Soc.*, *127*, 1433–1452, 2001.

Ebel, A., Berger, U., and Krüger, B. C., Numerical Simulations with COMMA, a Global Model of the Middle Atmosphere, *SIMPO Newsletter*, *4*, 22–32, 1995.

Elbern, H. and Schmidt, H., A four–dimensional variational chemistry data assimilation scheme for Eulerian chemistry transport modeling, *J. Geophys. Res.*, *104*, 1999.

Elbern, H., Schmidt, H., and Ebel, A., Variational data assimilation for tropospheric chemistry modeling, *J. Geophys. Res.*, *D13*, 15,967–15,985, 1997.

Elbern, H., Schmidt, H., and Ebel, A., Improving chemical state analysis and ozone forecasts by four-dimensional chemistry data assimilation, in *Third WMO International Symposium on Assimilation of Observations in Meteorology and Oceanography*, 1999a.

Elbern, H., Schmidt, H., and Ebel, A., Parallel 4D-variational data assimilation for an eulerian chemistry transport model, in *Large-Scale Computations in Air Pollution Modelling*, edited by Z. Z. et al., pp. 151–160, Kluver Academic Publishers, 1999b.

Elbern, H., Schmidt, H., Talagrand, O., and Ebel, A., 4D–variational data assimilation with an adjoint air quality model for emission analysis, *Environmental Modelling and Software*, *15*, 539–548, 2000.

Engel, A., Strunk, M., Müller, M., Haase, H.-P., Poss, C., Levin, I., and Schmidt, U., Temporal development of total chlorine in the high-latitude stratosphere based on reference distributions of mean age derived from CO_2 and SF_6, *J. Geophys. Res.*, *107*, DOI 10.1029/2001JD000584, 2002.

Errera, Q. and Fonteyn, D., Four-dimensional variational chemical assimilation of CRISTA stratospheric measurements, *J. Geophys. Res.*, *106*, 12,253–12,265, 2001.

Farman, J. C., Gardiner, B. G., and Shanklin, J. D., Large losses of total ozone in Antarctica reveal seasonal ClO_x/NO_x interaction, *Nature*, *315*, 207–210, 1985.

Fisher, M. and Lary, D. J., Lagrangian four-dimensional variational data assimilation of chemical species, *Quart. J. Roy. Meteorol. Soc.*, *121*, 1681–1704, 1995.

Ghil, M. and Malanotte-Rizzoli, P., Data assimilation in meteorology and oceanography, *Adv. Geophys.*, *33*, 141–266, 1991.

Giering, R. and Kaminski, T., Recipes for adjoint code construction, *ACM Trans. Math. Software*, *24*, 437–474, 1998.

Gill, A. E., *Atmosphere-Ocean Dynamics*, vol. 30 of *International Geophysics Series*, Academic Press, Inc., 1982.

Grossmann, K. U., Recent Improvements in Middle Atmosphere Remote Sounding Techniques: The CRISTA-SPAS Experiment, in *Atmospheric Science Across the Stratopause*, vol. 123 of *Geophysical Monograph*, 2000.

Günther, G., *Die numerische Simulation von Transportprozessen in der mittleren Atmosphäre*, vol. 104, Mitteilungen aus dem Institut für Geophysik und Meteorologie der Universität zu Köln, Köln, Ph.D. dissertation, 1995.

Günther, G. and Dameris, M., Air mass exchange across the polar vortex edge during a simulated major stratospheric warming, *Ann. Geophys.*, *13*, 745–756, 1995.

Hendricks, J., Baier, F., Günther, G., Krüger, B., and Ebel, A., Stratospheric ozone depletion during the 1995-1996 Artic winter: 3-D simulations on the potential role of different PSC types, *Ann. Geophys.*, *19*, 1163–1181, 2001.

Hoelzemann, J. J., Elbern, H., and Ebel, A., PSAS and 4D–var Data Assimilation for Chemical Sstate analysis by Urban and Rural Observation Sites, *Physics and Chemistry of the Earth*, *26*, 807–812, 2001.

Ide, K., Courtier, P., Ghil, M., and Lorenc, A. C., Unified Notation for Data Assimilation: Operational, Sequential and Variational, *J. Meteorol. Soc. Japan*, *75*, 181–189, 1997.

Jakobs, H. J., *Untersuchungen von Schwerwelleneffekten mit Hilfe eines 3-D Zirkulationsmodells der mittleren Atmosphäre*, vol. 50, Mitteilungen aus dem Institut für Geophysik und Meteorologie der Universität zu Köln, Ph.D. dissertation, 1986.

Klinker, E., *Die numerische Simulation der nahezu zweijährigen Schwingung des mittleren Zonalwindes in der äquatorialen Stratosphäre*, Ph.D. dissertation, Freie Universität Berlin, 1981.

Klinker, E., Rabier, F., Kelly, G., and Mahfouf, J. F., The ECMWF operational implementation of four-dimensional variational assimilation. III: Experimental results and diagnostics with operational configuration, *Quart. J. Roy. Meteorol. Soc.*, *126*, 1191–1215, 2000.

Küll, V., *Dynamik und Photchemie in der Stratosphäre: Spurengasmessungen des CRISTA–Experiments*, Ph.D. dissertation, Bergische Universität–Gesamthochschule Wuppertal, 2002.

Küll, V., Riese, M., Tie, X., Wiemert, T., Eidmann, G., Offermann, D., and Brasseur, G. P., NO_y partitioning and aerosol influences in the stratosphere, *J. Geophys. Res.*, *107*, DOI 10.1029/2001JD001246, 2002.

LeDimet, F. X. and Talagrand, O., Variational algorithms for analysis and assimilation of meteorological observations: theoretical aspects, *Tellus*, *38A*, 97–110, 1986.

Lewis, J. M. and Derber, J. C., The use of adjoint equations to solve a variational adjustment problem with advective constraints, *Tellus*, *37*, 309–322, 1985.

Liu, D. C. and Nocedal, J., On the limited memory BFGS method for large scale optimization, *Mathematical Programming*, *45*, 503–528, 1989.

Mahfouf, J.-F. and Rabier, F., The ECMWF operational implementation of four-dimensional variational assimilation. II: Experimental results with improved physics, *Quart. J. Roy. Meteorol. Soc.*, *126*, 1171–1190, 2000.

Manney, G. L., Swinbank, R., and O'Neill, A., Stratospheric meteorological conditions for the 3-12 Nov 1994 ATMOS/ATLAS-3 measurements, *Geophys. Res. Lett.*, *23*, 2409–2412, 1996.

Manney, G. L., Michelsen, H. A., Bevilacqua, R. M., Gunson, M. R., Irion, F. W., Livesey, N. J., Oberheide, J., Riese, M., Russel III, J. M., Toon, G. C., and Zawodny, J. M., Comparison of satellite ozone observations in coincident air masses in early November 1994, *J. Geophys. Res.*, *106*, 9923–9943, 2001.

Nocedal, J., Updating Quasi-Newton Matrices With Limited Storage, *Mathematics of Computation*, *35*, 773–782, 1980.

Offermann, D., Grossmann, K.-U., Barthol, P., Knieling, P., Riese, M., and Trant, R., Cryogenic Infrared Spectrometers and Telescopes for the Atmosphere (CRISTA) experiment and middle atmosphere variability, *J. Geophys. Res.*, *104*, 16,311–16,325, 1999.

Rabier, F., Järvinen, H., Klinker, E., Mahfouf, J.-F., and Simmons, A., The ECMWF operational implementation of four-dimensional variational assimilation. I: Experimental results with simplified physics, *Quart. J. Roy. Meteorol. Soc.*, *126*, 1143–1170, 2000.

Reinsel, G. C., Trend analysis of upper stratospheric Umkehr ozone data for evidence of turnaround, *Geophys. Res. Lett.*, *29*, DOI 10.1029/2002GL014716, 2002.

Riese, M., *Remote Sensing and Modeling of the Earth's Middle Atmosphere: Results of the CRISTA Experiment*, Habilitationsschrift, Bergische Universität-Gesamthochschule Wuppertal, 2000.

Riese, M., Spang, R., Preusse, P., Ern, M., Jarisch, M., Offermann, D., and Grossmann, K. U., Cryogenic Infrared Spectrometers and Telescopes for the Atmosphere (CRISTA) data processing and atmospheric temperature and trace gas retrieval, *J. Geophys. Res.*, *104*, 16,349–16,367, 1999a.

Riese, M., Tie, X., Brasseur, G., and Offermann, D., Three-dimensional simulation of stratospheric trace gas distributions measured by CRISTA, *J. Geophys. Res.*, *104*, 16,419–16,435, 1999b.

Riese, M., Küll, V., Tie, X., Brasseur, G., Offermann, D., Lehmacher, G., and Franzen, A., Modeling of nitrogen species measured by CRISTA, *Geophys. Res. Lett.*, *27*, 2221–2224, 2000.

Riese, M., Franzen, A., Tie, X., and Offermann, D., Tracer structures in the southern hemispheric middle statosphere observed by CRISTA-1, *Adv. Space Res.*, *27*, 1623–1628, 2001.

Robinson, A. R., Lermusciaux, P. F. J., and Sloan III, N. Z., Data Assimilation, in *The Sea*, edited by K. H. Brink and A. R. Robinson, J. Wiley and Sons Inc., 1998.

Rose, K., On the Influence of Nonlinear Wave-Wave Interaction in a 3-d Primitive Equation Model for Sudden Stratospheric Warmings, *Beitr. Phys. Atmosph.*, *56*, 14–41, 1983.

Sandu, A., Daescu, D., and Carmichael, G. R., Direct and Adjoint Sensitivity Analysis of Chemical Kinetic Systems with KPP: I-Theory and Software Tools, Tech. Rep. CSTR-02-01, Michigan Technological University, 1400 Townsend Drive, Houghton, MI 49931, 2002.

Sirkes, Z. and Tziperman, E., Finite Difference of Adjoint or Adjoint of Finite Difference?, *Mon. Weather Rev.*, *125*, 3373–3378, 1997.

Smith, A. K. and Riese, M., Cryogenic Infrared Spectrometers and Telescopes for the Atmosphere (CRISTA) observations of tracer transport by inertially unstable circulations, *J. Geophys. Res.*, *104*, 1999.

Smyshlyaev, S. P. and Geller, M. A., Analysis of SAGE II observations using data assimilation by the SUNY-SPB two-dimensional model and comparison to TOMS data, *J. Geophys. Res.*, *106*, 32,327–32,335, 2001.

Solomon, S., Stratospheric ozone depletion: A review of concepts and history, *Rev. Geophys.*, *37*, 275–316, 1999.

Spang, R., Riese, M., and Offermann, D., CFC11 measurements by CRISTA, *Adv. Space Res.*, *19*, 575–578, 1997.

Stoer, J., *Numerische Mathematik I*, Springer, 1994.

Swinbank, R. and O'Neill, A., A Stratosphere-Troposphere Data Assimilation System, *Mon. Weather Rev.*, *122*, 686–702, 1994.

Talagrand, O., The use of Adjoint Equations in Numerical Modelling of the Atmospheric Circulation, in *Proceedings of Workshop on Automatic Differentiation of Algorithms: Theory, Implementation and Application*, edited by A. Griewank and G. G. Corliss, Society for Industrial and Applied Mathematics, 1991.

Talagrand, O., Assimilation of Observations, an Introduction, *J. Meteorol. Soc. Japan*, *75*, 191–209, 1997.

Talagrand, O., A posteriori evaluation and verification of analysis and assimilation algorithms, in *Workshop on Diagnosis of Data Assimilation Systems*, European Centre for Medium-range Weather Forecasts Reading, England, 2-4 November, 1998.

Talagrand, O. and Courtier, P., Variational assimilation of meteorological observations with the adjoint vorticity equation. I: Theory, *Quart. J. Roy. Meteorol. Soc.*, *113*, 1311–1328, 1987.

Todling, R., Estimation Theory and Foundations of Atmospheric Data Assimilation, DAO Office Note 1999-01, 1999.

van Loon, M., Builtjes, P. J. H., and Segers, A. J., Data assimilation of ozone in the atmospheric transport chemistry model LOTOS, *Environ. Modell. Software.*, *15*, 603–609, 2000.

Wahba, G. and Wendelberger, J., Some New Mathematical Method for Variational Objective Analysis Using Splines and Cross Validation, *Mon. Weather Rev.*, *108*, 1122–1143, 1980.

Waibel, A. E., Peter, T., Carslaw, K. S., Oelhaf, H., Wetzel, G., Crutzen, P. J., Pöschl, U., Tsias, A., Reimer, E., and Fischer, H., Arctic ozone loss due to denitrification, *Science*, *283*, 2064–2069, 1999.

Weatherhead, E. C., Reinsel, G. C., Tiao, G. C., Jackman, C. H., Bishop, L., Hollandsworth Frith, S. M., DeLuisi, J., Keller, T., Oltmans, S. J., Fleming, E. L., Wuebbles, D. J., Kerr, J. B., Miller, A. J., Herman, J., McPeters, R., Nagatani, R. M., and Frederick, J. E., Detecting the recovery of total column ozone, *J. Geophys. Res.*, *105*, 22,201–22,210, 2000.

World Meteorological Organization, Scientific assessment of ozone depletion: 1998, Tech. Rep. 44, WMO, 1999.

Zhang, S., Zou, X., Ahlquist, J., Navon, I. M., and Sela, J. G., Use of Differentiable and Nondifferentiable Optimization Algorithms for Variational Data Assimilation with Discontinuous Cost Functions, *Mon. Weather Rev.*, *128*, 4031–4044, 2000.

Zou, X., Navon, I. M., Berger, M., Phua, P. K. H., Schlick, T., and LeDimet, F. X., Numerical experience with limited-memory quasi-Newton and truncated-Newton methods, *SIAM J. Optim.*, *3*, 582–608, 1993.

Zou, X., Vandenberghe, F., Pondeca, M., and Kuo, Y.-H., Introduction to adjoint techniques and the MM5 adjoint modelling system, Tech. Rep. NCAR/TN-435-STR, NCAR, 1997.

APPENDIX A

Reactions in the AMMOC-CTM

Table A.1: *Photolysis reactions included in the AMMOC-CTM*

Reaction	
(J1)	$O_2 + h\nu \rightarrow 2O(^3P)$
(J2)	$O_3 + h\nu \rightarrow O(^3P) + O_2$
(J3)	$O_3 + h\nu \rightarrow O(^1D) + O_2$
(J4)	$HO_2 + h\nu \rightarrow O(^3P) + OH$
(J5)	$H_2O + h\nu \rightarrow H + OH$
(J6)	$H_2O_2 + h\nu \rightarrow 2OH$
(J7)	$NO_2 + h\nu \rightarrow O(^3P) + NO$
(J8)	$NO_3 + h\nu \rightarrow NO_2 + O(^3P)$
(J9)	$NO_3 + h\nu \rightarrow NO + O_2$
(J10)	$N_2O + h\nu \rightarrow N_2 + O(^1D)$
(J11)	$N_2O_5 + h\nu \rightarrow NO_2 + NO_3$
(J12)	$HNO_3 + h\nu \rightarrow OH + NO_2$
(J13)	$HNO_4 + h\nu \rightarrow HO_2 + NO_2$
(J14)	$Cl_2O_2 + h\nu\ (+ M) \rightarrow 2Cl + O_2\ (+ M)$
(J15)	$Cl_2 + h\nu \rightarrow 2Cl$
(J16)	$OClO + h\nu \rightarrow O(^3P) + ClO$
(J17)	$HCl + h\nu \rightarrow Cl + H$
(J18)	$HOCl + h\nu \rightarrow Cl + OH$
(J19)	$ClONO_2 + h\nu \rightarrow Cl + NO_3$
(J20)	$CH_3Cl + h\nu \rightarrow Cl + \text{products}$
(J21)	$CCl_4 + h\nu \rightarrow 4Cl + \text{products}$
(J22)	$CFCl_3 + h\nu \rightarrow 3Cl + \text{products}$
(J23)	$CF_2Cl_2 + h\nu \rightarrow 2Cl + \text{products}$
(J24)	$CHF_2Cl + h\nu \rightarrow Cl + \text{products}$
(J25)	$CF_2ClCFCl_2 + h\nu \rightarrow 3Cl + \text{products}$
(J26)	$CH_3CCl_3 + h\nu \rightarrow 3Cl + \text{products}$
(J27)	$BrO + h\nu \rightarrow Br + O(^3P)$
(J28)	$BrCl + h\nu \rightarrow Br + Cl$
(J29)	$HBr + h\nu \rightarrow Br + H$
(J30)	$HOBr + h\nu \rightarrow Br + OH$
(J31)	$BrONO_2 + h\nu \rightarrow Br + NO_3$
(J32)	$CH_3Br + h\nu \rightarrow Br + \text{products}$
(J33)	$CF_2ClBr + h\nu \rightarrow Cl + Br + \text{products}$
(J34)	$CF_3Br + h\nu \rightarrow Br + \text{products}$

The term "products" represents constituents which are not considered in the present study.

Table A.2: *Gas phase reactions included in the AMMOC-CTM. Rate constants for first- and second-order reactions are given in units of* s^{-1} *and* $molecules^{-1}cm^3s^{-1}$*, respectively. Rate constants for third-order reactions are given as effective second-order rate constants in units of* $molecules^{-1}cm^3s^{-1}$

Reaction		Rate constant
(R1)	$O(^1D) + N_2 \rightarrow O(^3P) + N_2$	$1.8\times10^{-11}\exp(110/T)$
(R2)	$O(^1D) + O_2 \rightarrow O(^3P) + O_2$	$3.2\times10^{-11}\exp(70/T)$
(R3)	$O(^1D) + O_3 \rightarrow 2O_2$	1.2×10^{-10}
(R4)	$O(^3P) + O(^3P) + M \rightarrow O_2 + M$	$4.7\times10^{-33}[M](T/300.)^{-2.0}$
(R5)	$O(^3P) + O_2 + M \rightarrow O_3 + M$	$6.0\times10^{-34}[M](T/300.)^{-2.3}$
(R6)	$O(^3P) + O_3 \rightarrow 2O_2$	$8.0\times10^{-12}\exp(-2060/T)$
(R7)	$O(^1D) + H_2O \rightarrow 2OH$	2.2×10^{-10}
(R8)	$O(^1D) + H_2 \rightarrow OH + H$	1.1×10^{-10}
(R9)	$H + O_3 \rightarrow OH + O_2$	$1.4\times10^{-10}\exp(-470/T)$
(R10)	$H + O_2 + M \rightarrow HO_2 + M$	$f(k_0,k_\infty)$, k_0=$5.7\times10^{-32}(T/300)^{-1.6}$, k_∞=7.5×10^{-11}
(R11)	$H + HO_2 \rightarrow 2OH$	7.3×10^{-11}
(R12)	$OH + O(^3P) \rightarrow H + O_2$	$2.2\times10^{-11}\exp(120/T)$
(R13)	$OH + OH \rightarrow H_2O + O(^3P)$	$4.2\times10^{-12}\exp(-240/T)$
(R14)	$OH + OH + M \rightarrow H_2O_2 + M$	$f(k_0,k_\infty)$, k_0=$6.2\times10^{-31}(T/300)^{-1.0}$, k_∞=2.6×10^{-11}
(R15)	$OH + H_2O_2 \rightarrow H_2O + HO_2$	$2.9\times10^{-12}\exp(-160/T)$
(R16)	$OH + H_2 \rightarrow H_2O + H$	$5.5\times10^{-12}\exp(-2000/T)$
(R17)	$OH + O_3 \rightarrow HO_2 + O_2$	$1.6\times10^{-12}\exp(-940/T)$
(R18)	$OH + HO_2 \rightarrow H_2O + O_2$	$4.8\times10^{-11}\exp(250/T)$
(R19)	$HO_2 + O(^3P) \rightarrow OH + O_2$	$3.0\times10^{-11}\exp(200/T)$
(R20)	$HO_2 + O_3 \rightarrow OH + 2O_2$	$1.1\times10^{-14}\exp(-500/T)$
(R21)	$HO_2 + HO_2 \rightarrow H_2O_2 + O_2$	$2.3\times10^{-13}\exp(600/T)$
(R22)	$HO_2 + HO_2 + M \rightarrow H_2O_2 + O_2 + M$	$1.7\times10^{-33}[M]\exp(1000./T)$
(R23)	$H_2O_2 + O(^3P) \rightarrow HO_2 + OH$	$1.4\times10^{-12}\exp(-2000/T)$
(R24)	$CH_4 + OH \rightarrow H_2O +$ products	$2.65\times10^{-12}\exp(-1800/T)$
(R25)	$CH_4 + O(^1D) \rightarrow OH +$ products	1.125×10^{-10}
(R26)	$N_2O + O(^1D) \rightarrow N_2 + O_2$	4.9×10^{-11}
(R27)	$N_2O + O(^1D) \rightarrow 2NO$	6.7×10^{-11}
(R28)	$N_2 + O(^1D) + M \rightarrow N_2O + M$	$3.5\times10^{-37}[M](T/300.)^{-0.6}$
(R29)	$NO + O_3 \rightarrow NO_2 + O_2$	$2.0\times10^{-12}\exp(-1400/T)$
(R30)	$NO + O(^3P) + M \rightarrow NO_2 + M$	$f(k_0,k_\infty)$, k_0=$9.0\times10^{-32}(T/300)^{-1.5}$, k_∞=3.0×10^{-11}
(R31)	$NO + HO_2 \rightarrow OH + NO_2$	$3.5\times10^{-12}\exp(250/T)$
(R32)	$NO + NO_3 \rightarrow 2NO_2$	$1.5\times10^{-11}\exp(170/T)$
(R33)	$NO_2 + O(^3P) \rightarrow NO + O_2$	$6.5\times10^{-12}\exp(120/T)$
(R34)	$NO_2 + O(^3P) + M \rightarrow NO_3 + M$	$f(k_0,k_\infty)$, k_0=$9.0\times10^{-32}(T/300)^{-2.0}$, k_∞=2.2×10^{-11}
(R35)	$NO_2 + O_3 \rightarrow NO_3 + O_2$	$1.2\times10^{-13}\exp(-2450/T)$
(R36)	$NO_2 + H \rightarrow OH + NO$	$4.0\times10^{-10}\exp(-340/T)$
(R37)	$NO_2 + OH + M \rightarrow HNO_3 + M$	$f(k_0,k_\infty)$, k_0=$2.5\times10^{-30}(T/300)^{-4.4}$, k_∞=$1.6\times10^{-11}(T/300)^{-1.7}$
(R38)	$NO_2 + HO_2 + M \rightarrow HNO_4 + M$	$f(k_0,k_\infty)$, k_0=$1.8\times10^{-31}(T/300)^{-3.2}$, k_∞=$4.7\times10^{-12}(T/300)^{-1.4}$
(R39)	$HNO_4 + M \rightarrow HO_2 + NO_2 + M$	$k_{R38}/(2.1\times10^{-27}\exp(10900/T))$

Table A.2: *(continued)*

Reaction		Rate constant
(R40)	$NO_2 + NO_3 + M \rightarrow N_2O_5 + M$	$f(k_0, k_\infty)$, k_0=$2.2\times10^{-30}(T/300)^{-3.9}$, k_∞=$1.5\times10^{-12}(T/300)^{-0.7}$
(R41)	$N_2O_5 + M \rightarrow NO_3 + NO_2 + M$	$k_{R40}/(2.7\times10^{-27}\exp(11000/T))$
(R42)	$NO_3 + O(^3P) \rightarrow NO_2 + O_2$	1.0×10^{-11}
(R43)	$NO_3 + OH \rightarrow NO_2 + HO_2$	2.2×10^{-11}
(R44)	$NO_3 + HO_2 \rightarrow HNO_3 + O_2$	1.5×10^{-12}
(R45)	$HNO_3 + OH \rightarrow NO_3 + H_2O$	$k_1+k_2/(1+k_2/k_3)$, k_1=$7.2\times10^{-15}\exp(785./T)$, k_2=1.9×10^{-33}[M]$\exp(725./T)$, k_3=$4.1\times10^{-16}\exp(1440./T)$
(R46)	$HNO_4 + OH \rightarrow NO_2 + H_2O + O_2$	$1.3\times10^{-12}\exp(380/T)$
(R47)	$Cl + O_3 \rightarrow ClO + O_2$	$2.9\times10^{-11}\exp(-260/T)$
(R48)	$Cl + OH \rightarrow HCl + O(^3P)$	$9.8\times10^{-12}\exp(-2860/T)$
(R49)	$Cl + HO_2 \rightarrow HCl + O_2$	$1.8\times10^{-11}\exp(170/T)$
(R50)	$Cl + HO_2 \rightarrow OH + ClO$	$4.1\times10^{-11}\exp(-450/T)$
(R51)	$Cl + H_2 \rightarrow HCl + H$	$3.7\times10^{-11}\exp(-2300/T)$
(R52)	$Cl + CH_4 \rightarrow HCl +$ products	$1.1\times10^{-11}\exp(-1400/T)$
(R53)	$Cl + H_2O_2 \rightarrow HCl + HO_2$	$1.1\times10^{-11}\exp(-980/T)$
(R54)	$Cl + H_2O \rightarrow HCl + OH$	$2.79\times10^{-11}\exp(-8670/T)$
(R55)	$Cl + NO_3 \rightarrow ClO + NO_2$	2.4×10^{-11}
(R56)	$Cl + Cl + M \rightarrow Cl_2 + M$	6.14×10^{-34}[M]$\exp(906/T)$
(R57)	$Cl + OClO \rightarrow 2ClO$	$3.4\times10^{-11}\exp(160/T)$
(R58)	$Cl + HOCl \rightarrow Cl_2 + OH$	$6.0\times10^{-13}\exp(-130/T)$
(R59)	$Cl + Cl_2O_2 \rightarrow Cl + Cl_2 + O_2$	1.0×10^{-10}
(R60)	$Cl + ClONO_2 \rightarrow Cl_2 + NO_3$	$6.5\times10^{-12}\exp(135/T)$
(R61)	$ClO + O(^3P) \rightarrow Cl + O_2$	$3.0\times10^{-11}\exp(70/T)$
(R62)	$ClO + OH \rightarrow Cl + HO_2$	$1.1\times10^{-11}\exp(120/T)$
(R63)	$ClO + HO_2 \rightarrow HOCl + O_2$	$4.8\times10^{-13}\exp(700/T)$
(R64)	$ClO + NO \rightarrow Cl + NO_2$	$6.4\times10^{-12}\exp(290/T)$
(R65)	$ClO + NO_2 + M \rightarrow ClONO_2 + M$	$f(k_0, k_\infty)$, k_0=$1.8\times10^{-31}(T/300)^{-3.4}$, k_∞=$1.5\times10^{-11}(T/300)^{-1.9}$
(R66)	$ClO + NO_3 \rightarrow Cl + NO_2 + O_2$	4.7×10^{-13}
(R67)	$ClO + ClO + M \rightarrow Cl_2O_2 + M$	$f(k_0, k_\infty)$, k_0=$2.2\times10^{-32}(T/300)^{-3.1}$, k_∞=$3.5\times10^{-12}(T/300)^{-1.0}$
(R68)	$Cl_2O_2 + M \rightarrow 2ClO + M$	$k_{R67}/(1.3\times10^{-27}\exp(8744/T))$
(R69)	$OClO + O(^3P) \rightarrow ClO + O_2$	$2.4\times10^{-12}\exp(-960/T)$
(R70)	$OClO + OH \rightarrow HOCl + O_2$	$4.5\times10^{-13}\exp(800/T)$
(R71)	$OClO + NO \rightarrow ClO + NO_2$	$2.5\times10^{-12}\exp(-600/T)$
(R72)	$Cl_2 + M \rightarrow 2Cl + M$	$\exp(\ln(3.85\times10^{-11}[M])$ - $23630/T)$
(R73)	$Cl_2 + O(^1D) \rightarrow ClO + Cl$	2.8×10^{-10} (25% quenching)
(R74)	$Cl_2 + OH \rightarrow HOCl + Cl$	$1.4\times10^{-12}\exp(-900/T)$
(R75)	$HCl + O(^1D) \rightarrow OH + Cl$	1.0×10^{-10}
(R76)	$HCl + O(^1D) \rightarrow H + ClO$	3.6×10^{-11}
(R77)	$HCl + O(^3P) \rightarrow Cl + OH$	$1.0\times10^{-11}\exp(-3300/T)$

Table A.2: *(continued)*

Reaction		Rate constant
(R78)	$HCl + OH \rightarrow Cl + H_2O$	$2.6\times10^{-12}\exp(-350/T)$
(R79)	$HOCl + O(^3P) \rightarrow ClO + OH$	$1.0\times10^{-11}\exp(-1300/T)$
(R80)	$HOCl + OH \rightarrow ClO + H_2O$	$3.0\times10^{-12}\exp(-500/T)$
(R81)	$ClONO_2 + O(^3P) \rightarrow ClO + NO_3$	$2.9\times10^{-12}\exp(-800/T)$
(R82)	$ClONO_2 + OH \rightarrow HOCl + NO_3$	$1.2\times10^{-12}\exp(-330/T)$
(R83)	$CH_3Cl + O(^1D) \rightarrow ClO + products$	4.0×10^{-10}
(R84)	$CH_3Cl + OH \rightarrow H_2O + products$	$4.0\times10^{-12}\exp(-1400/T)$
(R85)	$CCl_4 + O(^1D) \rightarrow ClO + products$	3.3×10^{-10} (14% quenching)
(R86)	$CFCl_3 + O(^1D) \rightarrow ClO + products$	2.3×10^{-10} (40% quenching)
(R87)	$CF_2Cl_2 + O(^1D) \rightarrow ClO + products$	1.4×10^{-10} (14% quenching)
(R88)	$CHF_2Cl + O(^1D) \rightarrow ClO + products$	1.0×10^{-10} (28% quenching)
(R89)	$CHF_2Cl + OH \rightarrow H_2O + products$	$1.0\times10^{-12}\exp(-1600/T)$
(R90)	$CF_2ClCFCl_2 + O(^1D) \rightarrow ClO + products$	2.0×10^{-10}
(R91)	$CH_3CCl_3 + O(^1D) \rightarrow ClO + products$	4.0×10^{-10}
(R92)	$CH_3CCl_3 + OH \rightarrow H_2O + products$	$1.8\times10^{-12}\exp(-1550/T)$
(R93)	$Br + O_3 \rightarrow BrO + O_2$	$1.7\times10^{-11}\exp(-800/T)$
(R94)	$Br + HO_2 \rightarrow HBr + O_2$	$1.5\times10^{-11}\exp(-600/T)$
(R95)	$Br + OClO \rightarrow BrO + ClO$	$2.6\times10^{-11}\exp(-1300/T)$
(R96)	$BrO + O(^3P) \rightarrow Br + O_2$	$1.9\times10^{-11}\exp(230/T)$
(R97)	$BrO + OH \rightarrow Br + HO_2$	7.5×10^{-11}
(R98)	$BrO + HO_2 \rightarrow HOBr + O_2$	$3.4\times10^{-12}\exp(540/T)$
(R99)	$BrO + NO \rightarrow Br + NO_2$	$8.8\times10^{-12}\exp(260/T)$
(R100)	$BrO + NO_2 + M \rightarrow BrONO_2 + M$	$f(k_0, k_\infty)$, k_0=$5.2\times10^{-31}(T/300)^{-3.2}$, k_∞=$6.9\times10^{-12}(T/300)^{-2.9}$
(R101)	$BrO + ClO \rightarrow Br + OClO$	$1.6\times10^{-12}\exp(430/T)$
(R102)	$BrO + ClO$ (+M) $\rightarrow Br + Cl + O_2$ (+M)	$2.9\times10^{-12}\exp(220/T)$
(R103)	$BrO + ClO \rightarrow BrCl + O_2$	$5.8\times10^{-13}\exp(170/T)$
(R104)	$BrO + BrO \rightarrow 2Br + O_2$	$1.5\times10^{-12}\exp(230/T)$
(R105)	$HBr + O(^1D) \rightarrow OH + Br$	1.5×10^{-10} (20% quenching)
(R106)	$HBr + O(^3P) \rightarrow Br + OH$	$5.8\times10^{-12}\exp(-1500/T)$
(R107)	$HBr + OH \rightarrow Br + H_2O$	1.1×10^{-11}
(R108)	$HOBr + O(^3P) \rightarrow OH + BrO$	$1.2\times10^{-10}\exp(-430/T)$
(R109)	$HOBr + OH \rightarrow H_2O + BrO$	1.1×10^{-12}
(R110)	$HOBr + Cl \rightarrow HCl + BrO$	1.1×10^{-10}
(R111)	$CH_3Br + O(^1D) \rightarrow BrO + products$	1.8×10^{-10}
(R112)	$CH_3Br + OH \rightarrow H_2O + products$	$4.0\times10^{-12}\exp(-1470/T)$
(R113)	$CF_2ClBr + O(^1D) \rightarrow BrO + products$	1.5×10^{-10} (36% quenching)
(R114)	$CF_3Br + O(^1D) \rightarrow BrO + products$	1.0×10^{-10} (59% quenching)

$M \in \{N_2, O_2\}$. For third-order reactions, $f(k_0, k_\infty)$ has to be evaluated according to DeMore et al. (1997):
$f(k_0, k_\infty)$=$(k_0[M]/(1+k_0[M]/k_\infty))\times0.6^{(1+(\log_{10}(k_0[M]/k_\infty))^2)^{-1}}$. The term "products" represents constituents which are not considered in the present study.

APPENDIX B

AMMOC-CTM flow chart

Figure B.1 shows the routines of the AMMOC-CTM. Each called routine (right) is listed only once per calling routine (left). The main tasks for each routine are listed in Table B.1

routine name	task
adicht	temperature interpolation and density
advec4	vertical advection
advec4m	meridional advection
advec4z	zonal advection
advec4mzvcl	adjoint vertical advection
advec4mmzvcl	adjoint meridional advection
advec4zmzvcl	adjoint zonal advection
an1int	reading of wind and temperature fields
bgforc	background contribution to adjoint variables and cost function
couran	Courant number
cristawght	weights for CRISTA real case experiments
daxpy	constant times a vector plus a vector, from linpack
decomp	matrix LR decomposition
decompcl	adjoint of matrix decomposition
dochem	chemistry
dochemcl	adjoint chemistry
forcing	measurement contribution to adjoint variables and cost function
f_var	calculates aggregate term, subroutine of ros2 generated by KPP
f_varcl	adjoint of f_var

Table B.1: *Routine names and tasks in the AMMOC-CTM.*

routine name	task
initqmix	initialization mixing ratio field
init_chem	setup for chemistry
init_interp	reading lookup-table for interp
init_main	setup of model grid and constants
integrate_ppb	integrator for box model (second order Rosenbrock)
integrate_ppbcl	adjoint of integrate_ppb
interp	photolysis rates
inter_01	interpolation of wind fields
itwght	weights for IT experiments
jacvar_sp	jacobian of concentrations, subroutine of ros2 generated by KPP
jacvar_spcl	adjoint of jacvar_sp
lbfgs	minimization
lb1	print of monitoring information
mcsrch	line search
mcstep	steplength for mcsrch
mindrv	setup for minimization
open_main	input/output
phot	photolysis rates
ros2	time integration of differential equations describing chemical reactions
ros2v2bcl	adjoint of ros2
setgeo	geometric constants
shift13	shift from 1D to 3D array after minimization
shift31	shift from 3D to 1D array for minimization
smoforc	curvature contribution to cost function
solve	new concentrations, subroutine of ros2 generated by KPP
solvecl	adjoint of solve
transn	transport
transnmzvcl	adjoint transport
update_rconst	reaction rates
vbew	vertical Courant numbers
vorwaerts	forward model
zenit	calculation of zenit angle

Table B.1: *(continued)*

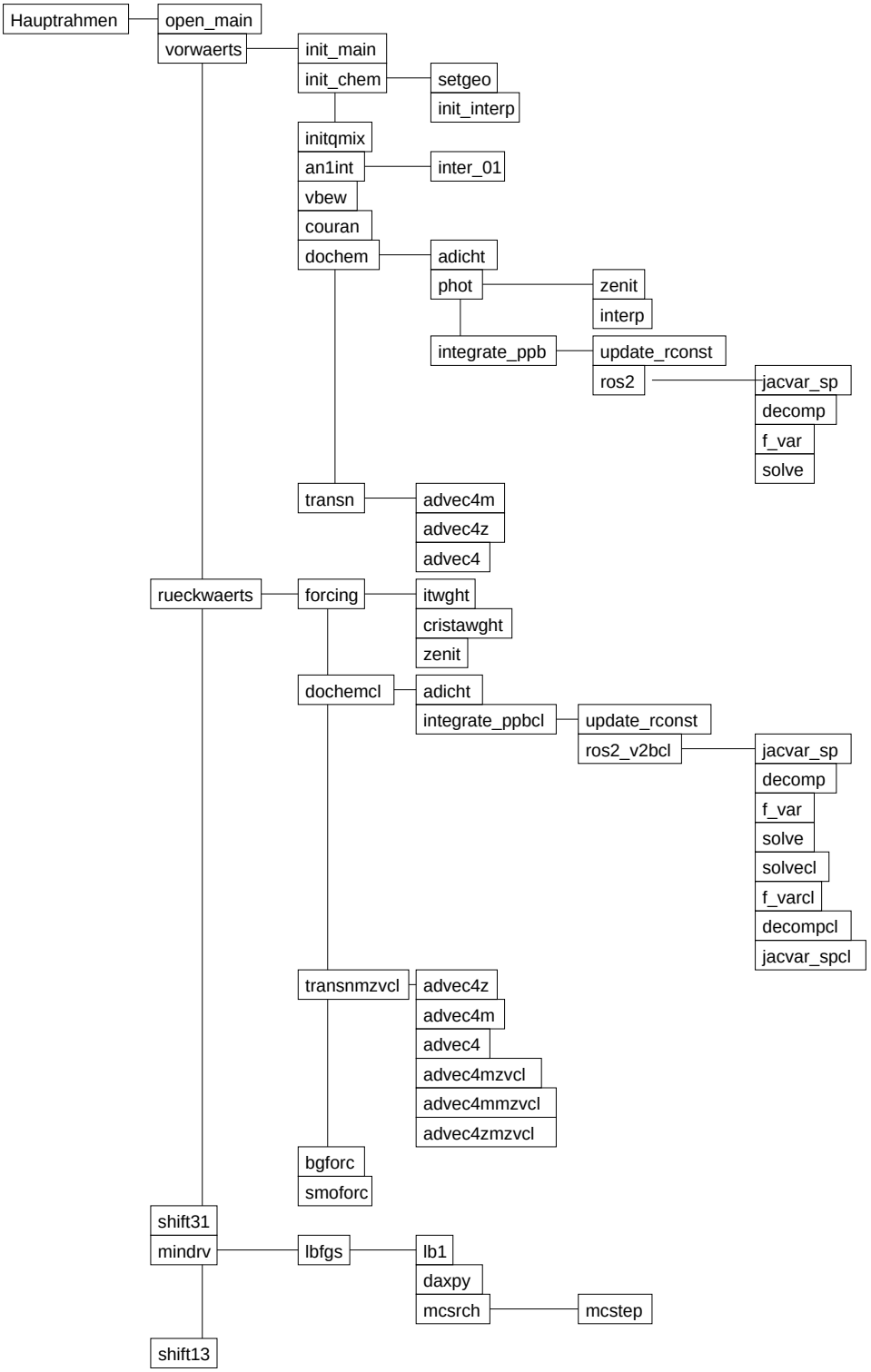

Figure B.1: *Flow chart of the AMMOC-CTM.*

APPENDIX C

CRISTA measurement resolution

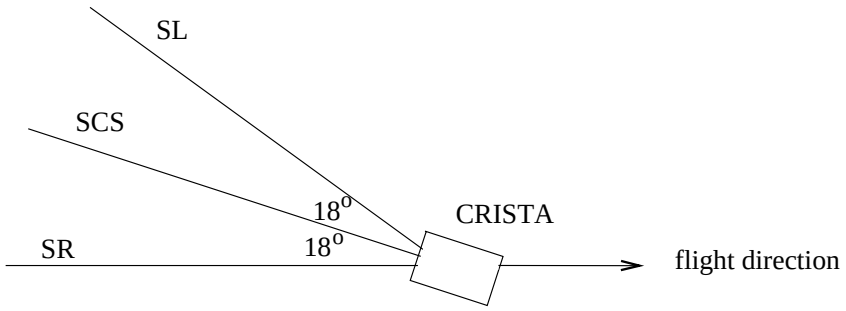

Figure C.1: *Flight direction of the CRISTA instrument and positions of the three telescopes SR, SCS and SL.*

During the first campaign in October 1994, the CRISTA instrument flew in an orbit with 57° inclination. The spectrometer SR faced in the opposite direction of the flight direction, while the spectrometer SCS and SL were facing into the direction 18° and 36°, respectively, to the right. This is illustrated in Figure C.1. Assuming that the size of the sampled air mass is given as 200km×20km (along track × across track), as described in Grossmann (2000), the zonal and meridional components can be calculated. The length of the sampled air mass in zonal direction is given by $a + a' = 200km|\cos(\beta - \alpha)| + 20km|\sin(\beta - \alpha)|$, in meridional direction by $b+b' = 200km|\sin(\beta-\alpha)|+20km|\cos(\beta-\alpha)|$ (see Figure C.2 for definition). α and β are given for the position of the CRISTA-SPAS. The footprint of the sampled air mass is situated approximately 1000 km in the direction of the line of sight. The size of the footprint is shown in Table C.1 in comparison to the AMMOC-CTM resolution at the latitude of the footprint.

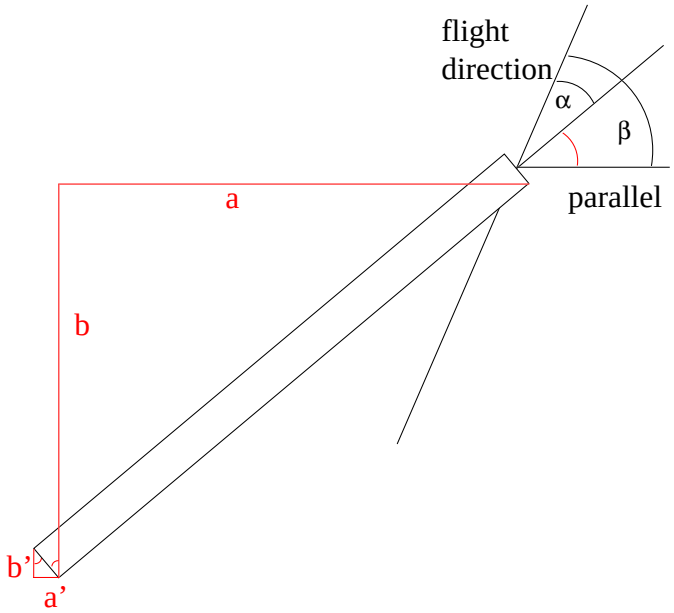

Figure C.2: *Definition of angles and lines for the calculation of the meridional and zonal length of CRISTA sampled air mass. The rectangle represents the sampled air mass of 200×20 km^2. α denotes the angle between the flight direction and the spectrometer, β denotes the angle between the flight direction and the latitudinal circle. a and a' add up to the zonal length, b and b' to the meridional length.*

		SR	**CTM**	**SCS**	**CTM**	**SL**	**CTM**
	α	0°		18°		36°	
turning point	γ	62°		65°		67°	
north	zonal	200	196	196	177	174	163
β =0°	mer.	20	278	81	278	134	278
turning point	γ	62°		59°		57°	
south	zonal	200	196	196	215	174	227
β =0°	mer.	20	278	81	278	134	278
equator	γ	8°		6°		3°	
ascending	zonal	125	413	168	415	194	416
β =57°	mer.	178	278	141	278	90	278
equator	γ	8°		9°		9°	
descending	zonal	125	413	71	417	30	417
β =57°	mer.	178	278	198	278	201	278

Table C.1: *Length [km] of sampled air mass in zonal and meridional direction for CRISTA telescopes SR, SCS and SL and resolution of the AMMOC-CTM. γ is the latitude of the footprint of the sampled air mass.*

Zusammenfassung

Kurz nach Entdeckung der Ozonschicht wurde die Fähigkeit der mittleren Atmosphäre erkannt, schädliche ultraviolette (UV) Strahlung zu filtern. Eine wichtige Konsequenz der UV Absorption durch die Ozonschicht ist eine Temperaturzunahme in der Stratosphäre bis zur Stratopause in etwa 50 km Höhe. Oberhalb der Ozonschicht, in der Mesosphäre, beobachtet man eine charakteristische Temperaturabnahme als Folge von dynamischen und von Strahlungseffekten. Die stratosphärische Temperaturzunahme aufgrund der Ozonschicht unterdrückt Vertikalbewegungen. Dies zeigt, dass die Ozonschicht deutlichen Einfluss auf die Dynamik der Atmosphäre hat. Daher muss ihre Entwicklung auch für Studien über Klimaveränderungen berücksichtigt werden. 1985 publizierten Farman et al. die Beobachtung einer drastischen Abnahme der Ozonkonzentration am Südpol zu Beginn des Frühlings, diese ist mittlererweile unter dem Begriff "Ozonloch" allgemein bekannt. Erhöhte atmosphärische Chlorkonzentrationen wurden als Ursache vermutet und bestätigt. Diese drastische Abnahme oder sogar ein vollständiger Abbau von Ozon wurde in Höhen beobachtet, in denen die Ozonkonzentration normalerweise maximal ist. Aufgrund dieser Entdeckung wurden intensive Untersuchungen der chemischen Eigenschaften der Stratosphäre begonnen.

Heute beobachten Satelliten den chemischen Zustand der Atmosphäre kontinuierlich. Eine Analyse dieser großen Datenmengen erlaubt eine globale und detailliertere Beschreibung der Atmosphäre. Die existierenden Datenquellen unterscheiden sich deutlich hinsichtlich der Datendichte, Messfrequenz und ihrer Repräsentativität. Beispielsweise besteht das Network for the Detection of Stratospheric Change (NDSC) aus einer Reihe von unregelmäßig verteilten Fernerkundungsstationen. Auch Satellitenmessungen sind durch unregelmäßige Beobachtungsorte und -zeiten gekennzeichnet. Dabei hängt die Häufigkeit der Beobachtung an einem Ort vom Satellitenorbit ab. Andererseits weisen Satelliten den Vorteil auf, auch für unzugängliche Orte Messwerte zu liefern. Außerdem sind manche Satelliten für Langzeitmessungen konzipiert.

Aufgrund der Heterogenität der Beobachtungen werden für eine gemein-

same Interpretation der Messungen hochentwickelte Methoden benötigt. Der Gebrauch eines Chemie-Transport-Modells (CTMs) erlaubt es, Messungen mit a priori Wissen von chemischen und physikalischen Atmosphärenprozessen zu kombinieren. CTMs untersuchen den Einfluss von Transport und chemischen Reaktionen auf die Zusammensetzung der Atmosphäre. Meteorologische Analysen werden dabei beispielsweise von allgemeinen Zirkulationsmodellen übernommen. In dieser Arbeit werden die Analysen des United Kingdom Meteorological Office (UKMO) in einem CTM verwendet, das aus dem Kölner Modell der Mittleren Atmosphäre (COMMA) im Rahmen dieser Arbeit entwickelt wurde. Dieses Modell wird in Kapitel 5 vorgestellt. Die bevorzugte Methode, um experimentelle Daten und numerische Modelle zu kombinieren, ist die vierdimensionale variationale (4D var) Datenassimilation, die in Kapitel 2.1 im Detail beschrieben wird. Sie erlaubt die Berücksichtigung von Messungen unter Beachtung ihrer Bedeutung bei der Modellierung, ohne das chemische Gleichgewicht des Modells zu stören. Durch dieses Verfahren kann die unregelmässige Verteilung der Messungen kompensiert werden. Die dabei erstellten synoptischen Karten enthalten dadurch Zusatzinformationen im Vergleich zu den Rohdaten. Die Modifikationen des im Folgenden auch Vorwärtsmodell genannten COMMA-CTM, die nötig waren, um ein effizientes und stabiles 4D var Datenassimilationssystem zu entwickeln, werden in Kapitel 5.1 erläutert.

Die 4D var Methode basiert darauf, dass (abgesehen von Randwertfragen) die Chemie-Transport-Modellierung als Anfangswertproblem angesehen werden kann, so dass die Wahl der Anfangswerte auch zu späteren Zeitpunkten den Grad der Übereinstimmung des Modells mit den Messungen festlegt. Die Übereinstimmung zwischen dem Modellzustand auf der einen Seite und Messungen sowie weiteren Informationen wie Klimatologien oder vorausgehenden Modellläufen auf der anderen Seite, die üblicherweise als Hintergrundwissen bezeichnet werden, wird durch eine skalarwertige Kostenfunktion gemessen. Die Definition der Kostenfunktion muss gut überlegt sein, da sie den relativen Einfluss der Informationsquellen durch die Verwendung von Fehlerkovarianzmatrizen gewichtet. Aufgrund der Kostenfunktion, die den Einfluss von Modell und Beobachtungen gegeneinander abwägt, kann die resultierende Analyse als objektiv bezeichnet werden. Neben Beobachtungen und vorherigen Modellläufen wird in dieser Arbeit die Verwendung der Krümmung der Spurengasfelder als Information untersucht. Motiviert war diese Modifikation der Kostenfunktion durch den Vergleich erster Analysen mit den zugrundeliegenden Messungen, interpoliert auf ein $2^\circ \times 2^\circ$ Gitter. Die Analysen zeigten deutlich stärkere Variationen zwischen benachbarten Gitterpunkte als die Messungen. Ein Krümmungsterm in der Kostenfunktion bestraft die Krümmung der Spurengasfelder zu Beginn des Assimilationsintervalls. Als Maß für die Krümmung wird der horizontale Laplaceoperator auf die Spurengasfelder angewandt. Dieser Term vergleicht benachbarte Gitterpunkte und bewirkt die Ausbreitung von Informatio-

nen von beobachteten zu unbeobachteten benachbarten Gitterpunkten. Die Änderung der Kostenfunktion und des Gradienten werden in Kapitel 7 beschrieben, gefolgt von einem Vergleich mit einer alternativen Methode zur Informationsausbreitung, der Verwendung von Nebendiagonalelementen in der Hintergrundfehlerkovarianzmatrix. Es wird dargelegt, dass die Annahmen über Feld- und Fehlerkorrelationen der verwendeten Hintergrundfelder die Grundlage darstellen, um zu entscheiden, welche der beiden Methoden am besten verwendet werden sollte.

Die Idee der 4D var Datenassimilation ist die Minimierung der Kostenfunktion auf iterative Weise. Um auch kleinskalige Strukturen in die Analyse einfließen zu lassen, wurde der Einfluss des Krümmungsterms bei späteren Iterationen reduziert. Das Modellgebiet umfasst (96*71+2)*10 Gitterpunkte, und an jedem Gitterpunkt werden die Anfangswerte von 41 Spezies benötigt. Aus diesem Grund wird der L-BFGS Minimierungsalgorithmus, der nur moderat viel Speicherplatz benötigt, verwendet, um neue Anfangswerte zu bestimmen. Dieser Algorithmus sowie die vorgenommenen Änderungen werden in Kapitel 8.1 skizziert. Um eine schnellere Minimierung zu erreichen, werden die Spurengasfelder und der Gradient vor dem Aufruf der Minimierungsroutine präkonditioniert.

Für die Minimierung wird der bereits erwähnte Gradient der Kostenfunktion benötigt. Dieser kann durch die Verwendung des adjungierten Modells zum tangential-linearen Modell effizient bestimmt werden. Kapitel 6 befaßt sich ausführlich mit der Entwicklung des adjungierten Modells. Hierzu können adjungierte Compiler verwendet werden, allerdings muss der produzierte Programmcode vor der Verwendung eingehend geprüft werden. Das CTM, das adjungierte Modell und der Minimierungsalgorithmus stellen zusammen das 4D var Datenassimilationssystem dar, das AMMOC-CTM benannt wurde und in Kapitel 9 beschrieben wird. Dabei wird auch die verwendete Speicherstrategie diskutiert, denn das adjungierte Modell benötigt große Datenmengen der Trajektorie des Vorwärtsmodells.

Das AMMOC-CTM ermöglicht die Bestimmung des CTM-Anfangszustandes, der im Sinne der Methode der kleinsten Fehlerquadrate in bester Übereinstimmung mit allen verfügbaren Information resultiert. Daher liefert es den besten linearen Schätzwert ohne Bias, der, aus dem Englischen stammend, auch als BLUE bezeichnet wird. Der Preis für diese gute Leistung sind hohe Rechenzeit- und Speicheranforderungen. Das AMMOC-CTM wurde in Identical Twin Experimenten getestet, die in Kapitel 10 dargestellt werden. In diesen Experimenten werden, anstelle von Realdaten, vom Vorwärtsmodell in einer separaten Integration generierte Daten verwandt, die als “Wahrheit” angesehen werden. Ausgewählte Daten werden dem Assimilationssystem als Beobachtungen zur Verfügung gestellt. Neben der Überprüfung der Korrektheit des Modellsystems erlauben diese Tests zu untersuchen, wie die Wahl der gemessenen Spezies, die dem Assimilationssystem zur Verfügung gestellt werden, die Qualität der Analyse beein-

flusst. In Vorbereitung auf das Realdatenexperiment bezogen sich die Untersuchungen auf die Novemberatmosphäre und die durch CRISTA gemessenen Spezies. Die Ergebnisse zeigen, dass die zur Verfügung stehenden Messungen von O_3, N_2O, HNO_3, $ClONO_2$ und CH_4 zu einer verbesserten Beschreibung der gemessenen und vieler nicht beobachteter Spezies führen. Der Grad an Übereinstimmung hängt dabei deutlich vom chemischen Regime am betrachteten Gitterpunkt ab.

Die Assimilation von CRISTA Daten ist Gegenstand von Kapitel 11. Die Eigenschaften des Assimilationssystems unter Verwendung des Krümmungsterms werden durch synoptische Karten und statistische Berechnungen untersucht. Am Beispiel von $ClONO_2$, das einen ausgeprägten Tagesgang aufweist, konnte die Überlegenheit der 4D var Datenassimilation gegenüber Interpolation der Messungen gezeigt werden. Die Analyse von N_2O zeigte, wie im Laufe des Assimilationsexperiments auch das nicht durch Messungen überdeckte Gebiet südlich von 60°S mit Informationen versorgt wurde. Das Ergebnis der Analyse hängt dabei deutlich von den verwendeten Annahmen über die Fehler ab. Eine von Talagrand (1998) vorgeschlagene Untersuchungsmethode wurde erweitert, um die Übereinstimmung der Analyse mit den verwendeten Fehlerkovarianzmatrizen zu überprüfen. Sie wird in Kapitel 12 dargestellt und auf die durchgeführten Realdatenexperimente angewandt. Dabei konnte festgestellt werden, dass der Hintergrundfehler von der Größenordnung von 50% ist. Im letzten Kapitel erfolgt eine Zusammenfassung der Arbeit und eine Diskussion der erhaltenen Ergebnisse.

Acknowledgements

First of all I would like to thank Prof. Dr. Adolf Ebel to offer me the opportunity to learn and work at and with the EURAD group. I especially appreciated his support and his interest in data assimilation.

I want to express my gratitude to PD Dr. Hendrik Elbern whose interest in data assimilation was contagious. He has shown me the way into a fascinating area of geophysical research. Thanks for so many interesting and helpful discussions and for pointing out possible research directions. He was always available for questions and showed me how to track down numerical issues in complex models. I appreciated his comments on the draft version of this thesis.

My thank is due to Prof. Dr. Michael Kerschgens who has kindly accepted to act as a referee for this thesis.

I owe special thanks to Jörg Schwinger and Dr. Anna Klyuchnikova for supplying the chemistry box model and its adjoint and for many enriching discussions. Thanks to everyone at EURAD for the positive and friendly working environment. Especially the system administrator, Georg Piekorz, was always and immediately helpful with any type of problem, even during the weekend.

I am indebted to Dr. Frank Baier for introducing me to COMMA and for many interesting discussions. Dr. Johannes Hendricks kindly provided the chemistry mechanism.

This work would not have been possible without the CRISTA measurements. Therefore, I want to thank PD Dr. Martin Riese, Bernd Schäler, Lars Hoffmann and the CRISTA team for providing the CRISTA data with detailed error statistics and helpful advice on their interpretation. The British Atmospheric Data Centre has provided UKMO data. Thanks to J. Nocedal for providing L-BFGS algorithm. KPP has been developed by V. Damian, A. Sandu, M. Damian, F.A. Potra, and G.R. Carmichael. O∂yssee was provided by INRIA, Nice, France.

This work was funded by the Graduiertenkolleg Scientific Computing and the AFO2000 project SACADA. Calculations were carried out in the Regional Computing Centre of the University of Cologne (RRZK) and RWTH

Aachen, many thanks to Dieter an May and Rud van der Pas for their introduction to high performance computing and parallelization and their interest in my work.

Several people were involved in the proofreading of this thesis. Thank you very much, all of you!

My special thanks to my family, Bernd Rosenow and all my friends for (among many other things) minimising my social cost function measuring the deviation of my state from the state of perfect well-being. Your presence was always a rapid minimiser!